PERFORMANCE PHYSICS

ANALYSIS AND SYNTHESIS OF COMMUNICATIVE BODIES

by

ANTHONY SCHULTZ

A dissertation submitted to the Graduate Faculty in Physics in partial fulfillment of the requirements for the degree of Doctor of Philosophy, The City University of New York

2012

This manuscript has been read and accepted for the Graduate Faculty in Physics in satisfaction of the dissertation requirement for the degree of Doctor of Philosophy.

BRIAN SCHWARTZ

Date | Chair of Examining Committee

IGOR KUSKOVSKY

Date | Executive Officer

STEPHEN BRIER

SULTAN CATTO

ADRIAN DUMITRU

JOSEPH KRIEGER

JIE WEI

Supervisory Committee

THE CITY UNIVERSITY OF NEW YORK

Abstract

PERFORMANCE PHYSICS
ANALYSIS AND SYNTHESIS OF COMMUNICATIVE BODIES

by

Anthony Schultz

Adviser: Brian Schwartz

Human motion contains information like written or spoken language. Contemporary camera and computer technologies capture this information for gaming, animation, medical diagnostics and robotic control. In this thesis we model human performance recorded with motion capture and video. Beginning with a kinematic chain model of the human body we generate a metric for comparing different states of skeletal articulation. Applying this measure over motion data time series generates similarity spectra from which we identify and characterize body motions. We use the results to model the subject's underlying movement vocabulary with a network of connected recordings called a motion graph. We construct a set of motion graphs from video data and by assigning variable transition probabilities between recorded movement sequences we model the purposeful subject as a stochastic traversal process on the motion graph. Finally we present the application of a non-anatomical kinematic chain model to video data and derive the accompanying distance metrics. We discuss the results and possible applications of these techniques.

Acknowledgments

I'd like to begin by expressing my appreciation to my dissertation adviser, Brian Schwartz. His help and guidance over the course of this research has made its completion possible.

I would also like to thank Sara Rudner for her help and insight. She has been generous with her time and intellect. I continue to learn a great deal from her. The freedom she gave me in developing my course at Sarah Lawrence College enabled me to hash out and prototype many of the ideas presented in this thesis.

Thanks also to my students, the spirited Caity Gwin and the unflappable Jeremy Pheiffer, for their participation in this research.

Additionally, I would like to thank my mother Priscilla Murolo and my father Stephen Schultz for their support and encouragement, of both my work and play. Many thanks as well to my stepfather Ben Chitty for many helpful edits.

Finally, thanks to Katherine and Beatrice for their love and care during the preparation of this manuscript. I could not have done it without them.

Contents

List of Figures

List of Tables

> The word communication will be used here in a very broad sense to include all of the procedures by which one mind may affect another. This, of course, not only involves written and oral speech, but also music, the pictorial arts, the theatre, the ballet, and in fact all human behavior.
> *Claude Shannon: The Mathematical Theory of Communication* [49]

1 Introduction

1.1 Communication, Performance and the Body

Claude Shannon's 1948 paper, "A Mathematical Theory of Communication," [50] develops much of modern communication theory, defining the process of communication as the transmission of a message from source to receiver. It models the source as a stochastic process characterized by a discrete Markov network. Shannon develops this as an effective model for representing written language or (digitally transduced) spoken language.

The quotation above, from the introduction to the 1949 book [49] reprinting the original paper, shows Shannon expanding the scope of the term communication to include not only natural language, but also the arts. The incorporation of performing arts indicates an understanding of the communicative power of the body and a certain insight, that a linguistic structure underlies a performance technique such as ballet.

Shannon uses dance rhetorically as the penultimate stop in developing a general theory of "all human behavior" based on the thought that if we are able to read, interpret and model the language of the dancing body then we should be also be able to read, interpret and model the activity of human bodies in general.

1.2 Technology

Contemporary media now include camera and vision technologies capable of digitally transducing and displaying human body motion. This enables scientists to expand their research into measuring and modeling human activity. They also open up more applications in the culture for digitally modeling and apprehending the body. There are several technologies which have dramatically changed the way bodies in space are measured and represented.

Vision based motion capture technology has become an industrial standard. There has grown a broad range of applications from animation for video games and movies to medical diagnostics, sports analysis and even as a compositional tool in the performing arts. These systems, such those developed by VICON, use reflective markers, infra-red light sources and multiple high speed cameras to render a full 3D representation of the human body in motion. Unfortunately the high cost of such systems makes their use prohibitive to the general public or less well funded institutions.

Computers equipped with high resolution digital video cameras are ubiquitous in gaming systems, security, cellphones, traffic cameras and laptops. Computer vision algorithms are continually being developed to track and model humans activity in video streams. Methods such as face recognition, color segmentation and Cartesian moment analysis are all available as part of the open source OpenCV library.[30]

Microsoft Kinect is a camera based controller for the XBox gaming system. The device consists of a VGA video camera and an infrared laser depth sensor, both 1280-1024 pixel 10-bit CMOS sensors. Both cameras are mounted alongside a microphone array on a small motorized pivot. The system software provides 3D motion capture with facial, voice and gesture recognition. OpenKinect is an open source library which allows access to Kinect's functionality. [1]

Human motion may also be transduced using accelerometers. Many consumer electronic

devices (cell phones, cameras, laptops) now contain them. An integrated chip reports the force of gravity relative to its frame and pseudoforces associated with the frame's acceleration. The Wii gaming controller uses an ADXL330 3-axis accelerometer to gain information about the controller's orientation and movement. It measures about +/-35 N at roughly 0.3 N resolution, reporting numbers between 0-255 for each axis.[6] This data is reported wirelessly using standard Bluetooth protocol. Magnetometers or gyroscopic sensors are often integrated with accelerometers to provide complete orientation data in 3D.

In considering a science of performance we should think of each of these technologies as another transducer for bodies through which bodies may send messages through their physical actions. The pace of these advances are impressive. At the time of starting this research consumer technologies were not capable of providing realtime 3D motion capture. Now the Kinect provides it in a turnkey fashion at low cost.

1.3 Previous Work and Applications

Since the commercial availability of motion capture systems researchers have been working on the problem of building movement libraries by splicing together threads of motion capture into a network known as a motion graph. This process was developed by Arikan and Forsyth [7] and Kovar et al. [33] and detailed by Alankus [3] in a comprehensive thesis. The challenge in building a motion graph is knowing where to splice the motion capture threads together. This is done by generating a distance metric to measure the proximity between body states. The task of navigating the motion graph in a way that fits the desires of the animator or optimizes some constraint is known as motion planning.

The metric space created by measuring the difference between elements of a motion capture time series has information in itself regarding the body's displacement over time. An exhaustive literature search does not find any scholarship detailing the correspondence between visual motifs in the metric space images, physical motifs in the movement sequences

and topological motifs in the corresponding motion graph.

Our method, using a metric and a pseudo metric to measure spatial symmetries across the sagittal plane of the body generates a novel visual representation of important movement features. This technique could find applications in biomechanics and medical diagnostics helping to identify pathological movement and help treat it. In work such as gait analysis [57] our similarity plot could be of use to medical practitioners for visualizing the period, phase, symmetry, and stability of a gait cycle.

Outside of using commercial motion capture data, vision and movement researchers such as Bregler [15] and Pullen [44] have applied physical models for tracking subjects in image sequences by using the mathematics of twists and exponential maps for representing kinematic chains. This mathematics of kinematic chains is outlined in Chapter 2.

Statistical color segmentation and moment analysis are powerful tools used by computer vision researchers and developers. Models such as presented by Liu and Lovell [35], Bradski [12] and Allen et al. [5] use a dynamic technique to track human motion, based on both color and moment distribution, called camshift. It is an optimized version of meanshift byBailer et al. [8]. Though we do not use camshift tracking to extract image features, our method in Chapter 5 is nearly equivalent as is yields the same image features.

Recognition techniques using moment analysis have been presented by Hu [27], Nagao and Horn [40], Flusser [21], Mukundan et al. [38], Pirard [43] and Flusser et al. [22] for 2D image distributions, Novotni and Klein [41] for 3D distribution and Sinha et al. [52] for 2D image time series. These types of moment analysis techniques underlie many patented gesture recognition applications such as those by Smith et al. [53], [18], Russell and Zipperer [46] andHatlelid et al. [26]. Our work in Chapter 5 falls along these same lines to generate a recognition scheme for comparing states of the body. Our method could be easily integrated with methods in the above research to generate a more efficient and robust strategy for tracking and recognizing human activity.

1.4 Present Work

The goal of the present research is to elaborate a physics of performance, namely to recognize and represent what the human body is capable of communicating using example data and physics based modeling.

In Chapter 2 we develop a method for mathematically representing articulation of the human skeleton. We use a kinematic chain model with state variables measured by motion capture technology. A pair of metrics is developed for measuring the difference between kinematic states.

Chapter 3 uses the space of this metric pair, over a kinematic time series, to extract the corresponding motion graphs. A taxonomy of movement based on space and time symmetry motifs is presented. Example motion capture data is analyzed and the motion graphs are extracted.

Chapter 4 applies an approach similar to Chapter 3 in extracting motion graphs for processed video sequences. With the processed body-image as our reduced representation we generate a metric set for comparing body-image states. We then use the corresponding metric space to construct the motion graph for a body-image time series. The motion graph is used to generate the Markov network for simulating the activity of the original subject.

Chapter 5 develops a kinematic chain model for image features of upper body gestures and the associated similarity metric. Computer vision methods including skin and face recognition are discussed and used to extract image features. Third order Cartesian moment analysis is applied to generate a functioning similarity metric.

1.5 Prototyping Tools

Much of the early work in this project was prototyped using Matlab. When 3-D animation capacity and realtime applications became a priority we began using Max/MSP/Jitter (MMJ). MMJ is a programming tool that provides a graphical dataflow programming environment for video and numerical processing. It supports char, float32, float64, string processes and includes many C functions such as expr, sprintf, and regular expressions. Data can be input and output in the form of images, various video compressions and as text files. The graphical programming interface allows the developer to generate an algorithmic pipeline and GUI using block diagrams. In this way it is very similar to Labview or Matlab's Simulink blockset interface, though it is much less expensive.

MMJ is supported by a large community media science researchers. Jean-Marc Pelletier of the Institute of Advanced Media Arts and Sciences has provided a free toolbox for MMJ called cv.jit which ports much of the functionality of Intel's OpenCV library.[42] This includes face recognition and moment analysis. Pelletier has also ported the OpenKinect open source library into MMJ with a coding object called jit.freenect.grab. Masayuki Akamatsu, also at the Institute of Advanced Media Arts and Sciences, has ported open source code to enable data acquisition from the Wii remote in Max/MSP.[2]

2 Kinematic Chains

In this chapter we develop the necessary physics and mathematics to represent the human body in regard to the placement of its parts in space and their displacement over time. We model each part of the body as a rigid element consisting of massive particles, distributed in space, so that inter-particle distances are invariant.

Each rigid element may undergo linear displacement (translation), angular displacement (rotation), or any combination of the two. The combination of translation and rotation is known as a rigid body transformation. More technically, a rigid body transformation is a mapping g: $\mathbb{R}^3$ to $\mathbb{R}^3$, in which the vector length and cross product are preserved.

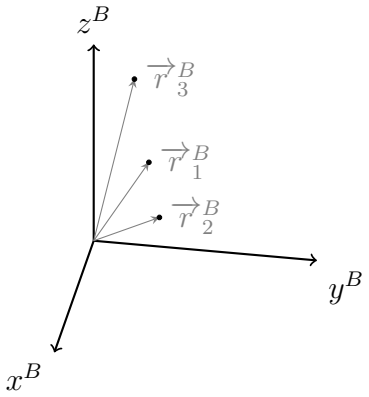

Figure 1: Rigid Body Represented in the Body Frame B

We set each rigid element in a Cartesian coordinate system so that each particle of that element is fixed within the coordinate system. We call this coordinate system the body coordinate system or the body frame B. The positions of each particle constituting the rigid body, as measured in the frame B, are notated as $\overrightarrow{r}_i^B$, where i is used as an index over all particles in the body. The rigid element within the body coordinate system B is shown in Figure 1.

Tracking the rigid element in a stationary global coordinate system, or global frame A, would mean knowing the positions of each particle constituting the rigid body, as measured in the

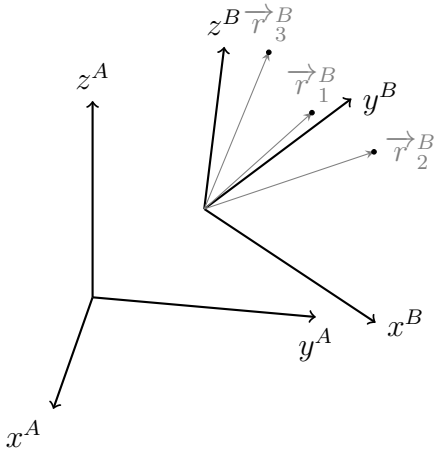

Figure 2: Body Frame B Embedded in Global Frame A

global frame A, namely $\overrightarrow{r}_i^A$. This only requires we know the position and orientation of the body frame B within the global frame A. The rigid body within the global coordinate system A is shown in Figure 2.

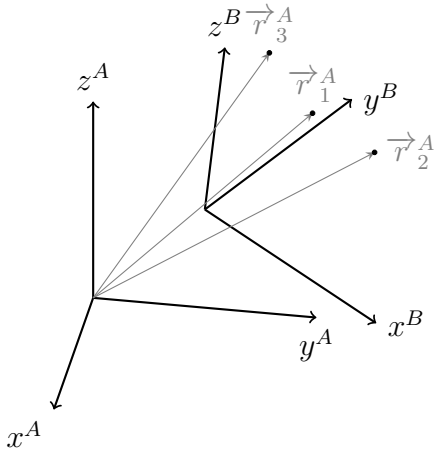

Figure 3: Rigid Body Represented in the Body Frame A

We couch this within the language of rigid body transformations as follows. The rigid body transformation g_{AB} maps the body coordinate frame B to the global coordinate frame A. In so doing g_{AB} maps the rigid body particle's positions as measured in the body frame B, $\overrightarrow{r}_i^B$, to the rigid body particle's positions as measured in the spatial frame A, $\overrightarrow{r}_i^A$. In this way we can describe the position and orientation of the rigid body through the rigid body transformation g_{AB}, as shown in Figure 3.

$$\overrightarrow{r}_i^A = g_{AB}\overrightarrow{r}_i^B$$

The set of all such transformations composed of rotation and translation is called SE(3), the special Euclidean group of rigid body displacements in three-dimensions.

2.1 Matrix Rotations

The set of all transformations composed of rotation in three dimensions is called SO(3), the special orthogonal group. SO(3) is a Lie group and can be recovered through the exponential mapping of the Lie algebra so(3). [25]

We use multiple representations for three dimensional rotation in this work. Given a vector $\overrightarrow{r}$ rotations map $\overrightarrow{r}$ under matrix multiplication $R\overrightarrow{r}$. The inverse of the rotation matrix is given by its transpose.

$$R^{-1} = R^T$$

The matrices for rotation around the x, y and z axis are given.

$$R_x = \begin{pmatrix} 1 & 0 & 0 \\ 0 & \cos\theta_x & -\sin\theta_x \\ 0 & \sin\theta_x & \cos\theta_x \end{pmatrix} \quad R_y = \begin{pmatrix} \cos\theta_y & 0 & \sin\theta_y \\ 0 & 1 & 0 \\ -\sin\theta_y & 0 & \cos\theta_y \end{pmatrix} \quad R_z = \begin{pmatrix} \cos\theta_z & -\sin\theta_z & 0 \\ \sin\theta_z & \cos\theta_z & 0 \\ 0 & 0 & 1 \end{pmatrix}$$

Composite transformations are generated by successive rotation around the cardinal axes. Values of these ordered angular displacements are known as Euler angles. Angles applied around the x, y then z axis are known as Fick angles.

$$R_{zyx}(\theta_x, \theta_y, \theta_z) = R_z(\theta_z)R_y(\theta_y)R_x(\theta_x)$$

Fick angles are used to report joint angles in motion capture data. Euler angle parameterization is prone to singularities producing "gimbal lock."

Euler's rotation theorem states that in 3D space any two coordinate systems with a common origin are related by a rotation about a fixed axis. Rather than give three angles, the rotation is parameterized by a single angle and an axis of rotation known as the Euler pole. [39]

We will derive the Lie algebra generators of rotations as done by Hammermesh [25] to develop a reparameterized form of the rotation matrix. The Lie algebra is obtained by extracting tangents near the identity.

$$
\begin{aligned}
dR_x = R_x(d\theta_x) - \mathbb{I} &= \begin{pmatrix} 0 & 0 & 0 \\ 0 & 0 & -d\theta_x \\ 0 & d\theta_x & 0 \end{pmatrix} = \begin{pmatrix} 0 & 0 & 0 \\ 0 & 0 & -\omega_x \\ 0 & \omega_x & 0 \end{pmatrix} d\theta \\
dR_y = R_y(d\theta_y) - \mathbb{I} &= \begin{pmatrix} 0 & 0 & d\theta_y \\ 0 & 0 & 0 \\ -d\theta_y & 0 & 0 \end{pmatrix} = \begin{pmatrix} 0 & 0 & \omega_y \\ 0 & 0 & 0 \\ -\omega_y & 0 & 0 \end{pmatrix} d\theta \\
dR_z = R_z(d\theta_z) - \mathbb{I} &= \begin{pmatrix} 0 & -d\theta_z & 0 \\ d\theta_z & 0 & 0 \\ 0 & 0 & 0 \end{pmatrix} = \begin{pmatrix} 0 & -\omega_z & 0 \\ \omega_z & 0 & 0 \\ 0 & 0 & 0 \end{pmatrix} d\theta
\end{aligned}
$$

We introduce the vector $\overrightarrow{\omega} = \begin{pmatrix} \omega_x \\ \omega_y \\ \omega_z \end{pmatrix}$ as the axis of rotation or Euler pole. The vector is normal, $|\overrightarrow{\omega}| = 1$. The associated matrix $\hat{\omega}$ is traceless and skew symmetric. The matrix $\hat{\omega}$ forms the action of the vector cross product through matrix multiplication.

$$
\hat{\omega} = \begin{pmatrix} 0 & -\omega_z & \omega_y \\ \omega_z & 0 & -\omega_x \\ -\omega_y & \omega_x & 0 \end{pmatrix} = \overrightarrow{\omega} \times
$$

With this we can express the action of the transformation away from identity for infinitesimal angular displacement around the axis $\overrightarrow{\omega}$ as follows.

$$
dR = dR_x + dR_y + dR_z = \hat{\omega} d\theta
$$

We identify the matrix $\hat{\omega}$ as the generator of rotations around the axis $\overrightarrow{\omega}$. We may use the exponential mapping to recover the matrix form of the transformation. In the exponentiation we make use of the identity $\hat{\omega}^3 = -\hat{\omega}$.

$$
R_\omega = e^{\hat{\omega}\theta} = \mathbb{I} + \hat{\omega} \sin\theta + \hat{\omega}^2 (1 - \cos\theta)
$$

With this formula we are able to construct the matrix associated with an rotation of θ about an axis $\overrightarrow{\omega}$. For any rotation matrix, $R = \begin{pmatrix} r_{11} & r_{12} & r_{13} \\ r_{21} & r_{22} & r_{23} \\ r_{31} & r_{32} & r_{33} \end{pmatrix}$, we can determine the parameters θ and $\overrightarrow{\omega}$ from the following formulae. [39]

$$\theta = \cos^{-1}\left(\frac{trace(R)-1}{2}\right) \qquad \overrightarrow{\omega} = \frac{1}{2\sin\theta}\begin{pmatrix} r_{32}-r_{23} \\ r_{13}-r_{31} \\ r_{21}-r_{12} \end{pmatrix}$$

2.2 Quaternionic Rotations

Using the terms θ and $\overrightarrow{\omega}$ derived above we can switch to a more compact representation using quaternions. Quaternions are a 4-tuple consisting of a real component q_0 and three imaginary components $q_1 i + q_2 j + q_3 k$. The algebra of the imaginary components follows.

$$ii = jj = kk = ijk = -1$$

The imaginary components may be written as a vector $\overrightarrow{q}$ so that the overall quaternion Q can be written $Q = \begin{pmatrix} q_0 \\ \overrightarrow{q} \end{pmatrix}$ Quaternion multiplication between a quaternion $Q = \begin{pmatrix} q_0 \\ \overrightarrow{q} \end{pmatrix}$ and $G = \begin{pmatrix} g_0 \\ \overrightarrow{g} \end{pmatrix}$ is given as follows.

$$QG = Q \cdot G = \begin{pmatrix} q_0 \\ \overrightarrow{q} \end{pmatrix} \cdot \begin{pmatrix} g_0 \\ \overrightarrow{g} \end{pmatrix} = \begin{pmatrix} q_0 g_0 - \overrightarrow{q} \cdot \overrightarrow{g} \\ q_0 \overrightarrow{g} + g_0 \overrightarrow{q} + \overrightarrow{q} \times \overrightarrow{g} \end{pmatrix}$$

Quaternions maybe be used to represent rotations using the Euler axis formalism.

$$q_0 = \cos(\theta/2)$$

$$\overrightarrow{q} = \sin(\theta/2)\overrightarrow{\omega}$$

Clearly the quaternion representing the inverse rotation, Q^{-1}, would be obtained by flipping the sign of θ. $Q^{-1} = \begin{pmatrix} q_0 \\ -\overrightarrow{q} \end{pmatrix}$.

$$QQ^{-1} = Q \cdot Q^{-1} = \begin{pmatrix} q_0 \\ \overrightarrow{q} \end{pmatrix} \cdot \begin{pmatrix} q_0 \\ -\overrightarrow{q} \end{pmatrix} = \begin{pmatrix} q_0^2 + \overrightarrow{q} \cdot \overrightarrow{q} \\ \overrightarrow{0}_3 \end{pmatrix} = \begin{pmatrix} 1 \\ \overrightarrow{0}_3 \end{pmatrix}$$

Rotation of a vector is achieved though quaternion action on a vector $\overrightarrow{r}$ as follows.

$$Q\overrightarrow{r} = Q \cdot \begin{pmatrix} 0 \\ \overrightarrow{r} \end{pmatrix} \cdot Q^* = \overrightarrow{r} + 2q_0 \overrightarrow{q} \times \overrightarrow{r} + 2\overrightarrow{q} \times \overrightarrow{q} \times \overrightarrow{r}$$

The quaternion operation on another quaternion and on a vector is associative.

$$Q_2(Q_1\overrightarrow{r}) = (Q_2Q_1)\overrightarrow{r}$$

Composite quaternion transformations follow this multiplication rule.

$$Q_{AC} = Q_{AB}Q_{BC}$$

In this way the action of the quaternion on the vector is the same as the rotation vector.

$$Q\overrightarrow{r} = R\overrightarrow{r}$$

2.3 Translations and Homogenous Coordinates

Translations are the other type of motion which constitute rigid body transformations. For the combination of both translational and rotational motion we describe the position and orientation of a coordinate frame B relative to a global frame A. We represent the translation by the vector $\overrightarrow{p}_{AB}$ (element of $\mathbb{R}^3$) of the origin of frame B relative to frame A, and Q_{AB} (element of $SO(3)$). In this way the configuration of the system consists of the pair ($\overrightarrow{p}_{AB}$, R_{AB}) and the configuration space of the system is the product space of $\mathbb{R}^3$ with $SO(3)$ which

is the special Euclidian group $SE(3)$. [25]

$$SE(3) = \mathbb{R}^3 \times SO(3)$$

Given point $\overrightarrow{r}_B$ in the coordinate frame B we can recover the coordinate of that point in the frame A by a transformation of coordinates. We name this rigid body transformation g_{AB}.

$$\overrightarrow{r}_A = g_{AB}\overrightarrow{r}_B = Q_{AB}\overrightarrow{r}_B + \overrightarrow{p}_{AB}$$

The action of the rigid transformation may be expressed in matrix form using homogenous coordinates for $\overrightarrow{r}$.

$$\begin{pmatrix} \overrightarrow{r}_A \\ 1 \end{pmatrix} = \begin{pmatrix} Q_{AB} & \overrightarrow{p}_{AB} \\ 0 & 1 \end{pmatrix} \begin{pmatrix} \overrightarrow{r}_B \\ 1 \end{pmatrix}$$

The homogenous matrix representation yields the following for the rigid body transformation g_{AB} and its inverse g_{AB}^{-1}.

$$g_{AB} = \begin{pmatrix} Q_{AB} & \overrightarrow{p}_{AB} \\ 0 & 1 \end{pmatrix}$$

$$g_{AB}^{-1} = \begin{pmatrix} Q_{AB}^* & -Q_{AB}^*\overrightarrow{p}_{AB} \\ 0 & 1 \end{pmatrix}$$

The composition of the transformation from frame C to B and the transformation from frame B to A yields the transformation from frame C to frame A. The composite transformation follows from matrix multiplication.

$$g_{AC} = g_{AB}g_{BC} = \begin{pmatrix} Q_{AB} & \overrightarrow{p}_{AB} \\ 0 & 1 \end{pmatrix} \begin{pmatrix} Q_{BC} & \overrightarrow{p}_{BC} \\ 0 & 1 \end{pmatrix} = \begin{pmatrix} Q_{AB}Q_{BC} & Q_{AB}\overrightarrow{p}_{BC} + \overrightarrow{p}_{AB} \\ 0 & 1 \end{pmatrix}$$

2.4 Instantaneous Transformations

If we take the composition rule for rigid body transformations given above and consider it in time we can investigate instantaneous rigid body transformations. Imagine frame A is associated with the state of the coordinate system at time zero, frame B with the present

state of the coordinate system and frame C with the state of the coordinate system some infinitesimally small time in the future. The composition rule for rigid body transformations, $g_{AC} = g_{AB}g_{BC}$, could then be written as follows.

$$g_{(0,t+\Delta t)} = g_{(0,t)}g_{(t,t+\Delta t)}$$

Multiplying each side of the equation by $g_{(0,t)}^{-1}$ yields an expression for $g_{t,\Delta t}$. This is the infinitesimal transformation applied to the present coordinate frame B which propagates it forward in time. Since this is expressed according to frame B it is notated with a superscript B indicating it is in the body frame.

$$g^B_{(t,t+\Delta t)} = g^{-1}_{(0,t)}g_{(0,t+\Delta t)} = \begin{pmatrix} Q^*_{(0,t)} & -Q^*_{(0,t)}\overrightarrow{p}_{(0,t)} \\ 0 & 1 \end{pmatrix}\begin{pmatrix} Q_{(0,t+\Delta t)} & \overrightarrow{p}_{(0,t+\Delta t)} \\ 0 & 1 \end{pmatrix} = \begin{pmatrix} Q_{(t,t+\Delta t)} & Q^*_{(0,t)}\overrightarrow{p}_{(t,t+\Delta t)} \\ 0 & 1 \end{pmatrix}$$

Much like we identified the Lie algebra so(3), generator of rotations in three dimensions, by evaluating small displacements from identity we can identify the Lie algebra se(3) by evaluating displacements over an infinitesimally small time increment. This takes the form of a twist measured in the body frame $\hat{\xi}^B$. Again the rigid body transformation can be recovered using the exponential mapping $g_{(0,t)} = e^{\hat{\xi}^B\theta}$. [39]

$$g^B_{(t,t+\Delta t)} - \mathbb{I} = \hat{\xi}^B = \begin{pmatrix} \hat{\omega}^B & \overrightarrow{v}^B \\ 0 & 1 \end{pmatrix} = \begin{pmatrix} Q_{(t,t+\Delta t)} - \mathbb{I} & Q^*_{(0,t)}\overrightarrow{p}_{(t,t+\Delta t)} \\ 0 & 1 \end{pmatrix}$$

Measured in the body frame B, the infinitesimal angular and linear displacements are $\hat{\omega}^B$ and $\overrightarrow{v}^B$ respectively. We write them with a dot above to indicate displacements in over infinitesimal time increments.

$$\hat{\omega}^B = Q_{(t,t+\Delta t)} - \mathbb{I} = \dot{Q}$$

$$\overrightarrow{v}^B = Q^*_{(0,t)}\dot{\overrightarrow{p}}$$

In order to recover the rigid body displacement in the spatial coordinate system A we take the adjoint transformation on $g^B_{(t,t+\Delta t)}$. This is performed below in order to recover the twist $\hat{\xi}^A$ parameters $\hat{\omega}^A$ and $\overrightarrow{v}^A$. These are the global frame angular and linear velocities respectively.

$$g^A_{(t,t+\Delta t)} = g_{(0,t)} g^B_{(t,t+\Delta t)} g^{-1}_{(0,t)} = g_{(0,t+\Delta t)} g^{-1}_{(0,t)} = \begin{pmatrix} Q_{(0,t+\Delta t)} & \overrightarrow{p}_{(0,t+\Delta t)} \\ 0 & 1 \end{pmatrix} \begin{pmatrix} Q^*_{(0,t)} & -Q^*_{(0,t)} \overrightarrow{p}_{(0,t)} \\ 0 & 1 \end{pmatrix}$$

$$g^A_{(t,t+\Delta t)} = \begin{pmatrix} Q_{(0,t)} Q_{(t,t+\Delta t)} Q^*_{(0,t)} & -Q_{(0,t)} Q_{(t,t+\Delta t)} Q^*_{(0,t)} \overrightarrow{p}_{(0,t)} + \overrightarrow{p}_{(0,t+\Delta t)} \\ 0 & 1 \end{pmatrix}$$

$$g^A_{(t,t+\Delta t)} - \mathbb{I} = \begin{pmatrix} \hat{\omega}^A & \overrightarrow{v}^A \\ 0 & 1 \end{pmatrix}$$

$$\hat{\omega}^A = Q_{(0,t)} Q_{(t,t+\Delta t)} Q^*_{(0,t)} - \mathbb{I} = Q_{(0,t)} \dot{Q} Q^*_{(0,t)} = Q_{(0,t)} \hat{\omega}^B Q^*_{(0,t)}$$

$$\overrightarrow{v}^A = -Q_{(0,t)} \dot{Q} Q^*_{(0,t)} \overrightarrow{p}_{(0,t)} + \dot{\overrightarrow{p}} = -\hat{\omega}^A \overrightarrow{p} + \dot{\overrightarrow{p}}$$

2.5 Rigid Body Dynamics

When observed from the frame A, an object with mass m has a linear momentum $\overrightarrow{P}^A$ and angular momentum $\overrightarrow{L}^A$.

$$\overrightarrow{P}^A(t) = m \overrightarrow{v}^A(t)$$

$$\overrightarrow{L}^A = I^A(t) \overrightarrow{\omega}^A(t)$$

Since the inertial tensor measured in the global frame $I^A(t)$ changes as the object rotates in time it is easier to describe the angular momentum in the body frame B.

$$\overrightarrow{L}^B(t) = I^B \overrightarrow{\omega}^B(t)$$

The inertial tensor in the spatial frame may be computed by the adjoint transformation on I^B, which is constant in time.

$$I^A(t) = Q_{(0,t)} I^B Q^*_{(0,t)}$$

The kinetic energy may be expressed as follows.

$$KE^A(t) = \frac{m\overrightarrow{v}^A(t) \cdot \overrightarrow{v}^A(t)}{2} + \frac{\overrightarrow{\omega}^B(t) I^B \overrightarrow{\omega}^B(t)}{2}$$

The potential energy $PE(t)$ in a uniform gravitational field is $PE(t) = mgh(t)$, where $h(t) = r_y^A(t)$.

To get the height h we need only to pick off the y coordinate of the position vector in the spatial frame using $\overrightarrow{r}^A(t) = Q_{(0,t)}\overrightarrow{r}^B(t) + \overrightarrow{p}(t)$. With this we have capacity to express the kinetic and potential energy of a rigid body given its mass, inertial tensor, position in the body frame, and transformation $g(t)$.

2.6 Kinematic Chains

We can now apply the mathematics developed above to describe the geometry of a kinematic chain model of the human body. A kinematic chain is a system of articulated rigid elements. Each rigid element is referred to as a link while each point of rotational articulation is called a joint. A kinematic chain in the form of a 2-D robotic arm is shown in Figure 4.

Every link in the kinematic chain is fixed in its own coordinate system and characterized by a mass, center of mass and moment of inertia. The origin of the coordinate system for each link is located at the point of rotational articulation. In this work adjacent links, or kinematic pairs, are connected to one another by fixed joints, meaning the distance between the adjacent link coordinate systems are constant. Therefore the kinematic chains discussed in this work have only rotational degrees of freedom corresponding to the articulation of their constituent joints. Joints with three degrees of freedom are called spherical joints. Joints with one degree are called hinge or revolute joints. [61]

We begin with a global inertial coordinate system we call the global frame A. Relative to this global frame, we identify the position and orientation of the root link in body frame

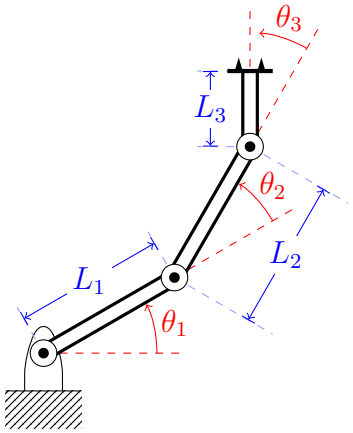

Figure 4: Kinematic Chain of a 2-Dim Robotic Arm

B though the transformation g_{AB}. This is a general rigid body transformation, consisting of a rotation and translation, which maps the body frame B of the root link to the global coordinate frame A. All other links in the kinematic chain are described relative to the root link coordinate frame B. The root link body frame B is the parent to subsequent coordinate frames of other rigid elements. The body frame C is a child to the root link body frame B. The location of the origin of the coordinate system C is fixed within the root link frame B. This is shown in Figure 5.

The variable rotation and fixed displacement of frame C relative to frame B constitutes the rigid transformation g_{BC}. This transformation maps between the coordinate systems of the kinematic pair B and C. The position and orientation of the rigid body C relative to the spatial frame A is known by the transformation g_{AC}. This may be determined through the product of rigid transformations g_{AB} and g_{BC}.

$$g_{AC} = g_{AB} g_{BC}$$

This is a restatement of the composition rule for rigid body transformations.

A kinematic chain is termed open if its terminal link, or end effector, is free to move. The end effector's position and orientation are determined by taking the product of the

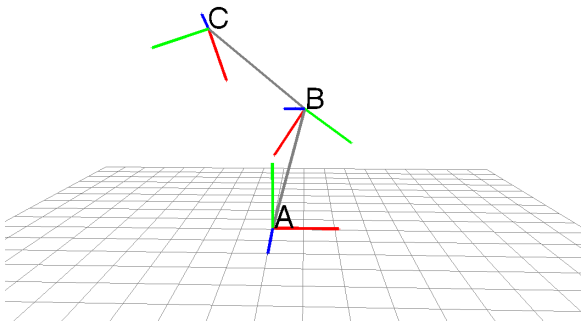

Figure 5: Kinematic Chain Coordinate Systems A, B and C (x-red, y-green, z-blue)

transformations relating relative displacements of parent/child kinematic pairs down the chain. Using numbers instead of letters to notate frame indices we write the following to represent the general open serial kinematic chain.

$$g_{(0,n)} = g_{(0,1)}g_{(1,2)}\cdots g_{(n-1,n)}$$

With the transformation $g_{(0,n)}$ known as a time series for every nth rigid element of the kinematic chain it is possible to calculate the linear and angular velocities as measured in the global coordinate frame, $\hat{\omega}^A$ and $\overrightarrow{v}^A$, for each rigid element of the kinematic chain. Given the mass and moment of inertia of each rigid element we may also know its linear momentum, angular momentum and kinetic energy. The linear momentum, angular momentum and kinetic energy of the whole chain is simply a sum of these terms.

2.7 Modeling the Human Body

The human skeleton consists of a hierarchy of open kinematic chains. A serial kinematic chain is a single kinematic chain without branching. The axial skeleton (pelvis, spine and head) can be modeled by a serial kinematic chain. Branching off this central axis is the appendicular skeleton, namely the left and right arm and the left and right legs. Though there are additional branchings for fingers and toes we will model each as its own serial kinematic chain.

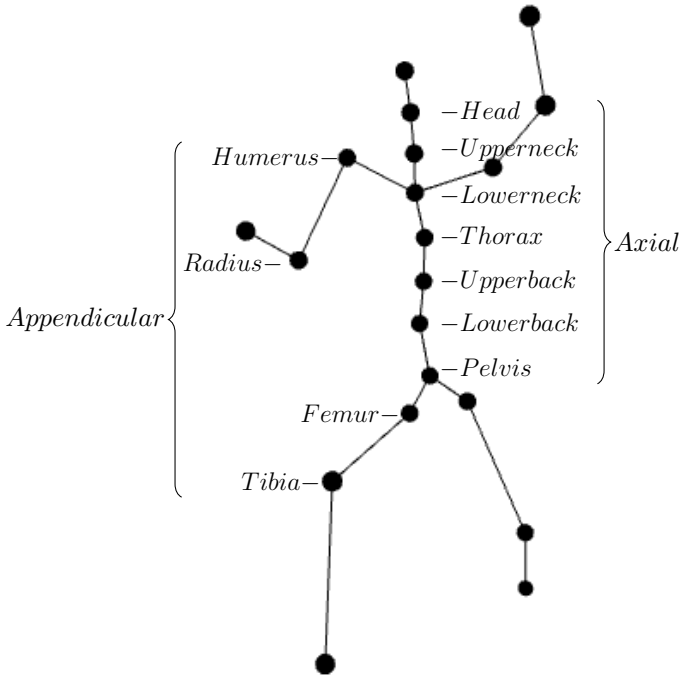

Figure 6: Kinematic Chain Model of Human Body

In this treatment we use a simplified model of the body. We model the axial skeleton with seven links. They are the pelvis (root), lowerback, upperback, thorax, lowerneck, upperneck and head. This is shown in Figure 6. Each joint connecting these links is spherical with three degrees of freedom. Off the pelvis we have the left and right leg. Each is modeled with

two links, the femur and tibia. The femur having a spherical joint (3 DOF) and the tibia having a revolute joint (1 DOF). The left and right arm are measured in the same way as the legs. They branch off the thorax link of the axial skeleton with the humerus having a spherical joint (3 DOF) and the radius having a revolute joint (1 DOF).

2.8 Intrinsic and Extrinsic Parameters

We assume the body to be set on a flat Euclidean space in which gravity is in the downward y direction. We will split the coordinates defining the position of the body's link into two sets, constituting extrinsic and intrinsic parameters. We call the extrinsic parameters those degrees of freedom which do not effect the energy of the the body's elements. The extrinsic parameters are made up of the two coordinates of location in the horizontal plane and orientation around the axis of gravity for the root link. This represents those coordinates for which the body has no "feel" through propioception. They are also parameters which can theoretically take on any value.

The intrinsic parameters can all be grouped into define the body's configuration, state of joint articulation or pose. We discard the vertical position of the root element by assuming it is contingent on the rotational states of the child coordinate frames. The intrinsic parameters are all joint angles and affect the energy of the body. For this reason the intrinsic parameters are those of which the subject's own body would have a sense through propioception.

The set of quaternion values describing the intrinsic parameters of the joint articulations completely represent the body's internal configuration or pose. This consists of 15 quaternions or 60 scalar values. Though there are 60 scalar values for this model they represent an internal mobility, number of degrees of freedom, of 36.

2.9 Configuration Space

We collect the set of quaternions determining the pose of the body model into a state or configuration vector $\overrightarrow{\Psi}$. We begin with a basis in which each element of the vector, quaternion Q_i determines the rotational state of joint i. The quaternions, which represent a set of rotational transformations, constitute a manifold. This manifold is called the configuration space, or $\mathcal{C}$, of the kinematic chain. The state vector $\overrightarrow{\Psi}$ spans $\mathcal{C}$. Due to limits on range of motion of each joint and conditions of self collision not all $\overrightarrow{\Psi}$ are physically posible. The set of all physically realizable $\overrightarrow{\Psi}$ constitute a subspace of $\mathcal{C}$. We this subspace $\mathcal{C}_{free}$. It is the accessible part of the manifold.

Therefore each physical configuration of the kinematic chain model is associated with a state vector $\overrightarrow{\Psi}$. In turn, this configuration vector (state vector) is associated with a point in the configuration space $\mathcal{C}$. The three representations are shown together in Figure 7.

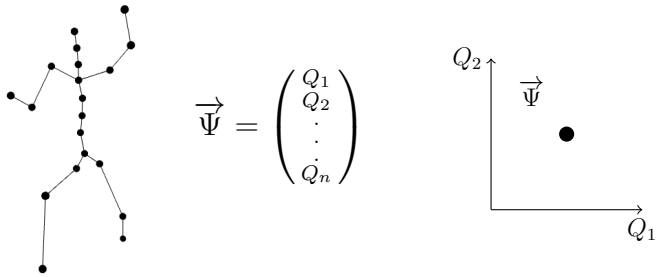

Figure 7: Physical Model, State Vector and Point in $\mathcal{C}$

2.10 Reflection

Due to the symmetry of the human body we know for any configuration state $\overrightarrow{\Psi} \in \mathcal{C}_{free}$ there exists a mirror image configuration state $\overrightarrow{\Psi}^* \in \mathcal{C}_{free}$. The reflection transformation maps the state of the body from $\overrightarrow{\Psi} \rightarrow \overrightarrow{\Psi}^*$.

We will specify the action of this transformation on the configuration state of the body. In

this way we can form a new set of generalized coordinates for the state of the body where the action of this mapping takes on a more simple form.

We begin by splitting $\overrightarrow{\Psi}$ into three separate components. These are the axial component $\overrightarrow{\Theta}$, consisting of the Q values for the axial skeleton, and the appendicular components $\overrightarrow{\Gamma}_{left}$ and $\overrightarrow{\Gamma}_{right}$, consisting of the Q values for the appendicular skeleton.

$$\overrightarrow{\Psi} = \begin{pmatrix} \overrightarrow{\Theta} \\ \overrightarrow{\Gamma}_{left} \\ \overrightarrow{\Gamma}_{right} \end{pmatrix}$$

$$\overrightarrow{\Theta} = \begin{pmatrix} Q_{root} \\ Q_{lowerback} \\ Q_{upperback} \\ Q_{thorax} \\ Q_{lowerneck} \\ Q_{upperneck} \\ Q_{head} \end{pmatrix}$$

$$\overrightarrow{\Gamma} = \begin{pmatrix} Q_{femur} \\ Q_{tibia} \\ Q_{humerus} \\ Q_{radius} \end{pmatrix}$$

We define a reflection operator **w** which reflects across the y-z plane, reversing the x-axis. This maps a right handed coordinate system to a left hand coordinate system. The operator **w** transforms the quaternion in the magnitude of the rotation angle and the sign of the ω_x term. This maps the quaternion $Q = (q_0, q_1, q_2, q_3)$ to $Q^* = (q_0, q_1, -q_2, -q_3)$.

$$\mathbf{w}Q = Q^*$$

$$\mathbf{w}\overrightarrow{\Theta}(Q_i) = \overrightarrow{\Theta}^*(Q_i^*)$$

$$\mathbf{w}\overrightarrow{\Gamma}(Q_i) = \overrightarrow{\Gamma}^*(Q_i^*)$$

The reflection operator **W** acts on whole body the configuration state vector.

$$\mathbf{W}\overrightarrow{\Psi} = \overrightarrow{\Psi}^*$$

This not only reflects the individual quaternions but switches left and right of the appendic-

ular vectors.

$$\overrightarrow{\Psi}^* = \begin{pmatrix} \overrightarrow{\Theta}^* \\ \overrightarrow{\Gamma}^*_{right} \\ \overrightarrow{\Gamma}^*_{left} \end{pmatrix}$$

We write the matrix form of body reflection operator $\mathbf{W} = \begin{pmatrix} \mathbf{w} & 0 & 0 \\ 0 & 0 & \mathbf{w} \\ 0 & \mathbf{w} & 0 \end{pmatrix}$ so that we may write the following.

$$\mathbf{W}\overrightarrow{\Psi} = \begin{pmatrix} \mathbf{w} & 0 & 0 \\ 0 & 0 & \mathbf{w} \\ 0 & \mathbf{w} & 0 \end{pmatrix} \begin{pmatrix} \overrightarrow{\Theta} \\ \overrightarrow{\Gamma}_{left} \\ \overrightarrow{\Gamma}_{right} \end{pmatrix} = \begin{pmatrix} \overrightarrow{\Theta}^* \\ \overrightarrow{\Gamma}^*_{right} \\ \overrightarrow{\Gamma}^*_{left} \end{pmatrix} = \overrightarrow{\Psi}^*$$

The three representations are of the original and reflected pose are shown together in Figure 8.

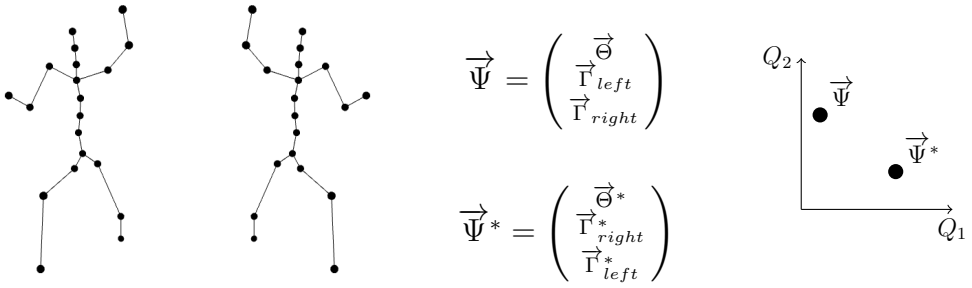

Figure 8: Reflected pose, state vector and point in $\mathcal{C}$.

2.11 Symmetry Coordinate Basis

We define an alternate basis of the conformation $\overrightarrow{\Psi}$ as follows.

$$\overrightarrow{S} = \frac{\overrightarrow{\Psi} + \overrightarrow{\Psi}^*}{2}$$

$$\overrightarrow{A} = \frac{\overrightarrow{\Psi} - \overrightarrow{\Psi}^*}{2}$$

By applying the reflection operator we see the following.

$$\mathbf{W}\overrightarrow{S} = \overrightarrow{S}$$

$$\mathbf{W}\overrightarrow{A} = -\overrightarrow{A}$$

$\overrightarrow{S}$ is invariant to the reflection operator $\mathbf{W}$ so it is the symmetric component of $\overrightarrow{\Psi}$. The sign of $\overrightarrow{A}$ is flipped by the application of the reflection operator $\mathbf{W}$ so it is termed the anti-symmetric component of $\overrightarrow{\Psi}$.

The configuration state of the body $\overrightarrow{\Psi}$ may be written in terms of these symmetric and antisymmetric components.

$$\overrightarrow{\Psi} = \overrightarrow{S} + \overrightarrow{A}$$

If the anti-symmetric component of the configuration state is zero, $\overrightarrow{A} = 0$, then the configuration is fully symmetric, $\overrightarrow{\Psi} = \overrightarrow{S}$, and is equal to it's mirror image, $\overrightarrow{\Psi} = \overrightarrow{\Psi}^*$.

If the anti-symmetric component of the configuration state is non-zero, $\overrightarrow{A} \neq 0$, then the configuration is chiral and there exists a mirror image configuration $\overrightarrow{\Psi}^* \in \mathcal{C}_{free}$ which is obtained by flipping the sign of $\overrightarrow{A}$.

Here we split $\mathcal{C}$ into two subspaces spanned by $\overrightarrow{S}$ and $\overrightarrow{A}$. The symmetric and anti-symmetric subspaces are shown in Figure 9. We refer to them jointly as the symmetry subspaces.

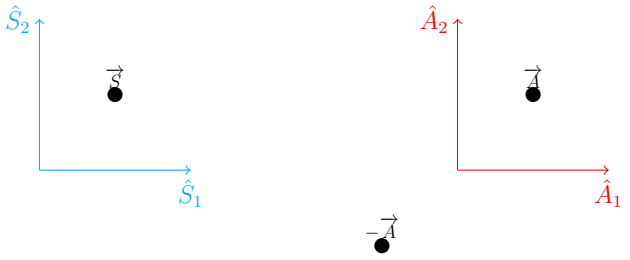

Figure 9: Symmetry Subspaces of $\mathcal{C}$

We combine both subspaces together in the same graph, while keeping them orthogonal. In the combined symmetry basis $\overrightarrow{\Psi}$ and $\overrightarrow{\Psi}^*$ are reflected through the vertical symmetry axis. This is shown in Figure 10. We refer to this depiction of $\mathcal{C}$ as the composite graph.

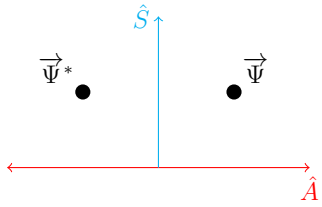

Figure 10: Combined Symmetry Basis of $\mathcal{C}$

2.12 Symmetric States

A symmetric pose is one which is invariant to the reflection operator since it is identical to it's mirror image or $\overrightarrow{\Psi} = \overrightarrow{\Psi}^*$. In such a state the left side of the body is doing the same thing as the right side of the body. A symmetric state is shown in Figure 11.

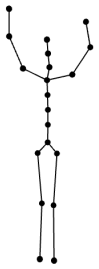

Figure 11: Symmetric State

It follows from $\overrightarrow{\Psi} = \overrightarrow{\Psi}^*$ that the antisymmetric component of a symmetric pose is zero. $\overrightarrow{A} = 0$ Therefore the symmetric state point in $\mathcal{C}$ projects on to the origin of the antisymmetric subspace and the state can be represented completely by its location in the symmetric subspace. This is shown in Figure 12

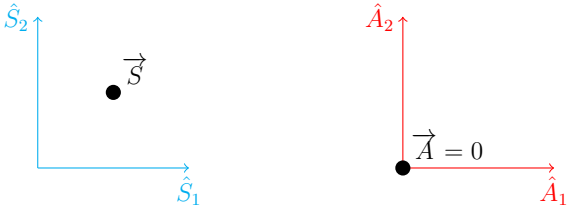

Figure 12: Symmetry Subspaces of $\mathcal{C}$

Seen from the view of the combined symmetry basis the symmetric state resides on the

vertical symmetry axis. This is shown in Figure 13.

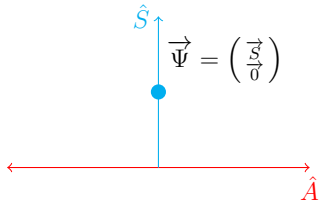

Figure 13: Combined Symmetry Basis of $\mathcal{C}$

2.13 Distance Metric

In order to compare two configuration states, $\vec{\Psi}_a$ and $\vec{\Psi}_b$, we define a distance function or metric. We begin by using a metric to compare each rigid element separately and then combine these distance functions to generate a distance metric comparing whole states of the whole body. A distance metric measuring the difference between two poses is depicted in Figure 14.

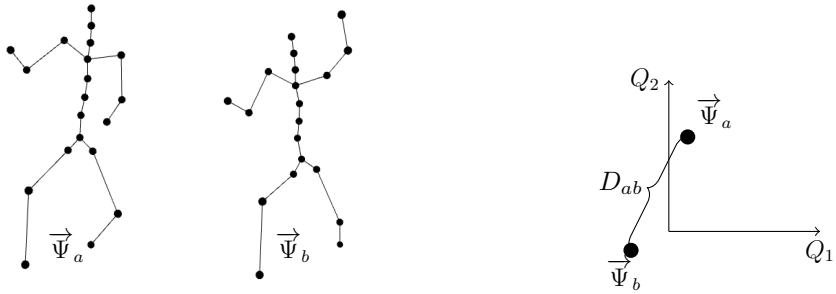

Figure 14: Distance Measure Between Two States in $\mathcal{C}$

We follow the usual definition for metrics as a map $D : \mathcal{C} \times \mathcal{C} \to \mathbb{R}$ satisfying the following four axioms. [28]

1. $D(x, y) \geq 0$ (non-negativity)
2. $D(x, y) = 0 \Leftrightarrow x = y$ (indiscernability)
3. $D(x, y) = D(y, x)$ for $x, y \in \mathcal{C}$ (symmetry)

4. $D(x,z) \leq D(x,y) + D(y,z)$ for $x, y \in \mathcal{C}$ (subadditivity)

We use the inner product of quaternions as our metric for comparing the rotational states of rigid elements. We define the inner product operator for quaternions as follows. [28]

$$Q \circ G = q_0 g_0 + q_1 g_1 + q_2 g_2 + q_3 g_3$$

We use the inner product of quaternions to derive a distance metric based solely on the rotational states of a particular rigid body element.

$$D(Q_a, Q_b) = 1 - Q_a \circ Q_b$$

This metric gives values in the range [0,1] and is only a measure in SO(3).

In considering metrics between whole body configurations we can simply take the weighted sum of metrics for individual links.

$$D(\overrightarrow{\Psi}_a, \overrightarrow{\Psi}_b) = \Sigma_i w_i D(Q_{ai}, Q_{bi})$$

This whole body metric gives values in the range $[0,\Sigma_i w_i]$. It measures the difference between two different states of the body $\overrightarrow{\Psi}_a$ and $\overrightarrow{\Psi}_b$. For this work we use a normalized metric of equal weighting. The states are normalized, $\overrightarrow{\Psi}_a \circ \overrightarrow{\Psi}_a = 1$.

$$D_{ab} = 1 - \overrightarrow{\Psi}_a \circ \overrightarrow{\Psi}_b$$

2.14 Double Metric

A pseudometric follows non-negativity and symmetry but lacks the indiscernability of proper metrics. Here we introduce the reflection pseudometric D^*_{ab}. This is the metric distance

between a state $\overrightarrow{\Psi}_a$ and the reflection of state $\overrightarrow{\Psi}_b$.

$$D^*_{ab} = 1 - \overrightarrow{\Psi}_a \circ \overrightarrow{\Psi}^*_b$$

We define the double metric as the set of values D_{ab} and D^*_{ab}. This is diagramed in Figure 15.

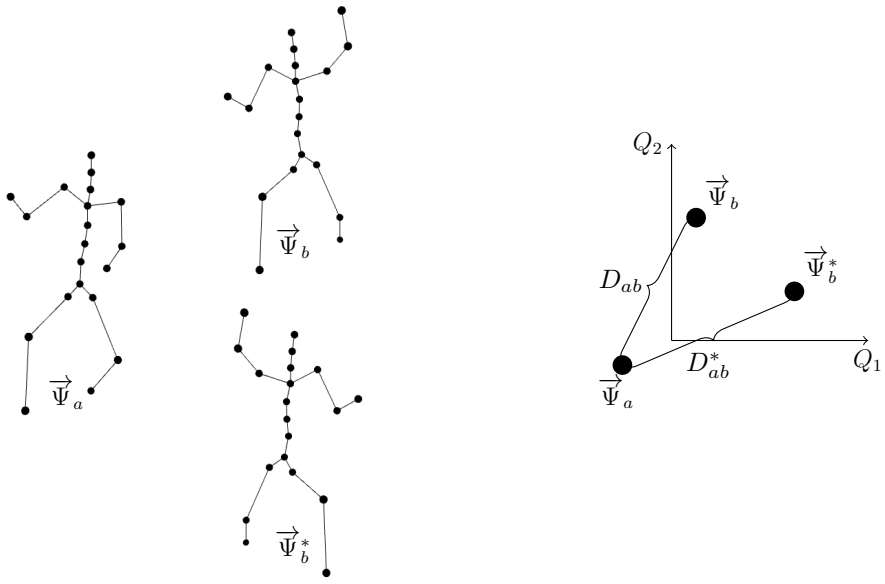

Figure 15: Distance Measure Between Two States in $\mathcal{C}$

Since $\overrightarrow{A}$ and $\overrightarrow{S}$ are orthogonal, representing $\overrightarrow{\Psi}$ in the symmetry basis yields the following identities.

$$\overrightarrow{\Psi}_a \circ \overrightarrow{\Psi}_b = \overrightarrow{S}_a \circ \overrightarrow{S}_b + \overrightarrow{A}_a \circ \overrightarrow{A}_b$$

$$\overrightarrow{\Psi}_a \circ \overrightarrow{\Psi}^*_b = \overrightarrow{S}_a \circ \overrightarrow{S}_b - \overrightarrow{A}_a \circ \overrightarrow{A}_b$$

It follows that if the reflection metric between a state and itself is zero, $D^*_{aa} = 0$, then $\overrightarrow{\Psi}_a = \overrightarrow{\Psi}^*_a$ and that $\overrightarrow{\Psi}_a$ is a symmetric state.

2.15 Motion Paths

Now we consider kinematic states as functions of time $\Psi(t)$. We note time as made of discrete points over an index, t_i. We call $\underrightarrow{t_a t_b}$ the linear set of points from t_a to t_b. The direction of the underarrow is used to notate the direction of time.

$\Psi(t_a)$ is the state vector at time t_a. The set of vectors from $\Psi(t_a)$ to $\Psi(t_b)$ is notated as $\Psi(\underrightarrow{t_a t_b})$. This represents a continuous path in $\mathcal{C}$ and is referred to as a motion path. A graph of motion path $\Psi(\underrightarrow{t_a t_b})$ in $\mathcal{C}$ is shown in Figure 16.

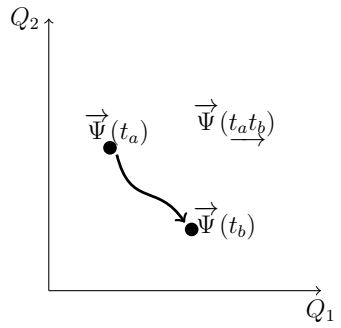

Figure 16: Motion Path Between Two States in $\mathcal{C}$

2.16 Motion Capture Data

Optical motion capture data is publicly available online from the Carnagie Mellon Motion Capture Lab. The kinematic chain model they use has a total of 62 degrees of freedom. It includes seven links for the axial skeleton. The appendicular skeleton consists of arms and legs. The arm chain links and DOF are clavicle(2), humerous(3), radius(1), wrist(1), hand(2), fingers(1) and thumb(2). The leg chain links and DOF are femur(3), tibia(1), foot(2), and toes(1).

Motion capture was used in the ASF/AMC format. The ASF data (Acclaim Skeleton File) describes the geometry of the kinematic chain. This includes the segment lengths and their linkage hierarchy. The AMC data (Acclaim Motion Capture) only consists of the joint angles

and the root position. Joint angles are reported by Euler angle in XYZ order of rotation. These are known as the Fick angles.

The AMC datafile gives a high dimensional timeseries. The Euler angles are reported for each frame of motion. Motion sequences are recorded at 120 frames per second. We convert this data into quaternion representation in order to get a time series motion path $\overrightarrow{\Psi}(\underrightarrow{tt})$. Simultaneously we extract the reflected state timeseries motion path $\overrightarrow{\Psi}^*(\underrightarrow{tt})$. We neglect hand and foot links and clavicle movement so that the motion capture data matches the model presented in this chapter.

3 Movement Analysis

In this chapter we analyze motion data using the mathematical tools presented in the previous chapter. The goals of this analysis are :

- Use the distance metrics D and D^* to develop a means of measuring the similarity between two body states $\overrightarrow{\Psi}_1$ and $\overrightarrow{\Psi}_2$. We call these similarity functions Z and Z^*.
- Use the similarity measures Z and Z^* to generate the similarity metric spaces Z_{ij} and Z^*_{ij} for a time series $\overrightarrow{\Psi}(t)$. We call Z_{ij} and Z^*_{ij} the similarity plots or motion spectra of $\overrightarrow{\Psi}(t)$.
- Analyze the motion spectra Z_{ij} and Z^*_{ij} to characterize $\overrightarrow{\Psi}(t)$ and its associated motion graph.

3.1 Similarity Function

Given the metrics D_{ab} and D^*_{ab} we create two functions to represent the similarity between two states $\overrightarrow{\Psi}_a$ and $\overrightarrow{\Psi}_b$. We call these Z_{ab} and Z^*_{ab}, the similarity function and anti-similarity function respectively. They are defined as follows.

$$Z_{ab}(\overrightarrow{\Psi}_a, \overrightarrow{\Psi}_b) = Ce^{-\beta D_{ab}}$$

$$Z^*_{ab}(\overrightarrow{\Psi}_a, \overrightarrow{\Psi}_b) = Ce^{-\beta D^*_{ab}}$$

Z_{ab} and Z^*_{ab} are in the range [0,1] where C is the normalization constant and β is a sensitivity constant.

Values of Z close to one indicate the two configurations are very similar.

$$Z_{ab} \approx 1 \rightarrow \overrightarrow{\Psi}_a \approx \overrightarrow{\Psi}_b$$

A configuration is always similar to itself.

$$Z_{aa} = 1$$

A configuration which is similar to its own mirror image is symmetric.

$$Z^*_{aa} \approx 1 \rightarrow \overrightarrow{\Psi}_a \approx \overrightarrow{\Psi}^*_a \approx \overrightarrow{S}_a$$

As Z_{ab} and Z^*_{ab} approach unity they behave as the quaternionic inner product between the states raised to the power of the sensitivity constant.

$$Z_{ab} \sim (\overrightarrow{\Psi}_a \circ \overrightarrow{\Psi}_b)^\beta$$

$$Z^*_{ab} \sim (\overrightarrow{\Psi}_a \circ \overrightarrow{\Psi}^*_b)^\beta$$

3.2 Similarity Matrices and Plots

Here we notate each motion path as a set of states over a time index, $\overrightarrow{\Psi}(t_i)$. We create a metric space by calculating the distance between each element of the set using the double index. $D_{ij} = D(\overrightarrow{\Psi}(t_i), \overrightarrow{\Psi}(t_j))$. Using this matrix of distance values this we create a 2D array Z_{ij} called the similarity matrix.

An example Z_{ij} from a three time point motion path is shown in Figure 17. The diagonal elements of the matrix are equal to one, $Z_{ii} = 1$, since all states are self similar. The matrix is also symmetric $Z_{ij} = Z_{ji}$. This follows from the symmetry property of the distance metric. An example Z_{ij} from a motion path including states $\overrightarrow{\Psi}(t_a)$ and $\overrightarrow{\Psi}(t_b)$ is shown in Figure 18. The diagonal elements of Z_{ij} are marked with an arrow and the symmetric feature of the matrix is shown explicitly. The kinematic model poses corresponding to $\overrightarrow{\Psi}(t_a)$ and $\overrightarrow{\Psi}(t_b)$ are shown on top and right.

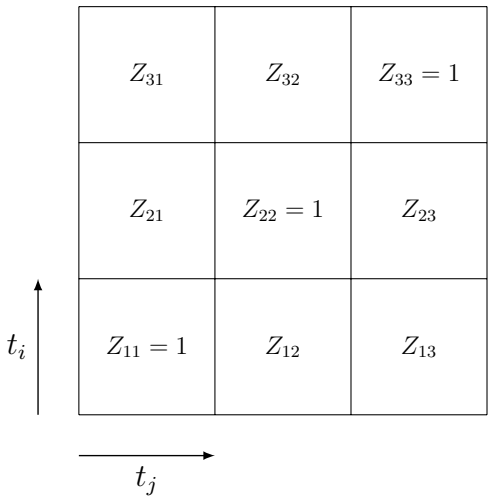

Figure 17: Three Time Point Z_{ij}

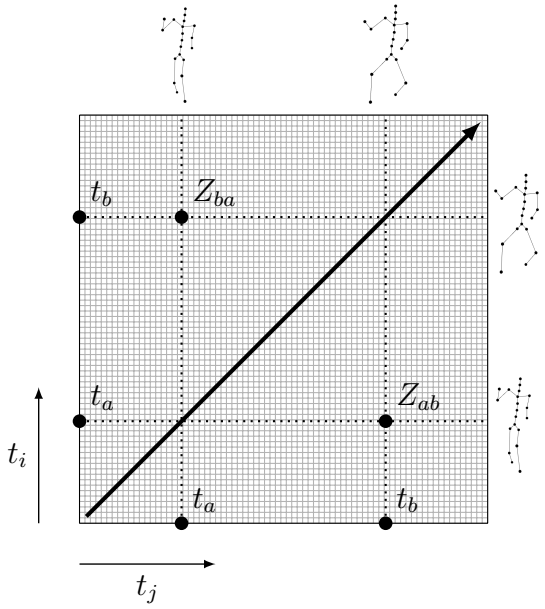

Figure 18: Representation of a Z_{ij} with many time points

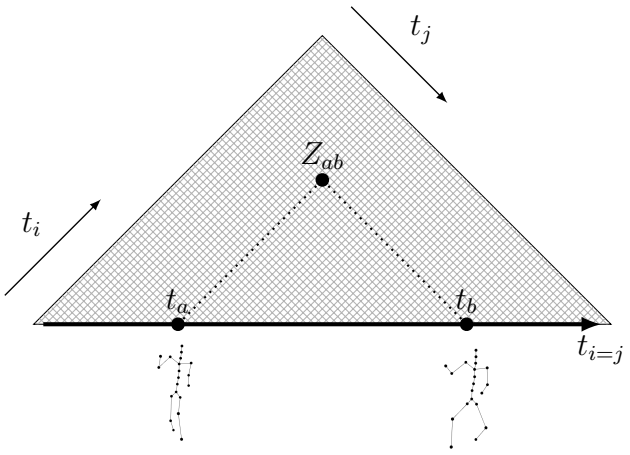

Figure 19: Compact representation of Z_{ij} is achieved by rotation

Since Z_{ij} is a symmetric matrix we can represent it more compactly as a triangle. Additionally we rotate the image 45 degrees so that the identity axis is horizontal. This horizontal axis is used as a $t_{i=j}$ time axis. From this view time runs horizontally to the right and similarity between states at various times is indicated by elements of the triangle. A diagram of such a rotated Z_{ij} triangle is shown in Figure 19.

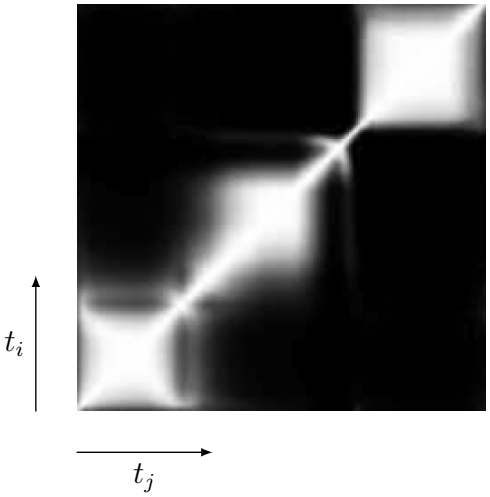

Figure 20: Similarity matrix Z_{ij} represented in greyscale

Mapping Z_{ij} matrix element values to greyscale values produces an image which conveys motion path information visually as shown in Figure 20. Z_{ij} values of 0 are mapped to black, 0 in the greyscale. Values of 1 are mapped to white, 256 in the greyscale. All Z_{ij}

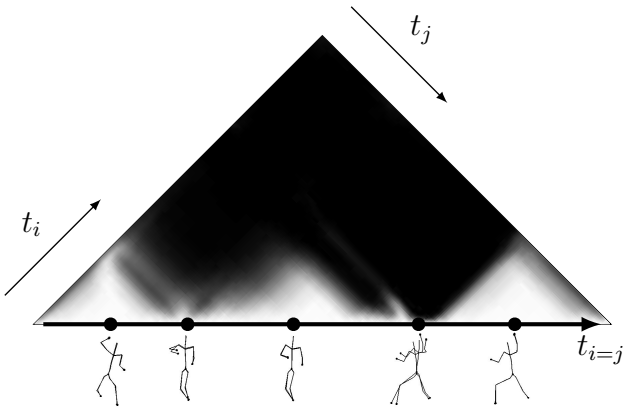

Figure 21: Kinematic displacement is related to the width Z_{ij} signal in the neighborhood of the identity axis

values between 0 and 1 are mapped to the greyscale linearly. The intensity of the Z_{ij} matrix element determines the similarity between $\overrightarrow{\Psi}(t_i)$ and $\overrightarrow{\Psi}(t_j)$. We call these images similarity plots or motion spectra. The light regions within them are referred to as proximity signals.

We call the diagonal elements of the similarity matrix Z_{ij} the identity axis since these are equal to one, as they are in the standard identity matrix.

$$Z_{ii} = 1$$

The elements near the identity axis are of interest because they give us insight into how the configuration state $\overrightarrow{\Psi}(t)$ changes over time.

We measure the magnitude of the time rate of change of the configuration state as follows.

$$|\frac{d\overrightarrow{\Psi}(t)}{dt}| = \frac{D(\overrightarrow{\Psi}(t_i), \overrightarrow{\Psi}(t_{i-1}))}{\Delta t}$$

Visually, on the motion spectra, this means the wider the identity axis appears to be the less displacement there is over time in state space and the more slowly the subject is moving. Said another way, the thinner the width of the identity axis the more displacement there is

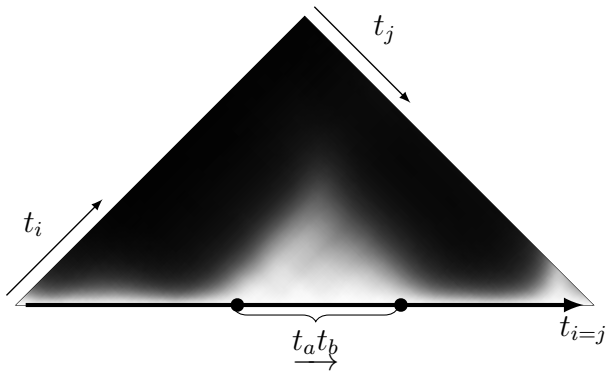

Figure 22: Kinematic displacement is related to the width Z_{ij} signal in the neighborhood of the identity axis

over time in state space and the more quickly the subject is moving. Figure 21 shows the rotated triangular version of the Z_{ij} image from Figure 20.

Below the $i = j$ similarity axis we show corresponding images of the kinematic chain model where at each time point we overlap models for states $\overrightarrow{\Psi}(t)$ and $\overrightarrow{\Psi}(t + \Delta)$. In this instance the Δ is 20 frames or a sixth of a second. It can be seen clearly that sections of the motion path with more displacement correspond to thinner width of the identity axis.

3.2.1 Stillness

The lack of displacement of the kinematic model over time can be interpreted as stillness. Though the model may not actually be still the kinematic states all reside within a certain region of $\mathcal{C}$ in which all points are within a certain proximity to one another. Therefore all points within this region will generate a metric space with elements all below a threshold value. This neighborhood of $\mathcal{C}$ can be represented by a single state. Continued presence in this region over time is described as stillness.

The Z_{ij} image for a section of stillness is shown in Figure 22. All of the Z_{ij} terms corresponding to the metric space of this set of poses are close to 1. In the image this manifests as a light triangle coming out of the identity axis between t_a and t_b. Over the time period $\underrightarrow{t_a t_b}$

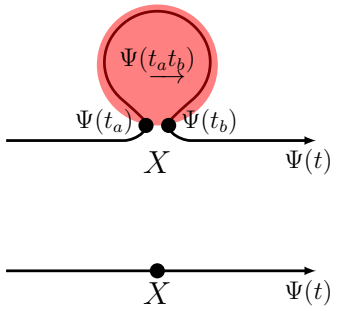

Figure 23: Graph of $\Psi(t)$ in $\mathcal{C}$ where the motion path includes stillness

all the states making up the motion path $\overrightarrow{\Psi}(\underrightarrow{t_a t_b})$ reside within an area of $\mathcal{C}$ we call X.

$$\Psi(\underrightarrow{t_a t_b}) \in X$$

$$\Psi(\underrightarrow{t_a t_b}) = \underrightarrow{x x_0}$$

In the upper part of Figure 23 we draw a graph of $\overrightarrow{\Psi}(t)$ and depict the region of $\mathcal{C}$ inhabited by $\overrightarrow{\Psi}(\underrightarrow{t_a t_b})$ as a red colored area. The lower part of Figure 23 shows the same graph with the states of $\overrightarrow{\Psi}(\underrightarrow{t_a t_b})$ collapsed onto a single node X.

We adopt a notation for naming this motion path using lower case letters to indicate the beginning and ending node of the path. The zero subscript is reserved for paths which remain on the node, indicating a still path.

3.2.2 State Repetition

Figure 24 shows a Z_{ij} plot in which a motion is executed which begins and ends in the same state in $\mathcal{C}$. The off diagonal region of lightness is a proximity signal indicating a similarity between $\Psi(t_a)$ and $\Psi(t_b)$.

In the upper part of Figure 25 we draw a graph of $\overrightarrow{\Psi}(t)$ and depict the region of $\mathcal{C}$ shared by $\overrightarrow{\Psi}(t_a)$ and $\overrightarrow{\Psi}(t_b)$ as a red colored area. The lower part of Figure 25 shows the same graph with the states of $\overrightarrow{\Psi}(t_a)$ and $\overrightarrow{\Psi}(t_b)$ collapsed onto a single node X. Both $\Psi(t_a)$ and

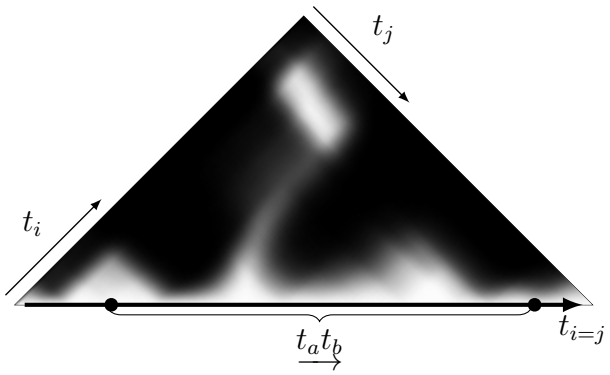

Figure 24: The return of a motion path to a previously inhabited region of $\mathcal{C}$ manifests an off diagonal proximity signal in Z_{ij} indicating $\Psi(t_a) \approx \Psi(t_b)$

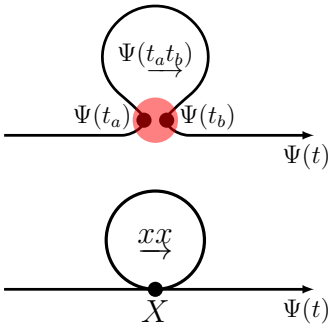

Figure 25: State Repetition

$\Psi(t_b)$ are elements of this region X and the looping motion path $\Psi(\underrightarrow{t_a t_b})$ is notated $\underrightarrow{xx}$ since it begins and ends in said region X.

$$\Psi(t_a), \Psi(t_b) \in X$$

$$\Psi(\underrightarrow{t_a t_b}) = \underrightarrow{xx}$$

3.2.3 Path Repetition

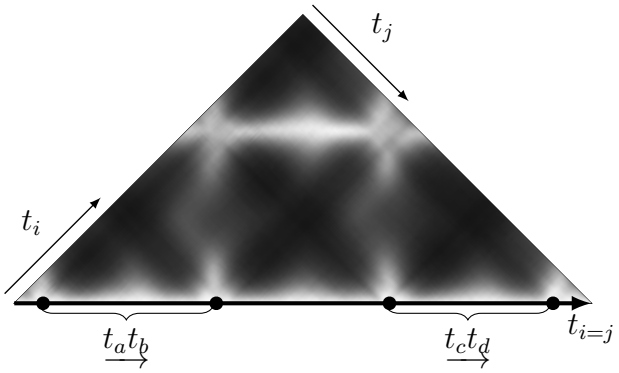

Figure 26: The return of a motion path along previously carved path in $\mathcal{C}$ manifests an off diagonal proximity signal in Z_{ij} parallel to the identity axis indicating $\Psi(t_a t_b) \approx \Psi(t_c t_d)$

Figure 26 shows a Z_{ij} plot in which two motion paths travel along the same route in $\mathcal{C}$. The off diagonal horizontal light region indicates a similarity between $\Psi(\underrightarrow{t_a t_b})$ and $\Psi(\underrightarrow{t_c t_d})$. An off diagonal signal which looks like the identity axis signal is the visual motif of path repetition.

In the upper part of Figure 27 we draw a graph of $\Psi(t)$, depicting the region of $\mathcal{C}$ shared by $\Psi(t_a)$ and $\Psi(t_c)$ as a red colored area and the region of $\mathcal{C}$ shared by $\Psi(t_b)$ and $\Psi(t)$ as a blue colored area. We name the region X that in which $\Psi(t_a) \approx \Psi(t_c)$ and name the region Y that in which $\Psi(t_b) \approx \Psi(t_d)$.

$$\Psi(t_a), \Psi(t_c) \in X$$

$$\Psi(t_b), \Psi(t_d) \in Y$$

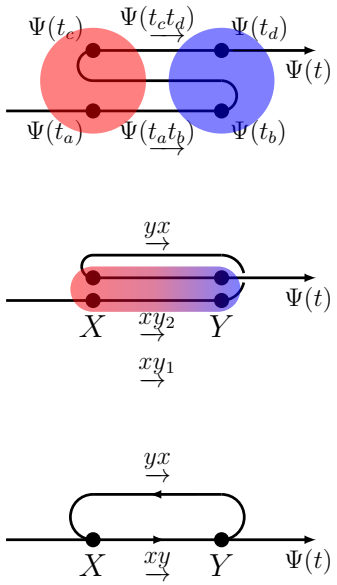

Figure 27: Path Repetition

We name the motion path $\overrightarrow{\Psi}(\overrightarrow{t_b t_c})$ as $\overrightarrow{yx}$. The motion paths $\overrightarrow{\Psi}(\overrightarrow{t_a t_b})$ and $\overrightarrow{\Psi}(\overrightarrow{t_c t_d})$ are named $\overrightarrow{xy_1}$ and $\overrightarrow{xy_2}$ respectively. In the middle part of Figure 27 we color the route in $\mathcal{C}$ shared by $\overrightarrow{xy_1}$ and $\overrightarrow{xy_2}$ using a red to blue gradient. We name this shared route $\overrightarrow{xy}$.

$$\Psi(\overrightarrow{t_a t_b}), \Psi(\overrightarrow{t_c t_d}) \in \overrightarrow{xy}$$

The lower part of Figure 25 shows the same graph with the states $\Psi(t_a)$ and $\Psi(t_b)$ collapsed onto a single node X and the states $\Psi(t_c)$ and $\Psi(t_d)$ collapsed onto a single node Y. The paths $\overrightarrow{xy_1}$ and $\overrightarrow{xy_2}$ are also collapsed onto a single path $\overrightarrow{xy}$.

3.2.4 Path Reversal

Figure 28 shows a Z_{ij} plot in which two motion paths travel along the same route in $\mathcal{C}$ but in opposite directions. More specifically the overall motion is palindindromic: a movement is performed from beginning to end and then repeated backwards in time, from the end to the beginning. The proximity signal projecting vertically out from the identity axis indicates a

similarity between $\Psi(\underrightarrow{t_a t_b})$ and the time reversed version of $\Psi(\underrightarrow{t_b t_c})$.

$$\Psi(\underrightarrow{t_a t_b}) \approx \Psi(\underleftarrow{t_b t_c})$$

We notate this time reversal using a left under arrow. An off diagonal signal which looks like the identity axis signal but projected perpendicular to it is the visual motif of time reversed path repetition.

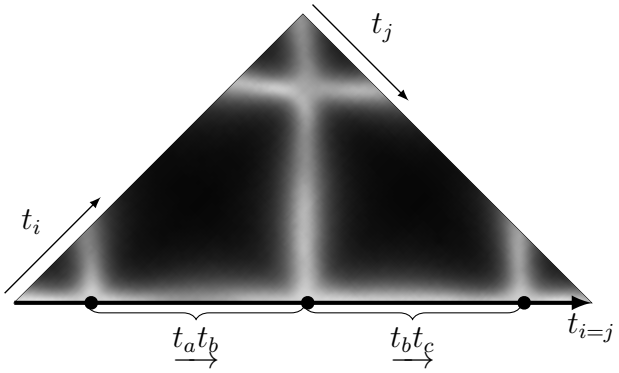

Figure 28: A motion path traversal of a previously carved path in $\mathcal{C}$ performed in reverse manifests a proximity signal in Z_{ij} that projects perpendicularly out from the identity axis.

In the upper part of Figure 29 we draw a graph of $\Psi(t)$, depicting the region of $\mathcal{C}$ shared by $\Psi(t_a)$ and $\Psi(t_c)$ as a red colored area and the region of $\mathcal{C}$ inhabited by the reversal state $\Psi(t_b)$ as a blue colored area. We name the region X that in which $\Psi(t_a) \approx \Psi(t_c)$ and name the region Y that in which the motion path $\Psi(\underrightarrow{t_a t_b})$ ends and reverses direction.

$$\Psi(t_a), \Psi(t_c) \in X$$

$$\Psi(t_b) \in Y$$

We name the motion path $\overrightarrow{\Psi}(\underrightarrow{t_a t_b})$ as $\underrightarrow{xy}$ and the motion path $\overrightarrow{\Psi}(\underrightarrow{t_b t_c})$ as $\underrightarrow{yx}$. In the middle part of Figure 29 we color the route in $\mathcal{C}$ shared by $\underrightarrow{xy}$ and $\underrightarrow{yx}$ using a red to blue gradient. We name this shared route $\underleftrightarrow{xy}$. The double sided arrow is used to indicate the motion path

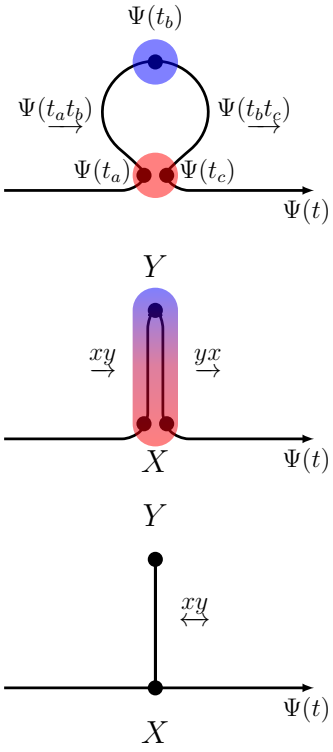

Figure 29: This series of images represents the generation of the motion graph for a palindromic motion path in $\mathcal{C}$.

route can be traversed in either direction.

$$\Psi(\underrightarrow{t_a t_b}), \Psi(\underrightarrow{t_b t_c}) \in \underleftrightarrow{xy}$$

The lower part of Figure 29 shows the same graph with the states $\Psi(t_a)$ and $\Psi(t_b)$ collapsed onto a single node X. The paths $\underrightarrow{xy}$ and $\underrightarrow{yx}$ are also collapsed onto a single time reversible path $\underleftrightarrow{xy}$.

3.3 Anti-Similarity Matrices and Plots

Here we introduce the concept of the anti-similarity matrix and anti-similarity plot. Again we have a configuration state time series represented as a set of states over a time index, $\overrightarrow{\Psi}(t_i)$. We create a pseudometric space by calculating the distance between each element of the set using the double index where we reflect one of the states.

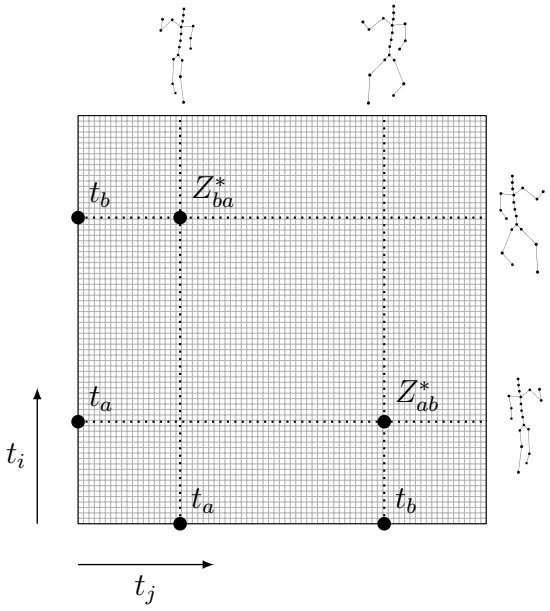

Figure 30: Representation of a Z^*_{ij} with many time points

$$D^*_{ij} = D(\overrightarrow{\Psi}(t_i), \overrightarrow{\Psi}^*(t_j))$$

Using this matrix of distance values we create a 2D array for Z^*_{ij}. We call this the anti-similarity matrix. The corresponding image form of the matrix which maps matrix elements to greyscale pixel values is referred to as the anti-similarity plot or Z^* plot.

The pseudo metric space D^*_{ij} has the symmetry property of metrics, namely $D^*_{ij} = D^*_{ji}$. It follows that the Z^* matrix, like the Z matrix, is symmetric.

$$Z^*_{ij} = Z^*_{ji}$$

Since D^*_{ij} is a pseudo metric and does not have the property of indiscernability, $D^*_{ii} \neq 0$, it follows that the diagonal elements of the anti similarity matrix are not necessarily equal to one. If it is the case that over some index the diagonal elements of the anti similarity matrix are one it means that the set of configuration states is symmetric.

$$Z^*_{ii} = 1 \longleftrightarrow \overrightarrow{\Psi}(t_i) = \overrightarrow{\Psi}^*(t_i)$$

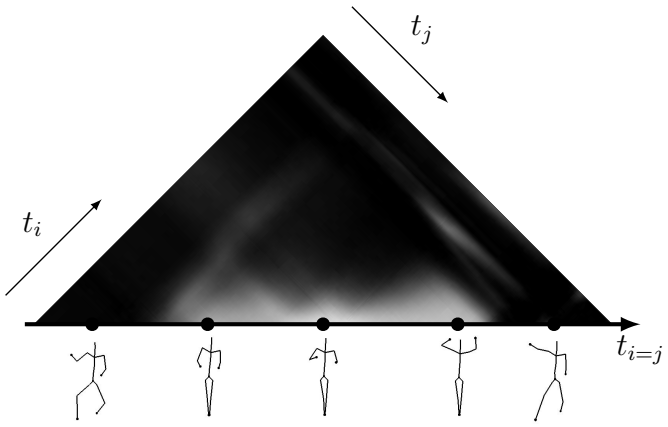

Figure 31: Symmetric configuration states are associated with a proximity signal along the identity axis of the anti-similarity plot

3.4 Similarity/Anti-Similarity Plots (Z/Z^* Plots)

In order to visualize the Z and Z^* plots simultaneously we use orthogonal color vectors, red and cyan, to plot Z and Z^* respectively. When the proximity signals of Z and Z^* overlap we get the addition of red and cyan to generate a grey signal. In the case that $Z_{ij} = 1$ and $Z^*_{ij} = 1$ we know that we have repetition and symmetry. This corresponds visually to a white proximity signal in the Z/Z^* plot.

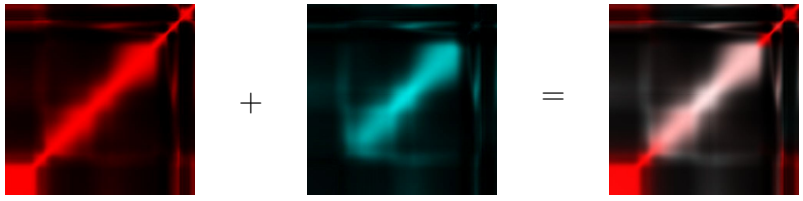

Figure 32: The addition of the similarity and anti-similarity plots with Z on the red color channel and Z^* on the green and blue color channels (cyan) generates the Z/Z^* plot.

3.4.1 Symmetry Path

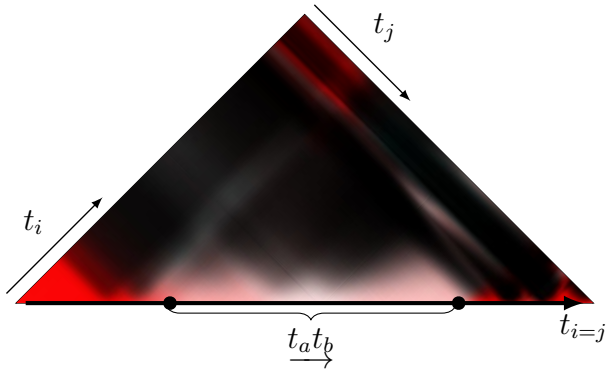

Figure 33: The overlap of proximity signals along the identity axis of Z and Z^* generates a white signal along the identity axis of the Z/Z^* plot between t_a and t_b. This indicates a symmetric motion path during this period of time.

Taking the composite Z/Z^* plot in Figure 32 we generate the triangular plot in the Figure 33. The white identity axis t_a and t_b indicates $\Psi(\underrightarrow{t_a t_b})$ resides completely within the

symmetric subspace of $\mathcal{C}$ and remains at the origin of the antisymmetric subspace.

$$\Psi(\underrightarrow{t_a t_b}) = S(\underrightarrow{t_a t_b})$$

$$A(\underrightarrow{t_a t_b}) = 0$$

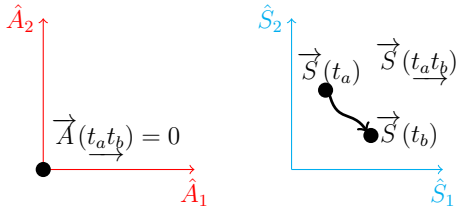

Figure 34: The symmetric motion path graphed in the symmetric and antisymmetric subspaces.

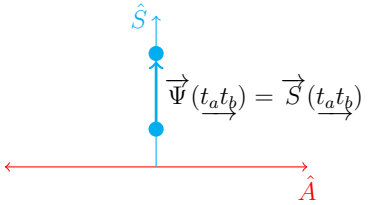

Figure 35: The symmetric motion path drawn in the composite graph. The path resides within the space of the symmetry axis.

The symmetric motion path is represented graphically in the two subspaces in Figure 34. Figure 35 shows the symmetric motion path in the composite basis of $\mathcal{C}$.

3.4.2 Reflected State Repetition

This section presents the Z/Z^* plot and motion graphs for the motif of a motion path which proceeds through a series of asymmetric configuration states and ends in a state which is the reflection of that state in which it started. Figure 36 shows the composition of the Z/Z^* plot from the addition of the Z and Z^* plot. We generate the corresponding triangular plot in 37. The red identity axis indicates $\Psi(\underrightarrow{t_a t_b})$ does not pass through a symmetry state. The

off axis proximity signal indicates a similarity between $\Psi(t_a)$ and $\Psi(t_b)$.

$$\forall\ i : \Psi(t_i) \neq \Psi^*(t_i)$$

$$\Psi(t_a) = \Psi^*(t_b)$$

The symmetric motion path is represented graphically in the two subspaces in Figure 38.

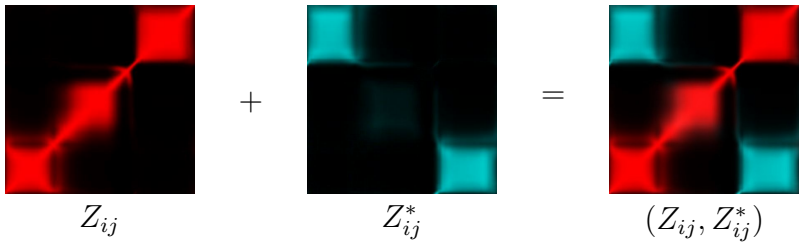

Figure 36: This is the composition of the Z/Z^* plot for a motion path which ends at the reflected state of that which it started.

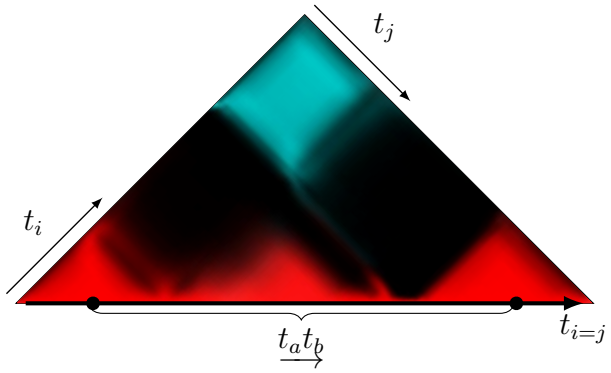

Figure 37: The triangular Z/Z^* shows a red identity axis indicating asymmetric motion. The off axis proximity signal indicates reflected state repetition.

Figure 39 shows the symmetric motion path in the composite basis of $\mathcal{C}$.

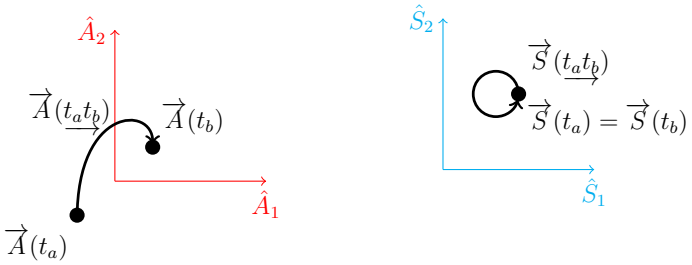

Figure 38: The motion path ending with reflected state repetition graphed in the symmetric and antisymmetric subspaces.

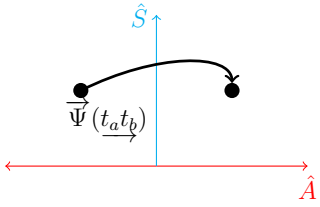

Figure 39: The motion path ending with reflected state repetition graphed in the composite basis.

3.4.3 Symmetric Motion Cycle

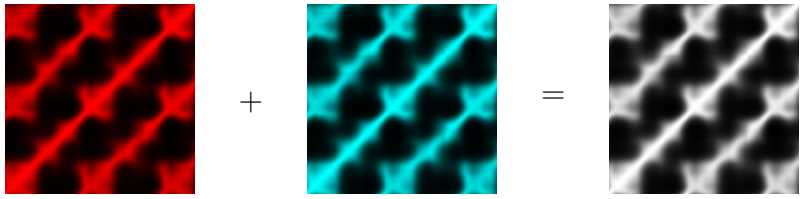

Figure 40: This is the composition of the Z/Z^* plot for a motion path which is symmetric and ends in the state in which it started. The motion cycle is repeated.

This section presents the Z/Z^* plot and motion graphs for the motif of a motion path which proceeds through a series of symmetric configuration states and ends in a state which is similar to that in which it started. We call this a symmetric motion cycle. The motion cycle is repeated.

Figure 40 shows the composition of the Z/Z^* plot from the addition of the Z and Z^* plot. We generate the corresponding triangular plot in Figure 41. The white identity axis indicates all the states of $\Psi(\underrightarrow{t_a t_b})$ are symmetric. The off axis proximity signal at $(Z/Z^*)_{ab}$ indicates a similarity between $\Psi(t_a)$ and $\Psi(t_b)$. Together these indicate a symmetric motion cycle.

$$A(\underrightarrow{t_a t_b}) = 0$$

$$\Psi(t_a) = \Psi(t_b)$$

The horizontal off axis proximity signal, parallel to the identity axis, indicates path repetition.

$$\Psi(\underrightarrow{t_a t_b}) = \Psi(\underrightarrow{t_b t_c})$$

The symmetric motion cycle is represented graphically in the two subspaces in Figure 42. Figure 43 shows the symmetric motion cycle in the composite basis of $\mathcal{C}$. The path is graphed in cyan to indicate its symmetry.

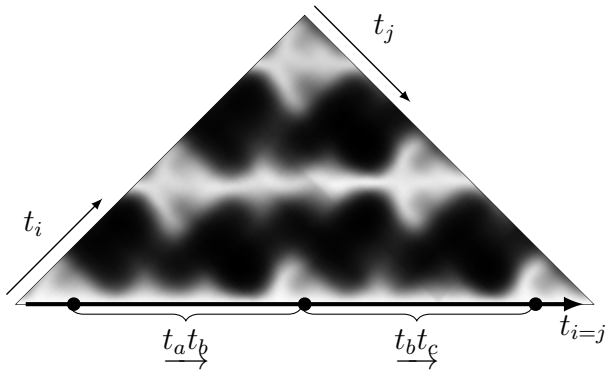

Figure 41: The triangular Z/Z^* shows a white identity axis indicating symmetric motion. The off axis proximity signal parallel to the identity axis indicates path repetition.

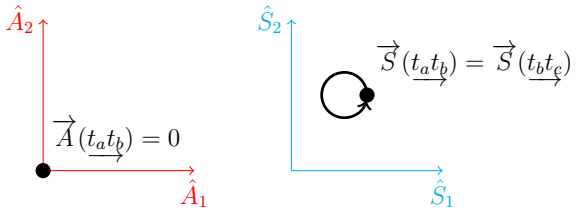

Figure 42: The symmetric motion cycle graphed in the symmetric and antisymmetric subspaces.

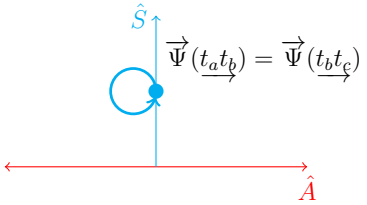

Figure 43: The symmetric motion cycle graphed in the composite basis. Symmetric states are drawn in cyan.

3.4.4 Asymmetric Motion Cycle

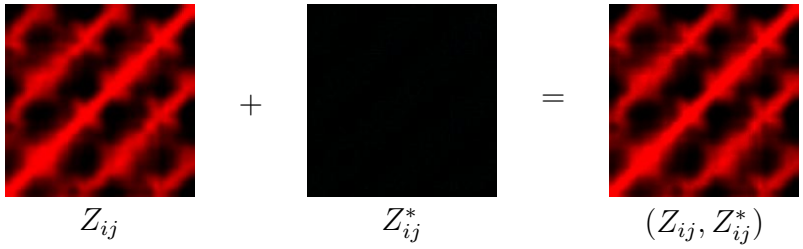

Figure 44: This is the composition of the Z/Z^* plot for a motion path which is asymmetric and ends in the state in which it started. The motion cycle is repeated.

This section presents the Z/Z^* plot and motion graphs for the motif of a motion path which proceeds through a series of asymmetric configuration states and ends in a state which is similar to that in which it started. We call this an asymmetric motion cycle. The motion cycle is repeated.

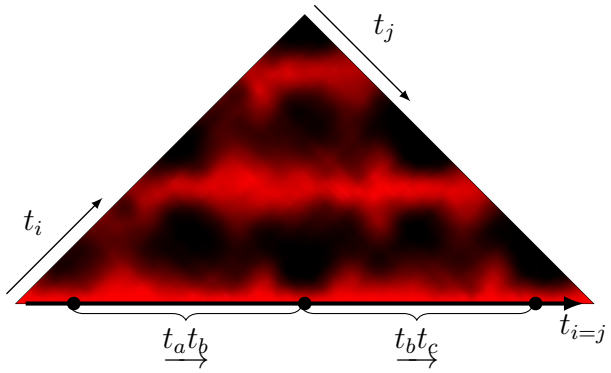

Figure 45: The triangular Z/Z^* shows a red identity axis indicating asymmetric motion. The off axis proximity signal parallel to the identity axis indicates path repetition.

Figure 44 shows the composition of the Z/Z^* plot from the addition of the Z and Z^* plot. We generate the corresponding triangular plot in Figure 45. The red identity axis indicates all the states of $\Psi(\underrightarrow{t_a t_b})$ are asymmetric. The off axis proximity signal at $(Z/Z^*)_{ab}$ indicates a similarity between $\Psi(t_a)$ and $\Psi(t_b)$. Together these indicate an asymmetric motion cycle.

$$\forall\ i : \Psi(t_i) \neq \Psi^*(t_i)$$

$$\Psi(t_a) = \Psi(t_b)$$

The horizontal off axis proximity signal, parallel to the identity axis, indicates path repetition.

$$\Psi(\underrightarrow{t_a t_b}) = \Psi(\underrightarrow{t_b t_c})$$

The asymmetric motion cycle is represented graphically in the two subspaces in Figure 46. Figure 47 shows the asymmetric motion cycle in the composite basis of $\mathcal{C}$. The reflected paths are drawn in light grey.

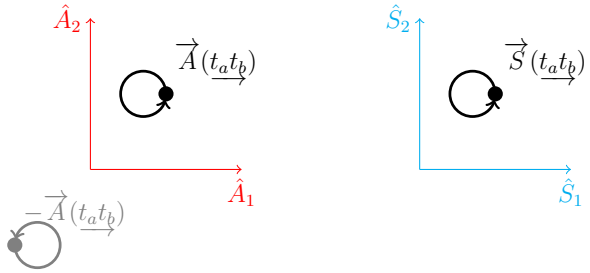

Figure 46: The asymmetric motion cycle graphed in the symmetric and antisymmetric subspaces.

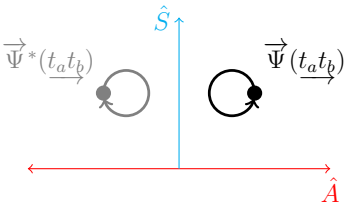

Figure 47: The asymmetric motion cycle graphed in the composite basis. The inferred reflected path is drawn in light grey.

3.4.5 Symmetric Palindromic Motion

This section presents the Z/Z^* plot and motion graphs for the motif of a motion path which proceeds through a series of symmetric configuration states, stopping half way through and returning along the same route in $\mathcal{C}$. This motion path is termed palindromic since it is invariant to time reversal.

Figure 48: This is the composition of the Z/Z^* plot for a motion path which is symmetric and palindromic.

Figure 48 shows the composition of the Z/Z^* plot from the addition of the Z and Z^* plot. We generate the corresponding triangular plot in 49. The white identity axis indicates all the states of $\Psi(\underrightarrow{t_a t_c})$ are symmetric.

$$\forall\ i : \Psi(t_i) = \Psi^*(t_i)$$

The vertical off axis proximity signal, perpendicular to the identity axis, indicates path repetition in the reverse time direction.

$$\Psi(\underrightarrow{t_a t_b}) = \Psi(\underleftarrow{t_b t_c})$$

The symmetric palindromic motion cycle is represented graphically in the two subspaces in

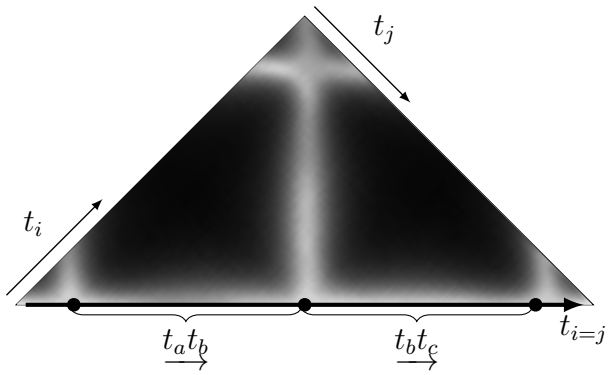

Figure 49: The triangular Z/Z^* shows a white identity axis indicating symmetric motion. The off axis proximity signal perpendicular to the identity axis indicates path repetition in the reverse time direction.

Figure 50. Since the path is symmetric the components of the configuration states in the anti-symmetric subpace remain at the origin. Figure 51 shows the symmetric palindromic motion cycle in the composite basis of $\mathcal{C}$.

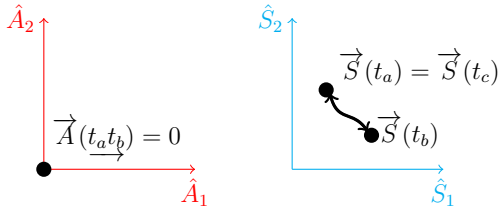

Figure 50: The symmetric palindromic motion cycle graphed in the symmetric and antisymmetric subspaces.

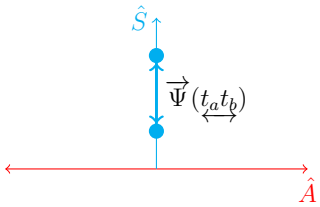

Figure 51: The symmetric palindromic motion cycle graphed in the composite basis. Symmetric states are graphed in cyan. Reversible paths are drawn as bidirectional arrows.

3.4.6 Asymmetric Palindromic Motion

This section presents the Z/Z^* plot and motion graphs for the motif of a motion path which proceeds through a series of asymmetric configuration states, stopping half way through and returning along the same route in $\mathcal{C}$. Again, this motion path is termed palindromic since it is invariant to time reversal. Figure 52 shows the composition of the Z/Z^* plot from the addition of the Z and Z^* plot. We generate the corresponding triangular plot in Figure 53. The red identity axis indicates all the states of $\Psi(\underrightarrow{t_a t_c})$ are asymmetric.

$$\forall\ i : \Psi(t_i) \neq \Psi^*(t_i)$$

Figure 52: This is the composition of the Z/Z^* plot for a motion path which is asymmetric and palindromic.

The vertical off axis proximity signal, perpendicular to the identity axis, indicates path repetition in the reverse time direction.

$$\Psi(\underrightarrow{t_a t_b}) = \Psi(\underleftarrow{t_b t_c})$$

The asymmetric palindromic motion cycle is represented graphically in the two subspaces

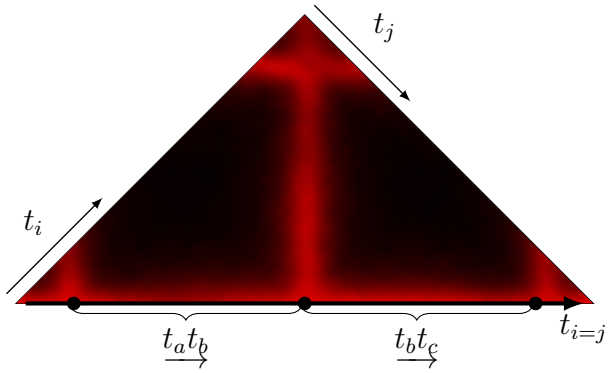

Figure 53: The triangular Z/Z^* shows a red identity axis indicating asymmetric motion. The off axis proximity signal perpendicular to the identity axis indicates path repetition in the reverse time direction.

in Figure 54. Figure 55 shows the asymmetric palindromic motion cycle in the composite basis of $\mathcal{C}$.

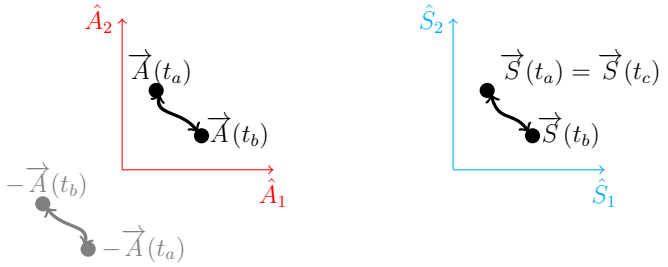

Figure 54: The asymmetric palindromic motion cycle graphed in the symmetric and anti-symmetric subspaces. The inferred reflected configuration states are drawn in grey.

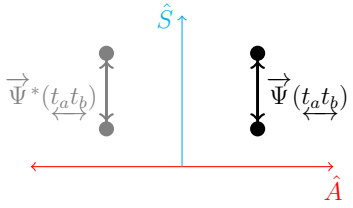

Figure 55: The symmetric palindromic motion cycle graphed in the composite basis. The inferred reflected configuration states are drawn in grey.

3.4.7 Anti-phase Motion

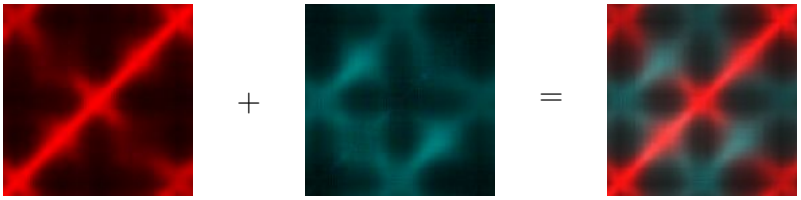

Figure 56: This is the composition of the Z/Z^* plot for an anti-phase motion path cycle.

This section presents the Z/Z^* plot and motion graphs for the motif of a motion path which proceeds through a series of configuration states and then repeats them on the other side. In other words the complete motion cycle consists of a movement phrase which is performed and then the reflected version of that phrase is performed. This kind of movement is referred to as anti-phase motion.

Figure 56 shows the composition of the Z/Z^* plot from the addition of the Z and Z^* plot. We generate the corresponding triangular plot in 57. The red identity axis indicates all the states of $\Psi(\underrightarrow{t_a t_c})$ are asymmetric.

$$\forall\ i : \Psi(t_i) \neq \Psi^*(t_i)$$

The cyan horizontal off axis proximity signal, parallel to the identity axis, indicates reflected path repetition.

$$\Psi(\underrightarrow{t_a t_b}) = \Psi^*(\underrightarrow{t_b t_c})$$

The red off axis proximity signal, $(Z/Z^*)_{ac}$, at the top of the triangle indicates the whole motion path $\Psi(\underrightarrow{t_a t_c})$ is cyclic.

$$\Psi(t_a) = \Psi(t_c)$$

The anti-phase motion cycle is represented graphically in the two subspaces in Figure 58. Figure 59 shows the anti-phase motion cycle in the composite basis of $\mathcal{C}$.

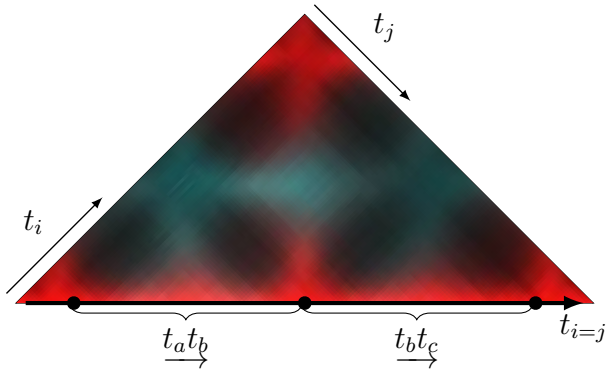

Figure 57: The triangular Z/Z^* shows anti-phase motion. The red identity axis indicates asymmetric motion while the horizontal cyan proximity signal, parallel to the identity axis, indicates reflected path repetition. The red off axis signal indicates overall path is a cycle.

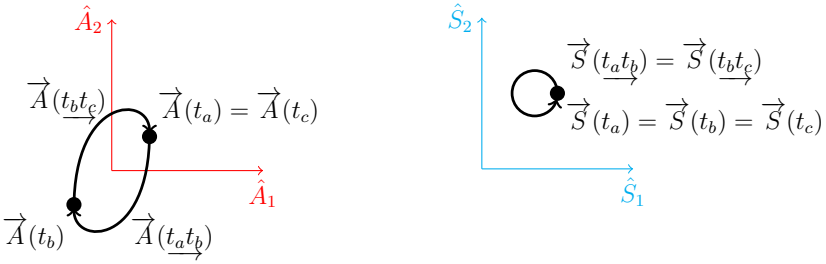

Figure 58: The anti-phase motion cycle graphed in the symmetric and antisymmetric subspaces.

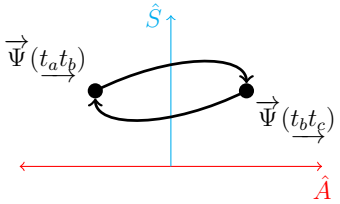

Figure 59: The anti-phase motion cycle graphed in the composite basis.

3.4.8 Anti-palindromic Motion

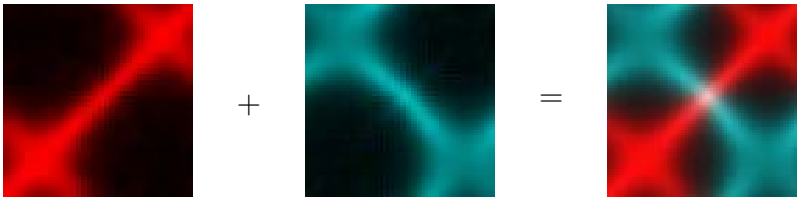

Figure 60: This is the composition of the Z/Z^* plot for an anti-phase motion path cycle.

This section presents the Z/Z^* plot and motion graphs for the motif of a motion path which proceeds through a series of configuration states and then repeats them on the other side, reversed in time. In this way it is similar to anti-phase motion. In other words the complete motion cycle consists of a movement phrase which is performed and then the reflected version of that phrase is performed reversed in time. For this reason we term this type of motion as anti-palindromic. This type of motion must pass through a symmetric state.

Figure 60 shows the composition of the Z/Z^* plot from the addition of the Z and Z^* plot. We generate the corresponding triangular plot in 61. The cyan vertical off axis proximity signal, perpendicular to the identity axis, indicates reflected path repetition reversed in time.

$$\Psi(\underrightarrow{t_a t_b}) = \Psi^*(\underleftarrow{t_b t_c})$$

The white section of the identity axis indicates the motion path passes through a symmetry state at t_b.

$$\Psi(t_b) = \Psi^*(t_b)$$

The anti-palidromic motion is represented graphically in the two subspaces in Figure 62. Figure 63 shows the anti-palindromic motion in the composite basis of $\mathcal{C}$.

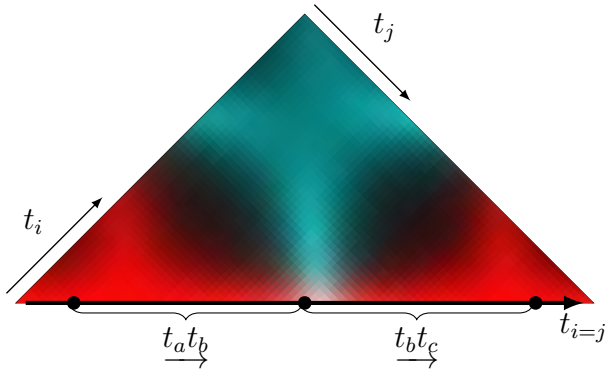

Figure 61: The triangular Z/Z^* shows anti-palindromic motion. The vertical cyan proximity signal, perpendicular to the identity axis, indicates reflected path repetition reversed in time. The white section of the identity axis indicates the motion path passes through a symmetric state before performing the reflected motion, reversed in time.

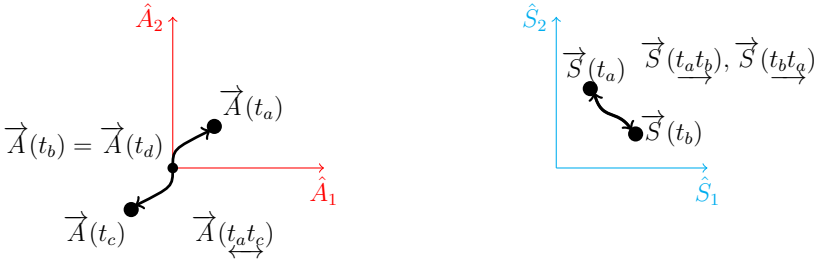

Figure 62: The anti-phase motion cycle graphed in the symmetric and anti-symmetric subspaces.

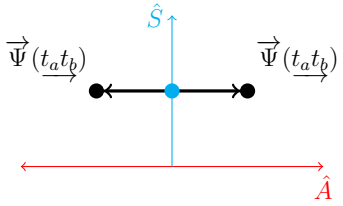

Figure 63: The anti-palindromic motion cycle graphed in the composite basis.

3.5 Short Motion Study

We have characterized the fundamental topological motifs of motion graphs as represented in the composite graph. Given a time series of motion capture data we can generate the associated Z/Z^* plot and extract the corresponding motion graph using this set of motifs. This is not only a way of extracting the associated motion graph but also a method of providing a scientific taxonomy for different types of motion, characterizing them by their symmetry properties in space and time.

Below are a series of longer movement sequences to which we apply this taxonomy and extract the corresponding motion graph. In terms of the physical model, the configuration states and motion paths which connect them are shown using stick figure representations of the kinematic chain. Motion paths are shown by a superposition of states with the grayscale color lightening as the path evolves in time.

In regard to the motion graph, we switch notation for the composite graph so that color is not required. Configuration states are notated using capital letters. Motion paths are notated using a pair of lowercase letters, indicating the start and end configuration states. The direction of the arrow in the graph determines the forward time direction. A double sided arrow is used for motion paths which are performed in either direction, namely reversible. The reversibility of a path may be justified when we measure a path's traversal in both directions, such as in palindromic movement.

Symmetric configuration states are notated using a bar over the letter and are drawn on the central vertical axis of the graph (symmetry axis). Symmetric motion paths are notated with a bar over the letter pair and are drawn along the central vertical axis when possible. The reflected versions of asymmetric states are labeled with an asterisk superscript and are located on the opposite side of the central vertical axis. Similarly, the reflected versions of asymmetric motion are labeled with an asterisk superscript and located on opposite sides of the central vertical axis.

We begin with six fairly simple example motions. They are: 1. Butterfly Stroke, 2. Jumping Jacks, 3. Jogging, 4. Walking, 5. Limping, and 6. Side Kicks. In the following figures the Z/Z^* plots are not rotated and the composite motion graphs are drawn in black using the aforementioned notation. Configuration states are identified on the right side of the Z/Z^* plots.

3.5.1 Butterfly Stroke

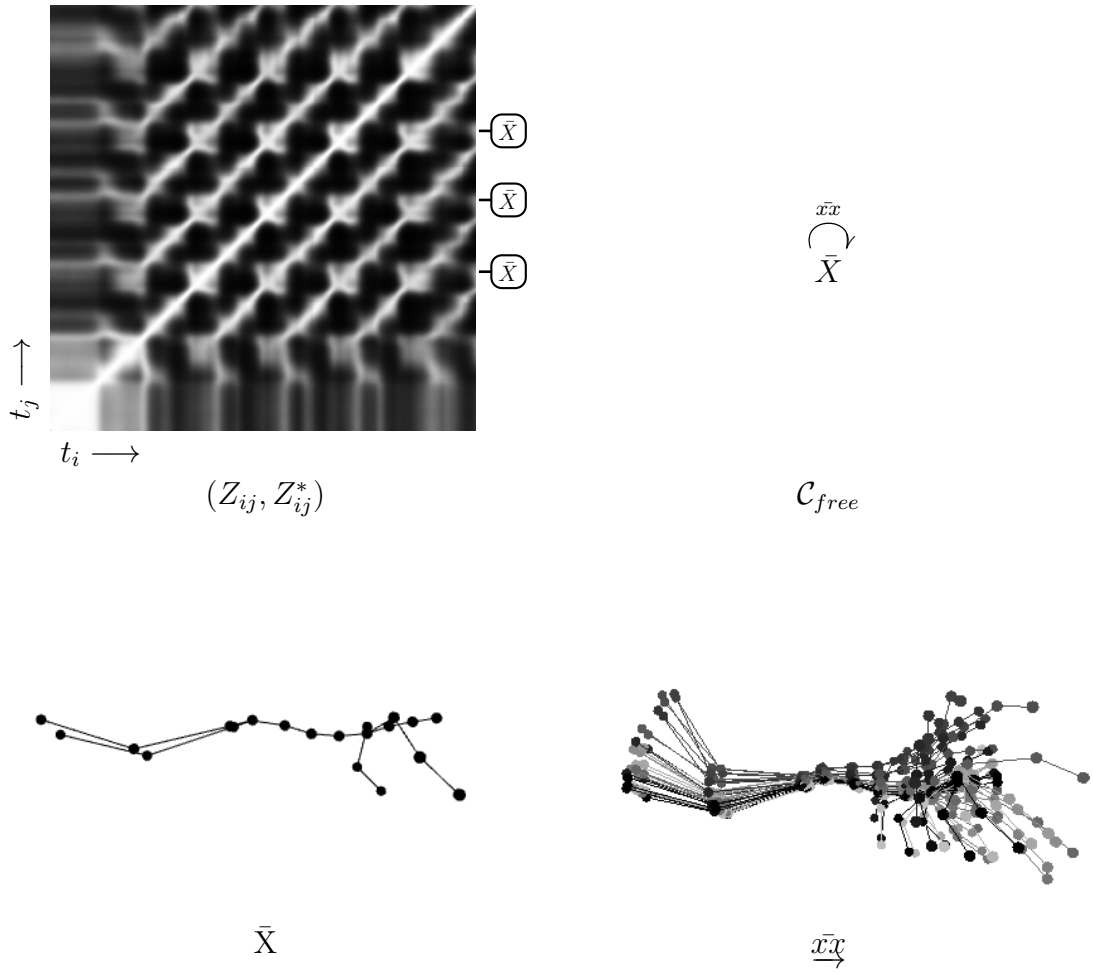

Figure 64: Butterfly Stroke (Symmetric, Cyclic)

The first phrase of motion is the butterfly stroke, shown in Figure 64. The motion is symmetric and cyclic. The symmetry is represented by the lack of color in the similarity plot. The cyclic aspect of the motion is represented by the off diagonal lines parallel to

the diagonal. The period of the motion corresponds to the distance between line in the x or y direction. The fact the lines are not connected indicates the paths are uni-directional. This means once a state has been passed through it is not returned to at any point in the cycle.

The corresponding directed graph consists of a state X with a unidirectional path xx, representing the cycle from state X back to state X. The symmetry of the state and path is represented by a bar. Any symmetric, uni-directional, cyclic motion will have a color similarity plot consisting of light grey, unconnected, parallel lines.

3.5.2 Jumping Jacks

The second phrase of motion consists of jumping jacks, as shown in 65. Jumping jacks are also symmetric and cyclic causing a grey similarity plot with the shape of the central axis repeated off center, parallel to the identity axis. The cross hatching pattern of the similarity plot, with proximity signals projecting perpendicularly away from the identity axis, represents a movement cycle which is palindromic, namely it is the same forwards and backwards.

The palindromic motion path is represented in the graph by a two way arrow connecting two states. The part of the Z/Z^* plot where the central axis crosses the perpendicular crosshatchings corresponds to points in the phrase where the movement stops momentarily to switch direction. These reversal points occur at the top and bottom of a jumping jack. We notate these states on the graph with two points labeled X and Y. The two sided arrow represents the reversible motion path between them. It is labeled xy. Any symmetric, palindromic, cyclic motion will have a color similarity plot of light grey crosshatched grid.

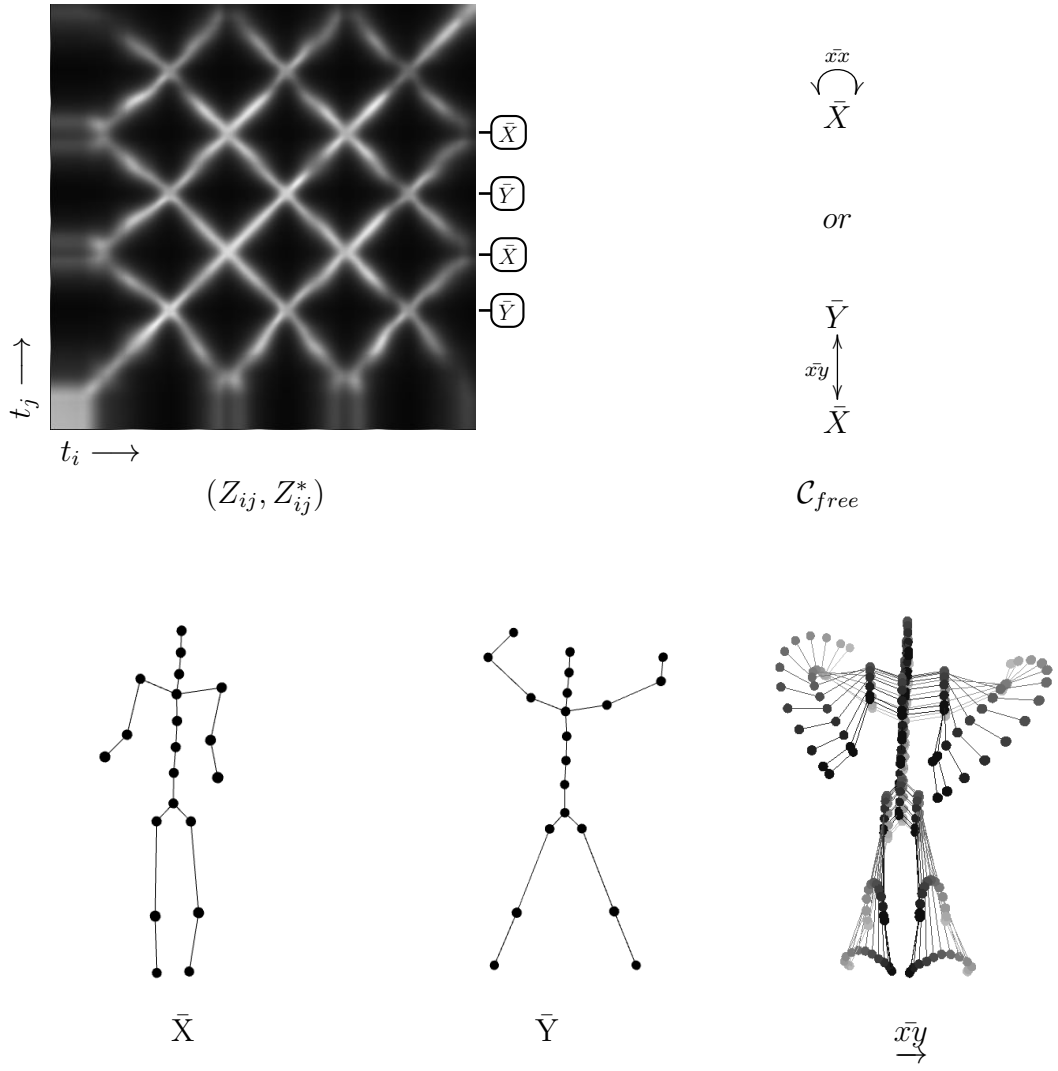

Figure 65: Jumping Jacks (Symmetric, Palindromic)

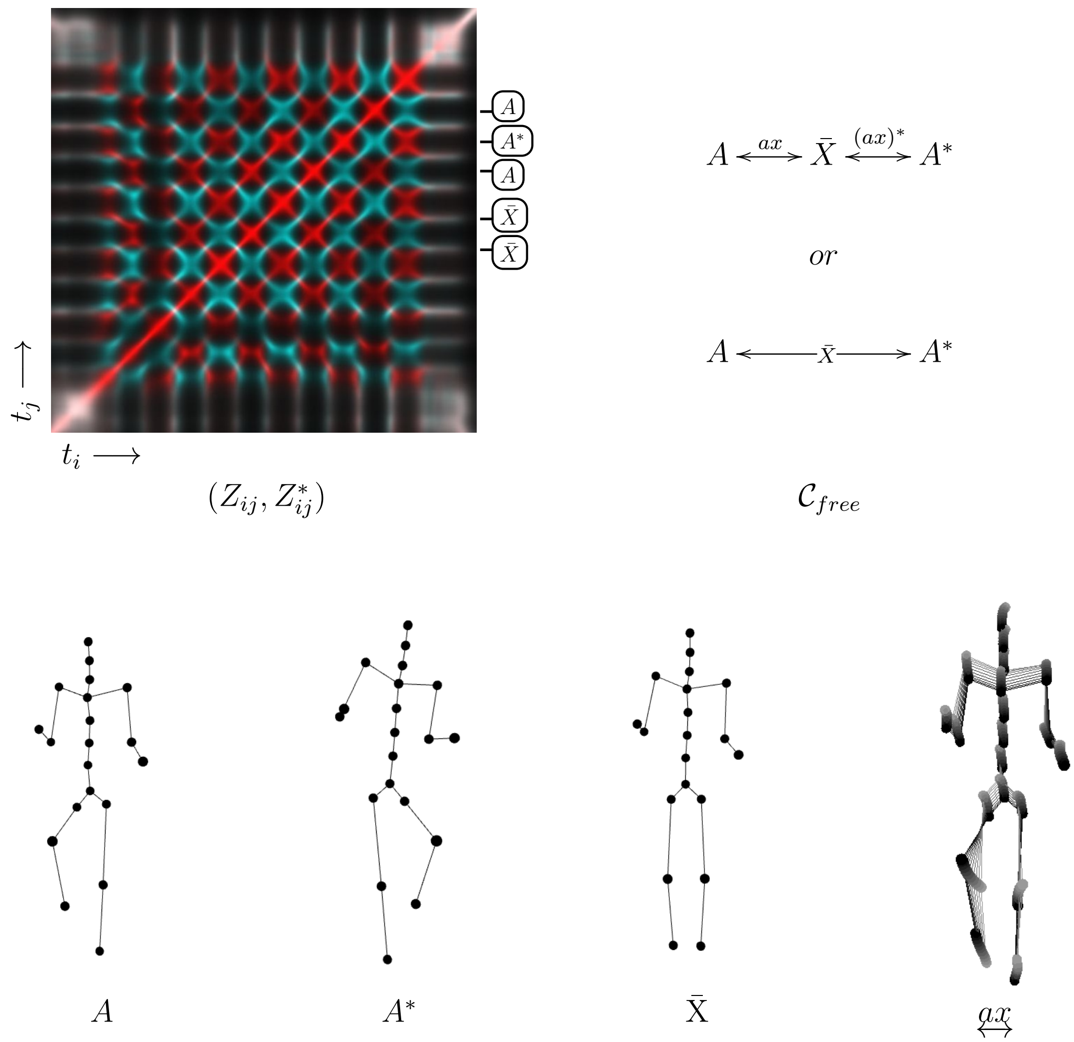

Figure 66: Jog in Place (Antipalindromic Cyclic)

3.5.3 Jogging in Place

The third motion phrase is of jogging in place, shown in Figure 66. The movement is cyclic anti-palindromic as it exhibits the features of that motif. It can be seen as two palindromic crosshatch patterns, one in red for Z and one in cyan for Z^*, which are 180 degrees out of phase with each other.

The anti-palindromic motion passes through the same symmetric state every half cycle shown by the white patch where the two grids of Z and Z^* cross. In the graph this state is notated by a central point label with a bar over X. On the graph, the configuration states at time of reversal are represented by two points, labeled A and A^*, on opposite sides of the symmetric state X. Two double sided arrows, labeled ax and $(ax)^*$ represent the motion paths joining these states. Note that the whole motion cycle consists of the same motion permuted through temporal and spatial reflection operations.

3.5.4 Walking

The forth phrase is walking, shown in Figure 67. Walking is cyclic antiphase motion as we can identify that motif in the Z/Z^* plot. It can be seen as the two parallel stripe patterns, one in red for Z and one in cyan for Z^*, which are 180 degrees out of phase with each other. The motion path never passes through a symmetric state as indicated by the fact that the red and cyan stripes never intersect to generate a white proximity signal in the Z/Z^* plot.

The corresponding graph shows two points, on opposite sides of the central axis, labeled A and A^*. The paths connecting them are unidirectional and labeled aa^* and $(aa^*)^*$ to indicate they are mirror images of one another. The total motion cycle consists of one motion path and its version reflected in space.

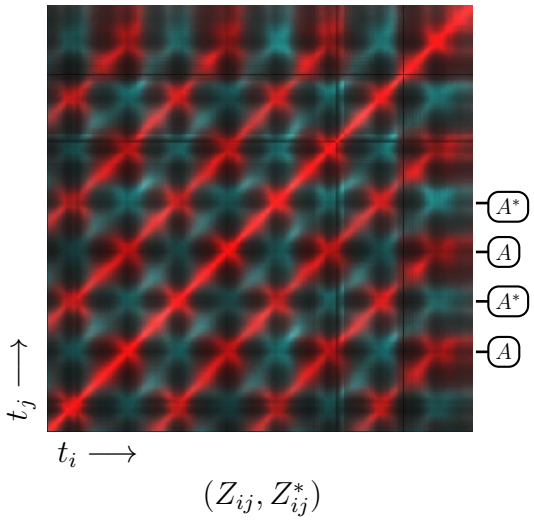

(Z_{ij}, Z^*_{ij})

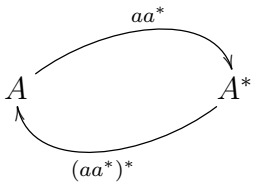

or

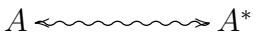

$\mathcal{C}_{free}$

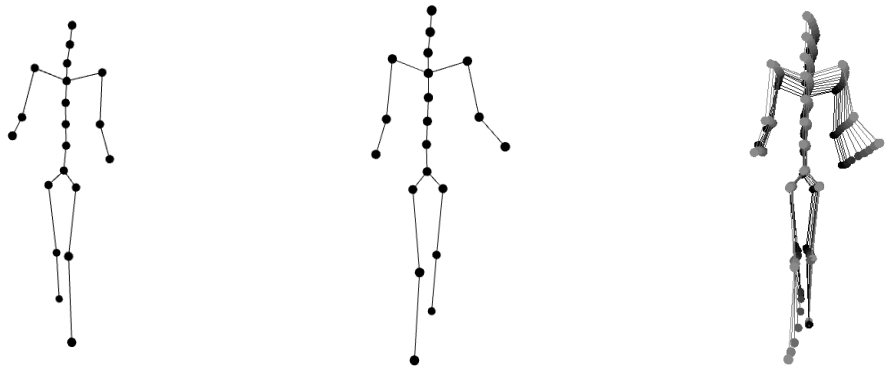

A A^* $\underrightarrow{aa^*}$

Figure 67: Walking (Anti-phase Cyclic)

3.5.5 Limping

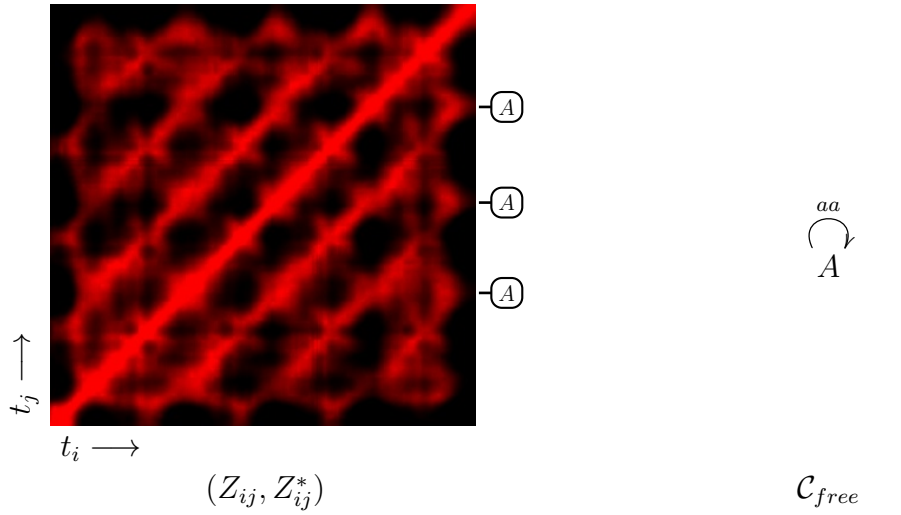

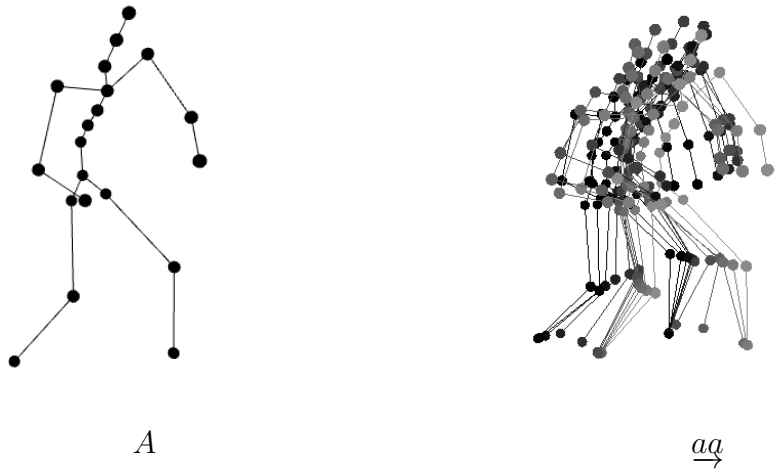

Figure 68: Limping (Asymmetric, Cyclic)

The fifth phrase is limping, shown in Figure 68. It is asymmetric and cyclic as we can identify that motif in the Z/Z^* plot. Limping breaks the left right anti-phase symmetry of walking though it is still cyclic so we only see a red striped pattern in Z but no signal coming from Z^*. Limping exhibits no spatial or time symmetry.

We show it on the graph by choosing a state to represent with a point labeled A. A unidirectional arrow loops from A back to A. This path is labeled aa. Though we could infer a

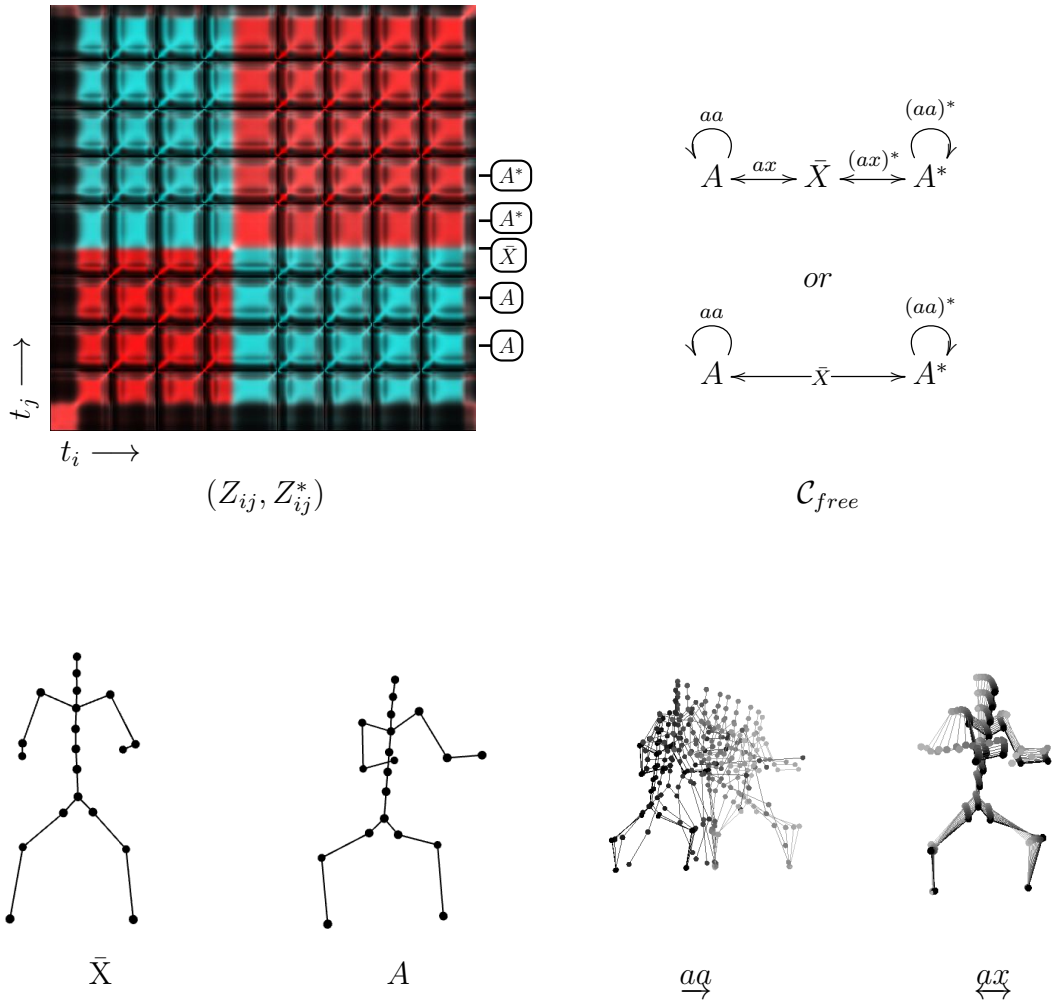

Figure 69: Side Kicks

mirror image of this movement it is not included in the graph.

3.5.6 Side Kicks

The sixth movement time series is a set of side kicks to the left, a switch of facing, and then a set of side kicks to the right. This is shown in Figure 69. The movement sequence is slightly more complicated than the previous examples as it manifests three motion motifs. These are asymmetric path repetition, reflected path repetition and anti-palindromic motion. These three motifs are indicated in the Z/Z^* plot by the region of red stripes, the region of cyan stripes and the small area around the identity axis where those two regions cross and a white

proximity signal is visible.

The graph consists of two points on opposite sides of the central axis. They are labeled A and A^* as they are reflected versions of one another. Each node has a unidirectional looping arrow coming off it labeled aa and $(aa)^*$ respectively. This path represents the kicking action on the left and the right. Connecting these two subspaces is a bidirectional arrow passing through the symmetric state node labeled X. This connecting part of the graph represents the part of the motion sequence where the subject switches direction. Since the connecting phrase is anti-palindromic it may be condensed in representation to the turn from right to center ax and the time and space reflected $(ax)^*$.

3.6 Complex Motion Study

Now that we have looked at and characterized simple movement sequences through their composite plots, composite graphs and stick figure representations we will use this same mode of analysis to map two additional movement sequences which have greater topological complexity. From these movement sequences we will extract the lexical map which underlies them. In this way we work to extract the underlying technique or movement vocabulary from example motion and fit the constituent motions into an overall taxonomy of the different types of movement. The two choreographies investigated are one yoga sequence and one karate sequence.

3.6.1 Yoga (Sun Salutation)

The example yoga sequence shown is a traditional movement sequence known as sun salutation. It is shown in Figure 70. The sun salutation is a series of motions which are composed together to generate a cyclic choreography. This series of motions starts and ends in the same configuration state. Therefore it can be repeated sequentially. The example motion

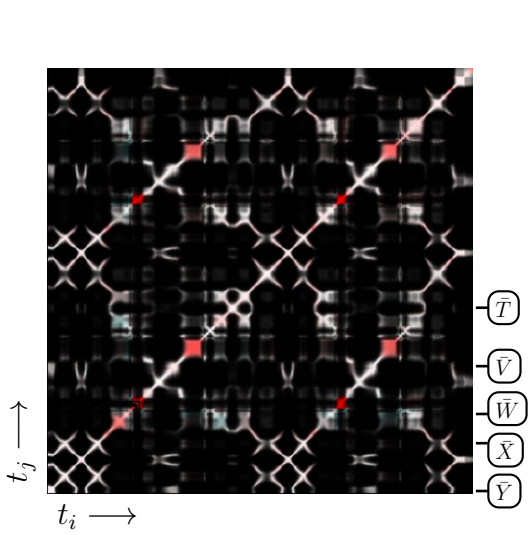

(Z_{ij}, Z^*_{ij})

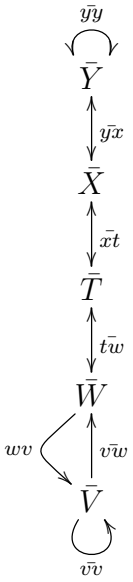

$\mathcal{C}_{free}$

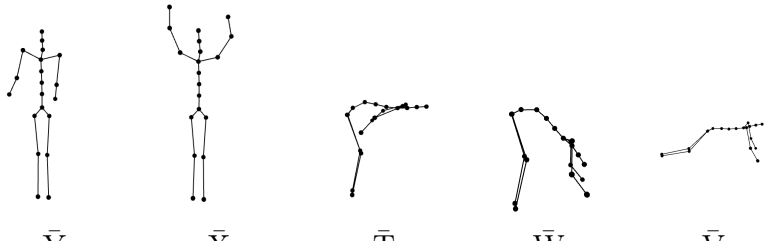

$\bar{\text{Y}}$ $\bar{\text{X}}$ $\bar{\text{T}}$ $\bar{\text{W}}$ $\bar{\text{V}}$

$\underset{\longleftrightarrow}{x\bar{y}}$ $\underset{\longleftrightarrow}{y\bar{y}}$ $\underset{\longleftrightarrow}{x\bar{t}}$ $\underset{\longleftrightarrow}{t\bar{w}}$ $\underset{\longrightarrow}{wv}$ $\underset{\longrightarrow}{v\bar{v}}$ $\underset{\longrightarrow}{v\bar{w}}$

Figure 70: Sun Salutation

capture data has the movement sequence performed twice in a row. As the plot shows the motion series consists largely of smaller time reversible movement phrases. The composite graph shows the space and time symmetries of the component phrases and how they are joined together.

The whole of this version of sun salutation is symmetric apart from the motion path $\underrightarrow{w\bar{v}}$. We can immediately apprehend this through the lack of color in the Z/Z^* plot apart from small sections of red where symmetry is broken. The sun salutation begins in a symmetric configuration state with the subject standing, arms at the side. We call this state $\bar{Y}$. From here the arms travel up overhead to the state $\bar{X}$ along the path $\underrightarrow{y\bar{x}}$ and return, palendromically, along $\underrightarrow{x\bar{y}}$. From $\bar{Y}$ the arms swing forward in a small palindromic motion cycle along a path $\underleftrightarrow{y\bar{y}}$ to return to the state $\bar{Y}$. This subspace constitutes the upright standing portion of sun salutation.

After completing this section the subject takes the arms overhead again along $\underrightarrow{y\bar{x}}$ to $\bar{X}$ and breaking at the waist lowers the torso to the horizontal along the path $\underrightarrow{x\bar{t}}$. In our nomenclature, this "half way up" position with flat back is called $\bar{T}$. From here the subject, taking the path $\underrightarrow{t\bar{w}}$, continues to lower the spine to "hang over" in state $\bar{W}$. Taking the asymmetric path $\underrightarrow{w\bar{v}}$ out of $\bar{W}$, the subject kicks one leg back and then the other to pause in "plank position" which we call $\bar{V}$. Since the $\underrightarrow{w\bar{v}}$ path breaks symmetry, by kicking one leg back and then the other, the motion path lacks an overbar even though the beginning and ending state are both symmetric. This section of the identity axis in the Z/Z^* plot is visibly red.

Next the subject bends the arms to lower the body to the bottom of a pushup position (chataranga) and proceeds to arch the back (updog) and then return to plank position $\bar{V}$. This motion path $\underrightarrow{v\bar{v}}$ is not palindromic or reversible. This motion cycle is so much repeated in the practice of yoga it has its own name, "vinyasa." From here the subject jumps both feet back toward the hands $\underrightarrow{v\bar{w}}$ and continues to make its way back through the reversible paths

$\underset{\leftrightarrow}{w\bar{t}}$, $\underset{\leftrightarrow}{t\bar{x}}$ and $\underset{\leftrightarrow}{x\bar{y}}$ to end in the initial standing state $\bar{Y}$. The whole sun salutation sequence is repeated again.

This completes the the topological analysis of sun salutation and constructs the underlying motion graph from which it comes. We can also make notes on the rapidity with which these movement phrases are performed by looking at the shape of the identity axis. As each pose is performed the subject takes a moment to dwell in that state in stillness. This is characterized by square regions along the identity axis. In addition it can be seen that the movement is performed with smooth changes in rapidity indicated by the smooth change in the width of the identity axis.

3.6.2 Graph Racemization and Notating Multiple Paths

Before performing this same type of analysis on the next larger movement sequence it is valuable to introduce two additional tools. First is the process of graph racemization. Second is a method for notating multiple non-similar paths between the same two end states.

In chemistry racemization is a process which converts a pure mixture, consisting of only one of the enantiomers of an asymmetric molecule, into a mixture which contains equal amounts of each enantiomer. For a motion graph the process consists of reflecting all the constituent motion paths in order to grow the motion graph. In a racemic motion graph the reflected version of any configuration state is part of the motion graph's set of configuration states. Visually, a racemic motion graph is symmetric around the vertical symmetry axis when represented in the composite basis.

Each motion sequence $\overrightarrow{\Psi}(t)$ can be reflected to $\overrightarrow{\Psi}^*(t)$. To represent this in the graph we simply reflect across the central symmetry axis. This corresponds to the application of the parity/reflection operator.

$$\mathbf{W}A = A^*$$

$$\mathbf{W}\underrightarrow{ab} = (\underrightarrow{ab})^*$$

Reflection operator generated motion paths are drawn with dotted lines.

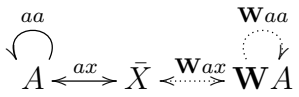

This means that we can use the reflected graph to expand the movement vocabulary. The graph is accessible from the initial graph if they overlap at some node. The expanded graph is in $\mathcal{C}_{free}$ and named $\mathcal{C}^{\dagger}_{free}$.

If there are multiple paths between two nodes we can give each a numerical subscript to distinguish them such as $\underrightarrow{ab}_1, \underrightarrow{ab}_2$. In terms of notation we can write this set as $\underrightarrow{ab}_i$. In other words a movement sequence, such as the martial arts form we are about to consider, may repeat the same motion between two states or include distinct motion which connects the same to states. We wish to use the same labeling for the repeated motion but have a unique identifier when that motion is distinct. Distinct motions which connect the same beginning and end configuration state can be distinguished by use of a subscript. In the graph a line which has an indexed label, such as ab_i, indicates a set of distinct motion paths which simply share the same starting and end points.

3.6.3 Karate (Bassai Dai Kata)

The final motion capture data series is from a Japanese martial arts sequence known as the Bassai Dai Kata. It is shown in Figure 70. A kata, literally the Japanese word for form, is a detailed choreographed pattern of movement. A kata is not performed in combat but rather as a training and memory device for a movement lexicon. It may be explained as a reference guide for filing a set of moves. After learning a given kata the constituent movements are remixed in the context of competitive sparring against an opponent. Stated mathematically we use this set of allowable paths as a map (graph) of $\mathcal{C}_{free}$. We then traverse the graph to

synthesize new movement sequences. Once the topology of the graph is generated it is now the task to figure out how to traverse it.

The structure of the Bassai Dai Kata is considerably more complex than the sun salutation. Unlike the sun salutation it consists mostly of asymmetric movement. The one symmetric state, notated as $\bar{X}$, is performed at the beginning, middle, and end of the kata. Four movement subspaces are articulated around the asymmetric poses notated A, B, C, D and their conjugates A*, B*, C*, and D*. The process of racimization expands the space of known movement from $\mathcal{C}_{free}$ to $\mathcal{C}^{\dagger}_{free}$. $\mathcal{C}^{\dagger}_{free}$ is a fully connected graph.

A qualitative kinetic analysis may also be performed by looking at the width of the diagonal signal. The diagonal signal in this movement series, as opposed to the sun salutation, is quite jagged. This indicates abrupt changes in momentum over time, meaning large net forces are at play. Strikes may be easily identified by the thinning of the identity signal. At the impact event of the impulse strike the motion path reversed direction. The associated visual artifact is the thinning of the identity signal to a place where an inversion spike is seen perpendicular to the diagonal.

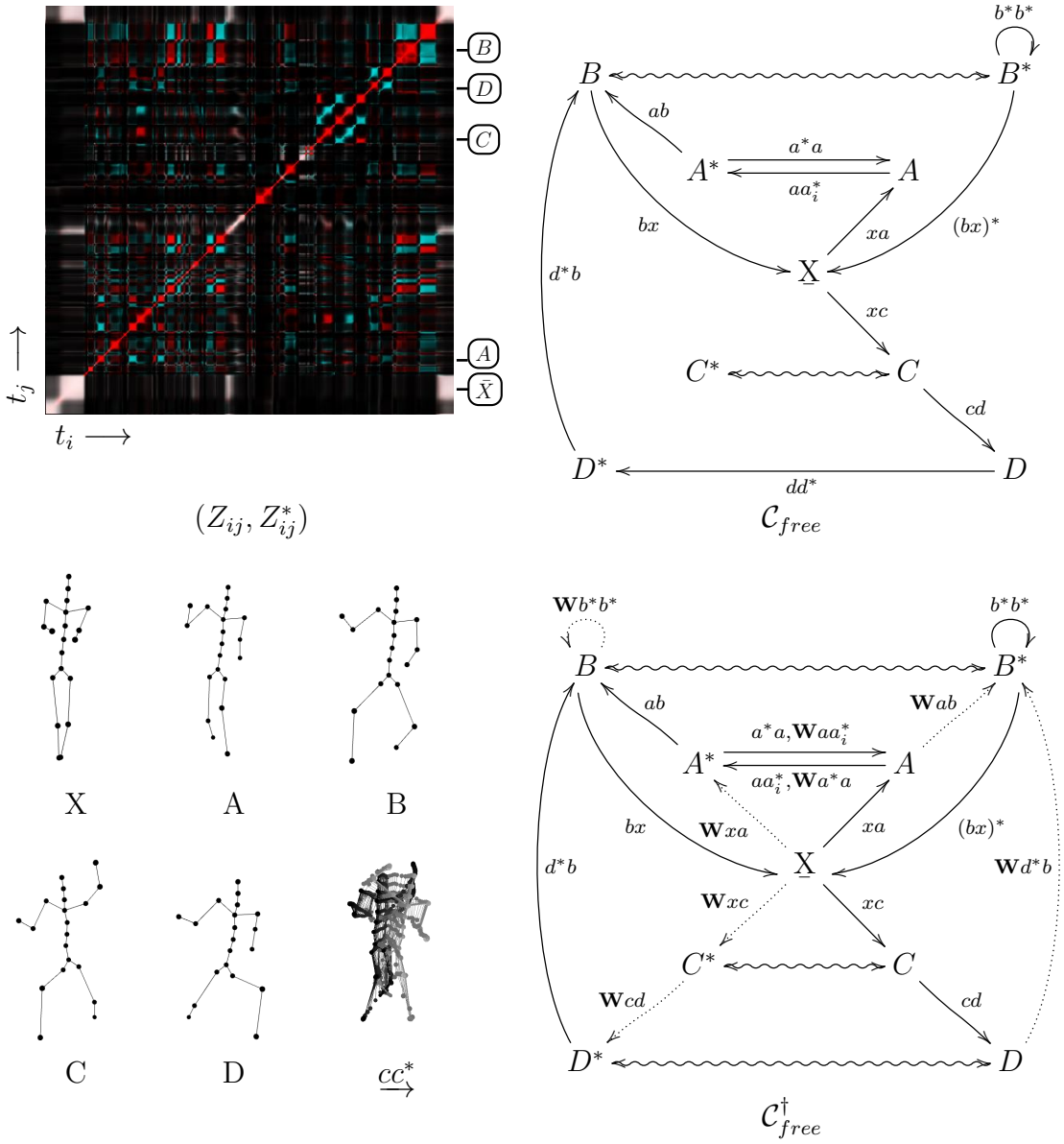

Figure 71: Bassai Dai Kata(Subject 135)

4 Video Motion Graphs

The cost and space required for a marker based motion capture system such as Vicon is prohibitive for many applications. On the other hand, single camera video acquisition is inexpensive and ubiquitous. While motion capture generates a moving skeletal model, sometimes image data is all that is required to model the subject. We will approach the problem of the last chapter but using color video data instead of motion capture.

- Develop a means to extract an image of the subject's body apart from the rest of the image data I. We call this the body image $\tilde{I}$. This requires segmentation and other video processing.
- Generate a technique using similarity metrics Z and Z^* to measure the similarity between two body image states $\tilde{I}_1$ and $\tilde{I}_2$.
- Use the measures Z and Z^* to generate metric spaces for body-image time series, $\tilde{I}$. We call this the Z/Z^* plot.
- Use the above analysis to generate a racemic motion graph for the time series data.
- Generate a Markov controller dependent on workspace and path features to traverse the motion graph.

4.1 Camera Model and Assumptions

We make the following assumptions to connect the math developed in the last chapter to this chapter. The camera image is modeled as simple orthographic projection oriented perpendicular to the gravity axis. Therefore the mapping from the coordinates of the subject's state to the image state is affine.

This mapping takes $\overrightarrow{\Psi}, \phi_z, \overrightarrow{r}$ on to I. We process the image I down to the body image $\tilde{I}$,

$\overrightarrow{\Psi}$	configuration state
ϕ_z	root coordinate rotation around vertical axis
$\overrightarrow{r}$	root position on horizontal plane
I	video image frame
$\tilde{I}$	body image frame

Table 1: Image processing quantities

making it invariant to position. and reducing the mapping to taking $\overrightarrow{\Psi}, \phi_z$ on to $\tilde{I}$.

$$I(\overrightarrow{\Psi}, \phi_z, \overrightarrow{r}) \longrightarrow \tilde{I}(\overrightarrow{\Psi}, \phi_z)$$

Given consistent lighting, clothing, hair, etc we assume the state of the body image $\tilde{I}$ is completely defined by its internal state $\overrightarrow{\Psi}$ and its orientation around the gravity axis ϕ_z. We neglect circumstances such as occlusion of a limb and assume the mapping to be one to one.

We name the manifold formed by the body image state space P_{free}. C_{free} was independent of ϕ_z and C^*_{free} mapped through the reflection of Ψ to Ψ^*. P_{free} is dependent and maps through mapping Ψ to Ψ^* and ϕ_z to $-\phi_z$. P_{free} represents the manifold of accessible image states mapped from the manifold of accessible physical body states C_{free}. This mapping in group theory would be described as group semidirect product $G_{body} \times SO(2)$.

4.2 Image Processing

Video data consists of four channels, three color channels (red, green and blue or RGB) and one alpha channel. The video data for this portion of the work was recorded in February of 2008 by Sarah Lawrence dance students in the campus squash courts. Two sequences will

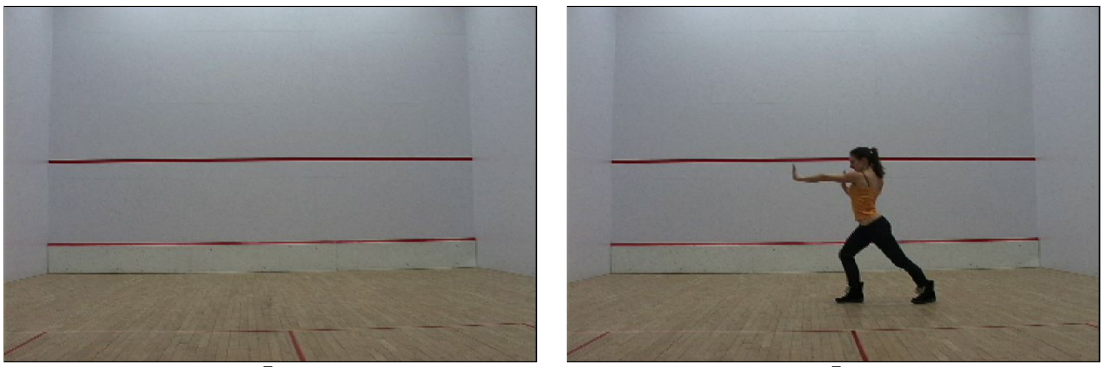

I_0 I

Figure 72: Background and Image

be looked at to show different video sequence features.

4.2.1 Background Subtraction

The first data processing task is to separate the region of interest, namely the region of the image containing the image of the body. Background subtraction is employed to separate the image of the subject from the physical setting. In this technique the image with the subject in it I is compared to the image without the subject, namely the background image I_0. These are shown in Figure 72.

The background subtraction measures the absolute difference between pixel values. The subtraction $|I_0 - I|$ takes place over the color vector for each pixel so the $|I_0 - I|$ is also a color image. In order to sort pixels between subject and background we first flatten the image in color space and convert to a greyscale determined by the luminance. This is a magnitude of the color vector. Each are shown in Figure 73.

By thresholding the greyscale difference image we can produce a mask which is binary 0 or 1 values. 0 for black or background pixel, 1 for white or subject pixel. To clarify the image signal we process the image through the following binary operations. The post thresholding and binary operation masks are shown in Figure 74.

- Grow: If a pixel is next to a 1 pixel it turns to 1. This grows the mask from the edges

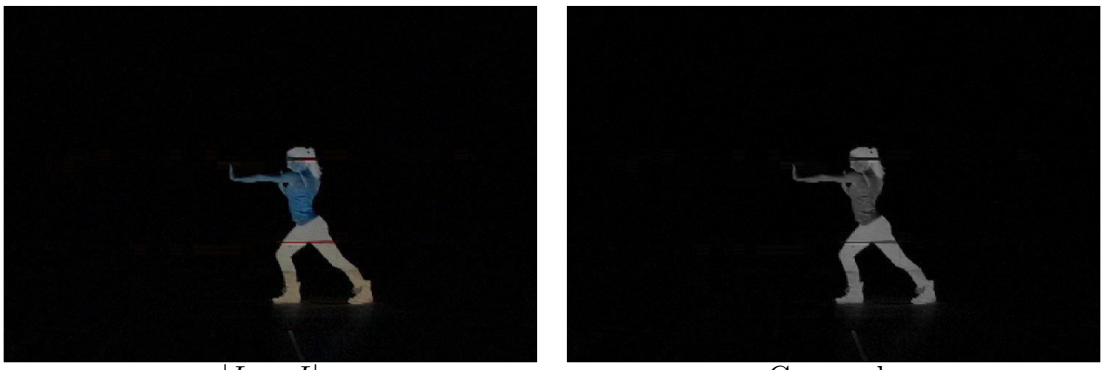

$|I_0 - I|$ Greyscale

Figure 73: Background Subtraction

Mask Annealed Mask

Figure 74: Mask Processing

and fills in holes.

- Shrink: If a pixel is next to a 0 pixel it turns to 0. This shrinks the mask from the edges and widens holes up.

By performing a series of grow operations followed by the same number of shrink operations we can get a much improved signal for the subject mask. We call this process annealing since it fills in holes below a certain size.

Taking the product of the annealed mask and the original video frame delivers only pixels which are imaging the body of the subject. This is our body-image signal $\tilde{I}$. The final filtered body image and it's mask are shown in Figure 75.

$$\tilde{I} = I * \rho$$

I_1 ρ_1

Figure 75: Filtered Body Image and Mask 1

I_2 ρ_2

Figure 76: Filtered Body Image and Mask 2

4.2.2 Body Image Similarity (Z Function)

Figure 76 and Figure 77 show two different body images along with their masks. The mask are shifted so that their centroid is in the middle of the image frame.

In order to generate a similarity function we take a normalized overlap integral of centered masks.

$$Z = \frac{\sum_{x,y} \rho_1(x,y)\rho_2(x,y)}{\sqrt{(\sum_{x,y} \rho_1(x,y))(\sum_{x,y} \rho_2(x,y))}}$$

Notice if the distributions are identical then the similarity metric is unity. If $\rho_1(x,y) = \rho_2(x,y)$ then since $\rho_1(x,y)$ has binary values $\rho_1^2(x,y) = \rho_1(x,y)$.

I_3 ρ_3

Figure 77: Filtered Body Image and Mask 3

$\rho_1\rho_2$ $\rho_1\rho_2^*$

Figure 78: Similarity Measure: $Z_{1,2} = 130/255$ and $Z*_{1,2} = 127/255$.

$\rho_1\rho_3$ $\rho_1\rho_3^*$

Figure 79: Similarity Measure: $Z_{1,3} = 203/255$ and $Z*_{1,3} = 132/255$

In addition $\sqrt{(\sum_{x,y}\rho_1(x,y))(\sum_{x,y}\rho_1(x,y))} = \sum_{x,y}\rho_1(x,y)$. Using this we can show if the distributions are identical then the similarity metric is unity.

$$Z = \frac{\sum_{x,y}\rho_1(x,y)\rho_1(x,y)}{\sqrt{(\sum_{x,y}\rho_1(x,y))(\sum_{x,y}\rho_2(x,y))}} = \frac{\sum_{x,y}\rho_1(x,y)}{\sum_{x,y}\rho_1(x,y)} = 1$$

As with Z we can define an anti-similarity measure Z^* as the overlap integral between the two distributions while one is reflected around the vertical axis passing through its center. Since $\rho_(x,y)$ is centered at zero the x centroid does not change in the reflection operation and can be represented by flipping the sign of x in the mask $\rho^*(x,y) = \rho(-x,y)$. Here we define the anti-similarity function.

$$Z^* = \frac{\sum_{x,y}\rho_1(x,y)\rho_2(-x,y)}{\sqrt{(\sum_{x,y}\rho_1(x,y))(\sum_{x,y}\rho_2(x,y))}}$$

The mask distribution products used for Z and Z^* are shown in Figure 78 and Figure 79. The normalized integral of these distributions give us Z and Z^* respectively.

4.3 Z_{ij} and Z^*_{ij} Plots

When we measure the Z and Z^* between all of the states of a motion time series it generates a motion spectrum or similarity plot. As we did in the motion capture data, we will develop similarity and anti-similarity plots as the metric spaces over body-image time series. We can combine the Z_{ij} and Z^*_{ij} plots into a single color plot to analyze topologies, symmetry properties and momentum properties of the motion sequences.

We can then characterize these motion spectra.

- If a diagonal element is large this indicates stillness.
- If a diagonal element is white it indicates symmetry in the body image and if it is red it indicates an asymmetry in the body image.
- Off-diagonal signal areas indicate repetition. The color indicates the symmetry of the repetition. Red is repeating an asymmetrical movement. White is repeating a symmetric movement and cyan is repeating the reflection of an asymmetric movement.

In the last chapter Z/Z^* plots are used to construct the motion graphs. Figures 80 and 81 show this process for motion sequences recorded of two subjects.

4.4 Motion Planning

Once the motion graph is constructed for each motion sequence it serves as a set of rules for playing back the original body image sequence. We can generate a dynamic controller for traversing the graph using a Markov-like network.

There are multiple distinct paths between node states; therefore this is not a typical directed graph formulation. To do a proper analysis we need to form an adjacency matrix representing connectivity between paths. The map G can be used with a Markov-like network. A random walk on G is a Markov chain defined on G with the transition probability matrix $P = P_{ij}$

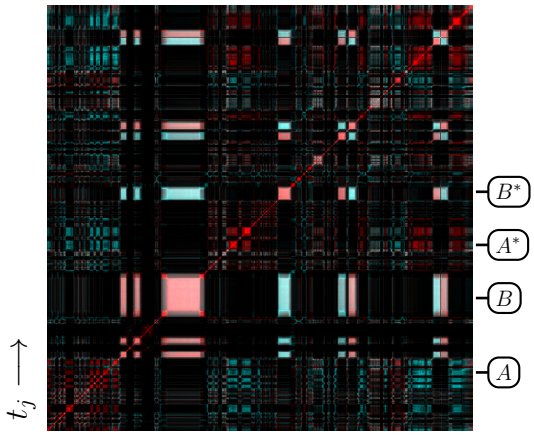

(Z_{ij}, Z^*_{ij})

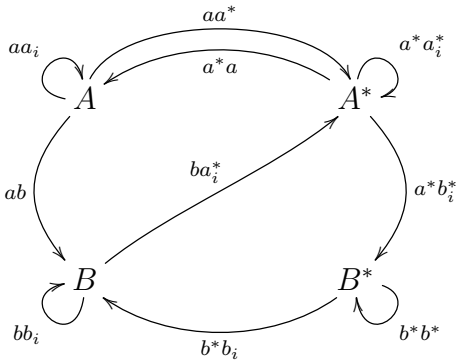

$\mathcal{C}_{free}$

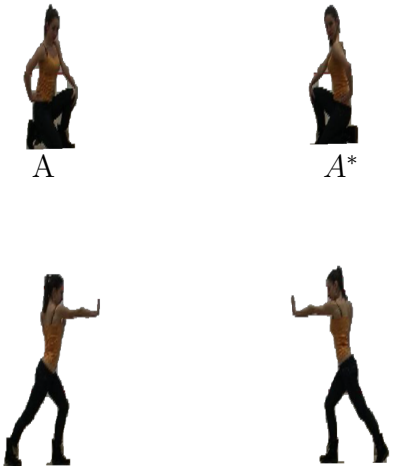

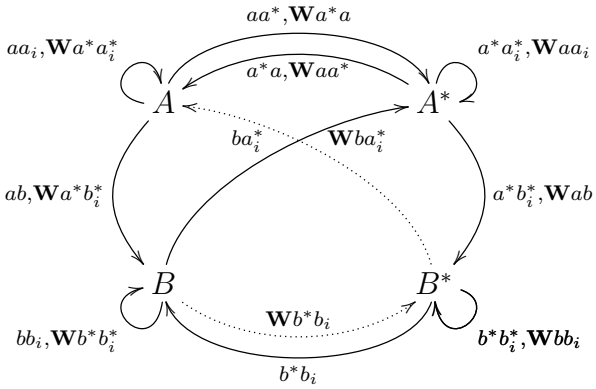

$\mathcal{C}^{\dagger}_{free}$

Figure 80: Image Configuration Space Subject 1

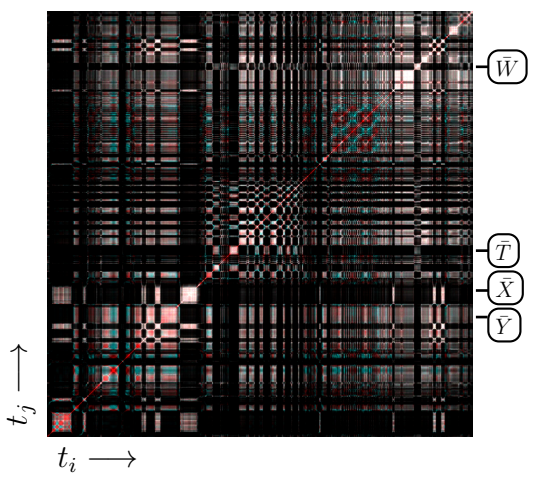

(Z_{ij}, Z^*_{ij})

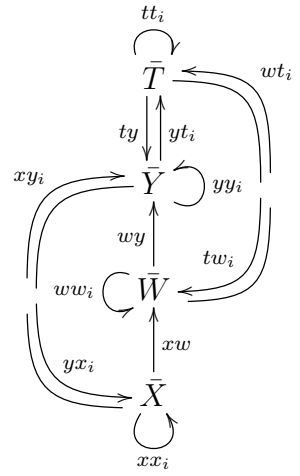

$\mathcal{C}_{free}$

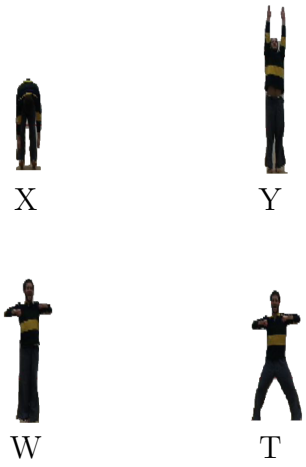

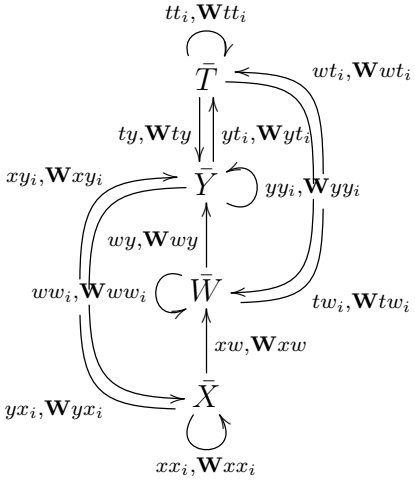

$\mathcal{C}^{\dagger}_{free}$

Figure 81: Image Configuration Space: Subject 2

between path α_i and path α_j.

Each path α_i has a beginning state and an end state. Paths are connected only if the end state for path i is the beginning state for path j. For example if $\alpha_1 = \underrightarrow{xx}$ and $\alpha_2 = \underrightarrow{xy}$ then P_{11} and P_{12} could both be non-zero because path 1 ends in x and so could be followed by path 1 or 2, but because path 2 ends in y it cannot be followed by path 1 or 2, so P_{22} and P_{21} would both be zero.

The motion path $\alpha_i = (\underrightarrow{nm})_i$ begins in state n and ends in state m. We define a function like the kronecker delta to represent the adjacency matrix for paths.

$$\delta_{m_i n_j} = \left\{ \begin{array}{ll} 0 & \text{for } \mathrm{m_i} \neq \mathrm{n_j} \\ 1 & \text{for } \mathrm{m_i} = \mathrm{n_j} \end{array} \right\}$$

Here n and m are indices on states such that n_j is the index of the beginning state of path j and m_i is the index on the end state of path i.

Using the path adjacency matrix the transition matrix can be defined as follows, where $E(j)$ represents the Markov weights.

$$P_{ij} = E(j)\delta_{m_i n_j}$$

We can control the behavior of subject in workspace by applying a random walk under dynamic Markov weights that are functions of workspace features and path features.

4.4.1 Implementation

Consider the following Markov weight function.

$$E(j) = e^{-\beta[\overrightarrow{f}(\alpha_j) - \overrightarrow{f}(t)]^2}$$

An implementation was developed using distance from a target as a workspace feature and

displacement as the path feature.

$$\overrightarrow{f}(\alpha_j) = \Delta \overrightarrow{x}_j$$

$$\overrightarrow{f}(t) = \overrightarrow{x}_{target} - \overrightarrow{x}(t)$$

At the end of each path the next path is chosen using values from the transition matrix as probability values. In this way the subject is simulated stochastically. This generated a responsive virtual character which was able to move through a space and choose motion paths which led it toward the goal marker. Still shots are shown in Figure 82. A trail of $\overrightarrow{x}(t)$ target position $\overrightarrow{x}_{target}$ is shown in blue.

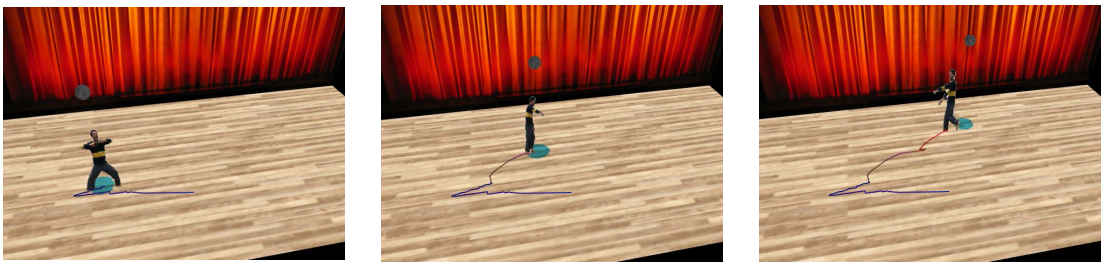

Figure 82: Frames from Markov controlled avatar

5 Particle Representation

In Chapter 2 we developed a method for mathematically representing articulation of the human skeleton. We used a kinematic chain model with state variables measured by motion capture technology and generated a metric for measuring the difference between kinematic states. Chapter 3 used the space of this metric over a kinematic time series to extract the corresponding motion graphs.

Chapter 4 applied a similar approach for extracting motion graphs for processed video sequences. With the processed body-image as our reduced representation we generated a metric for comparing body-image states. We then used the corresponding metric space to construct the motion graph for a body-image time series.

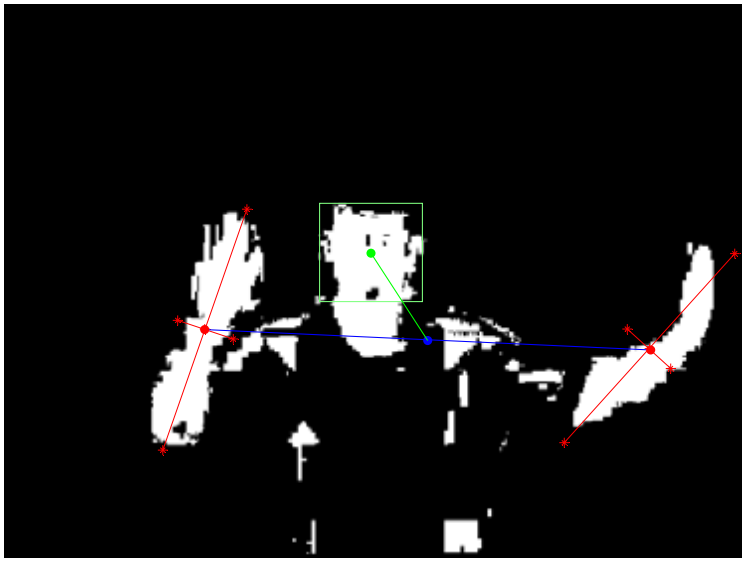

Figure 83: A multi-particle model of frontal arm gesture.

The present chapter develops a mathematical model and corresponding metric for processing front facing arm gestures. This situation is common in physical communication settings such as broadcast news, academic lecture, home gaming or traffic control. In a type of hybrid approach we use computer vision techniques on video data to construct a non-anatomical kinematic chain model and an effective distance metric for comparing states. A "multi-particle

model" of the body image, with state variables measured by computer vision techniques, is used to represent the articulation of the arms relative to the face. This application is shown in Figure 83.

5.1 Techniques

There are several intermediate pattern recognition and image processing tasks (see Figure 84) which must be accomplished to construct the multi-particle representation suited for a recognition scheme. These tasks are listed below.

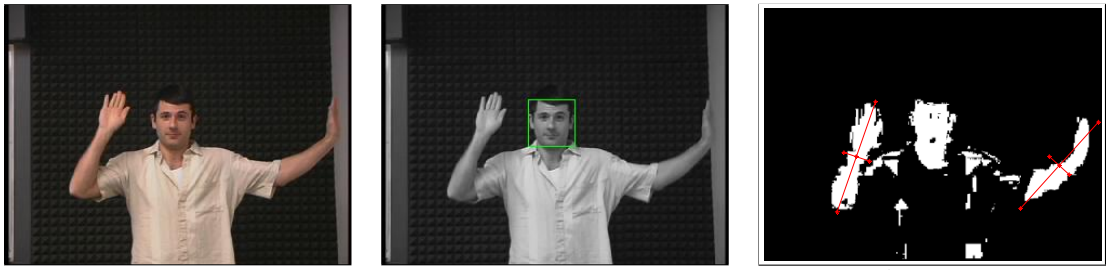

Image Face Detection Particle Extraction

Figure 84: Image processing for constructing a multi-particle representation.

- Face Detection: This process is able to identify images of faces in the visual field. The location of the face generates an origin of coordinates for the body representation.
- Color Segmentation: This process, like background subtraction, is able to segment the image into various regions of interest. We use a statistical model to identify skin tone pixels. Different implementations are looked at. This process leaves us with regions of interest in the visual field which are identified as skin tone.
- Particle Representation: Moment analysis is applied to create a representation of the two arms position and orientation in space relative to the face. This reduced representation is used to generate a feature vector of unity magnitude which describes the state of the simplified kinematic model.

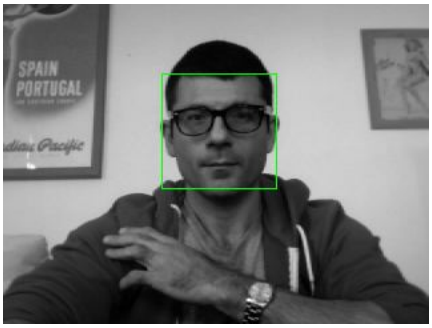

Figure 85: Face Recognition Using Haar-like Features

- Similarity Metric Z: We define a metric space to compare various states of the subject and enable the construction of metric spaces over motion time series.

5.2 Face Recognition

The facial recognition technology implemented in this work uses OpenCV. [30] This is an opensource code base for programming computer vision applications. The face tracking code provided by OpenCV extracts image features from greyscale image integration over a set of basis functions. The feature set is described as "Haar-like" since the basis functions resemble the square functions that are Haar wavelets. These kinds of Haar-like features can be used to recognize any number of image patterns.

The face detector of OpenCV has been initially proposed by Paul Viola and improved by Rainer Lienhart. The algorithm uses a cascade of boosted classifiers working with Haar-like features as presented by Menezes et al. [37] In this case it is front gazing faces, though side gazing implementations have been performed by groups such as Wu et al. [59].

OpenCV can consistently detect faces from a live camera feed in real-time. After implementing this method it is possible to identify the location of a face in an image. We use the face as the center of coordinates for looking at the configuration of the arms.

5.3 Color Segmentation

Color analysis employs statistical methods to extract information about an image scene based on color. This type of analysis works best on scenes with objects of relatively uniform color placed in front of a uniform background. New video technology providing turn-key depth channel video can be used in conjunction with color analysis to easily separate the subject image from the background.

5.3.1 Colorspace

Perceivable differences in color span a 3-D space due to the 3 types of color photoreceptors in the eye. [31] Typical video camera CCDs measure images on 3 channels: red, green and blue. The RGB color space (gamut) is cubic. Any color in the RGB gamut can be represented as a point in a cube. The color spectra in Figure 86 show pixel color locations in the RGB cube as seen looking down the (1,1,1) axis.

The RGB color space can be transformed via a non-linear mapping. The HSV (hue, saturation, value) and HSL (hue, saturation, luminosity) spaces represent color in a polar coordinate system. [23] In RGB space the points along the central (1,1,1) axis vary from black to white. The HSV and HSL spaces represent color relative to this central axis. The H value determines the angular position, the S value determines the distance from the axis while the V or L values determine the projected distance along the main axis.

5.3.2 Color Tone Distributions

Consider an object in the image of semi-uniform color and all of the pixels associated with it. The RGB values provide a sample colorspace distribution of that object in the image. Not all of the pixels associated with this object have exactly the same value RGB values. Instead the object has a color tone, or localized distribution in colorspace.

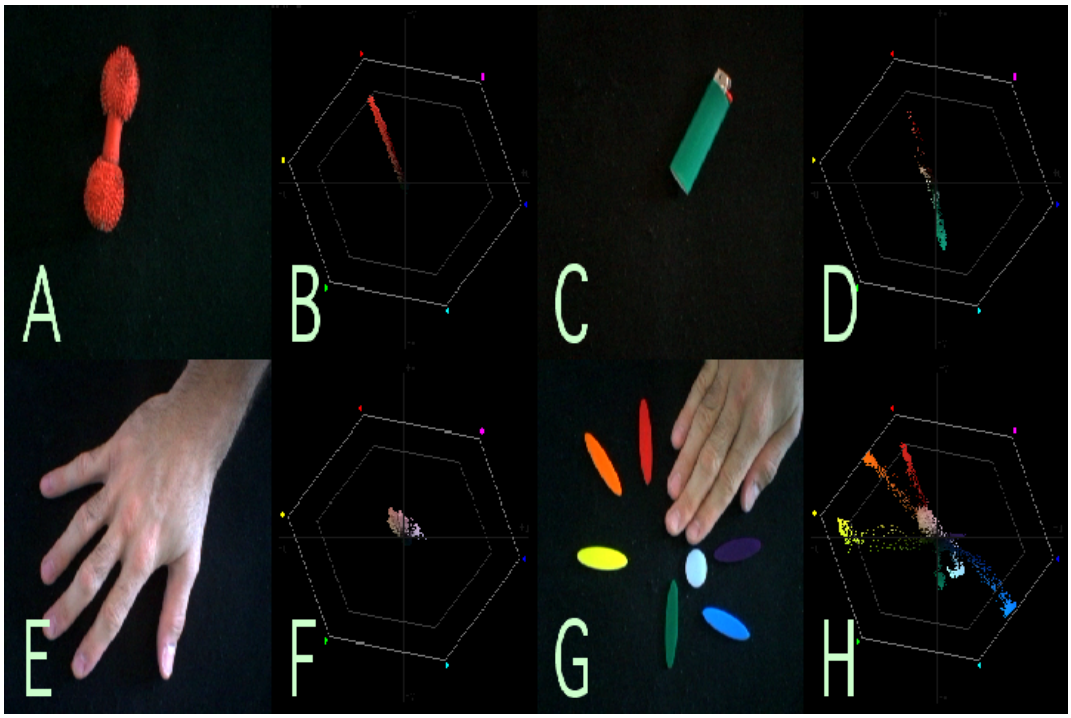

Figure 86: Color Tone Distributions

There are various ways to use pattern classification models to identify objects in images according to color. The task is to segment colorspace into various regions, each identified with being one of the target color tones or some outlier category. Figure 86 shows various color tone distributions including that of skin.

5.3.3 Bayesian Theory

Consider an object of semi-uniform color in the image. The pixels of this object do not all have the same exact color. The object pixels' color values $\overrightarrow{c}$ form a distribution in colorspace. Bayesian estimation uses an analysis of these type of feature distributions (the feature here being color) for the purpose of statistical recognition.

Firstly, a note on conditional probability notation. The probability of x is written $P(x)$. The probability of x and y is written $P(x, y)$. Clearly the ordering of terms x and y is not in this case. The probability of x given y is written $P(x|y)$. This is also known as the conditional

probability of x given y. Here the ordering of terms is important.

The fundamental proposition of Bayesian probability theory is that the probability of x and y occurring is the probability of x given y, times the probability of y. Due to symmetry between x and y in $P(x, y)$ the probability of x given y, times the probability of y, is equal to the probability of y given x, times the probability of x.

Below f and c are used to make reference to the particular situation of measuring the image color c, of an object f. In this case c serves as the measurement where f determines the color tone distribution.

$$P(f, c) = P(f|c)P(c) = P(c|f)P(f)$$

Since we are interested in identifying the pixels that are associated with a given color tone we look for an expression of $P(f|c)$. Using the equivalence between the last two terms yields the following equation. This is Bayes's theorem. [19]

$$P(f|c) = \frac{P(c|f)P(f)}{P(c)}$$

Terms of Bayes's theorem have special names that are typically used for them. The conditional probability of f given c, $P(f|c)$, is known as the posterior probability. $P(f)$ and $P(c)$ are known as the prior probabilities of f and c respectively. These are also known as marginal probabilities.

For a set of different color tones the prior probability of c can be calculated by the weighted sum of $P(c|f)$. This process integration over all possible f is known as marginalization. [19] It yields the following equation.

$$P(f_i|c) = \frac{P(c|f_i)P(f_i)}{\Sigma_j P(c|f_j)P(f_j)}$$

Assuming the priors of each f are all equal, $P(f_i) = P(f_j)$, then Bayes's theorem simplifies

to the following.

$$P(f_i|c) = \frac{P(c|f_i)}{\Sigma_j P(c|f_j)}$$

5.3.4 Gaussian Classifiers

In order to calculate $P(f_i|c)$ for a given color measurement we first need to create a set of classifier functions to give $P(c|f_j)$. These classifier functions are distributions in color space that give the probability amplitude for measuring a color when the image shows f_j. A sample of the color distribution of a given f_j must be taken in order to construct the appropriate function. A reasonable function for this purpose is the gaussian, or normal, distribution. The zero, first and second order statistics can be measured to get the center and covariance of the distribution. This is sufficient to construct the appropriate normal distribution. The resulting gaussian distribution functions as a statistical model for $P(c|f_j)$.

$$P_{norm}(f_i|\overrightarrow{c}) = N \exp\left(-\frac{1}{2}(\overrightarrow{c} - \overrightarrow{c}_i)^\top cov_i^{-1}(\overrightarrow{c} - \overrightarrow{c}_i)\right)$$

This color measurement c may be represented in any colorspace (HSV or HSL) or subspace (HS). When implementing this approach the HS subspace is often decomposed into a non-periodic coordinate representation using $s\cos 2\pi h$ and $s\sin 2\pi h$. Since hue has a discontinuity at 1-0, even though these are the same value, the cartesian mapping of the hue subspace is necessary to build a proper gaussian model.

Once each f_j is sampled and the normal distribution for that $P(c|f_j)$ is constructed then $\Sigma_j P(c|f_j)$ can be calculated. This serves to normalize the set of $P(c|f_j)$ functions to finally yield the posterior probability function $P(f_i|c)$. Typically a broad outlier distribution is included in the normalization term to pick out colors that are not associated with any f_j.

5.3.5 Histogram Methods

Rather than using the sample distribution to calculate a centroid and a covariance matrix for a gaussian model a histogram model may be built. The sample pixels are used to fill bins in colorspace. When properly normalized the filled bins form a histogram that can be used as a probability density function $P(c|f_i)$. The backprojection of the image through the histogram calculates $P(c|f_i)$ by giving the histogram magnitude for a certain color value. Since color sample points become sparse at higher dimensions an H or HS subspace is often used for back projection. This is the type of color signal used in camshift algorithm. Since no function is being explicitly built the histogram can easily represent a periodic space such as hue.

5.3.6 Color Segmentation

Consider a situation where a camera feeds video of different kinds of objects, f_i. Each pixel in the image has a color c. The task is to use statistics to assign an identity to each pixel in the image to one of the kinds of fabric. The probability a certain pixels' color corresponds to object f_i is $P(f_i|c)$.

The set of N $P(f_i|c)$ measurements produces N greyscale images. This density function can be used as a masslike quantity in the analysis. A thresholding operation is often performed on these greyscale distributions to create image segments that have well defined borders. Once this thresholding is performed each f_i channel can be subjected to blob/moment analysis described above. The product of such a segmentation is shown in Figure 87.

5.3.7 Post Processing

An image of a frontal human gesture includes multiple skin tone regions. After filtering this image of skin pixel regions we segregate the multiple regions by identifying the various

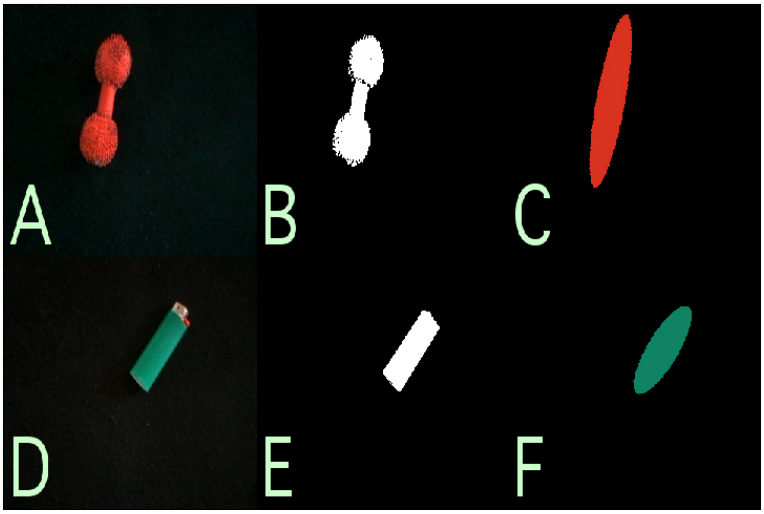

Figure 87: Color Sementation and Ellipse Fitting

connected components of the binary image. Those not belonging to the face are assumed to be the arms. The two arm regions are the objects of analysis for the next section.

5.4 Single Particle Representation

Given a previously segmented region of the image plane we analyze it as a 2D probability density function such as that shown in Figure 88.

5.4.1 Cartesian Moments

In the 2D (x,y) image plane the position is notated by the vector $\overrightarrow{r}$.

$$\overrightarrow{r} = \begin{pmatrix} x \\ y \end{pmatrix}$$

The image moments are defined as follows. The order of a given moment is $p + q$.

$$M_{pq} = \sum_x \sum_y x^p y^q \rho(\overrightarrow{r})$$

The zero moment M_{00} represents the total mass of the distribution. For a 2D binary distribution the zero moment measures the area.

The centroid is the vector set of first order moments. It is the center of mass, or average position of the distribution and is calculated as follows.

$$< \overrightarrow{r} >= \begin{pmatrix} \bar{x} \\ \bar{y} \end{pmatrix} = \frac{1}{M_{00}} \begin{pmatrix} M_{10} \\ M_{01} \end{pmatrix}$$

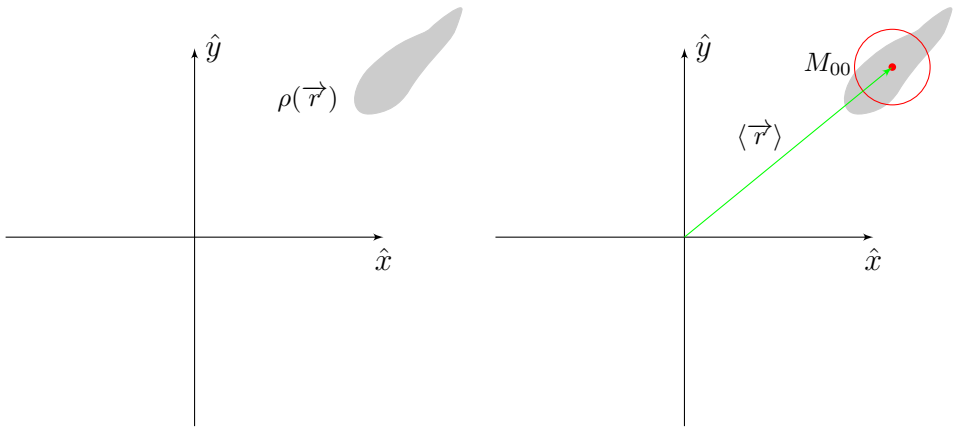

Figure 88: 2-D Distribution Mass and Centroid

The central moments measure distribution features around the center of mass. These features are invariant to translation. The central moments are defined as follows.

$$\mu_{pq} = \sum_{x} \sum_{y} (x)^p (y)^q \rho(\overrightarrow{r} - \langle \overrightarrow{r} \rangle)$$

The central moments can be calculated from the image moments using the formula below. [21]

$$\mu_{pq} = \sum_{m}^{p} \sum_{n}^{q} \binom{p}{m} \binom{q}{n} (-\bar{x})^{(p-m)} (-\bar{y})^{(q-n)} M_{mn}$$

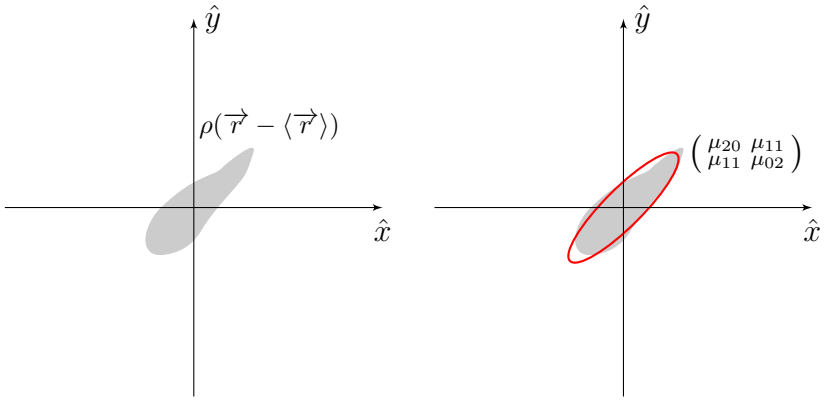

Figure 89: 2-D Central Distribution and Covariance

5.4.2 Covariance

The three second order central moments make up the covariance matrix. The mass weighted covariance is defined as follows.

$$cov(\rho(\overrightarrow{r})) = \begin{pmatrix} \mu_{20} & \mu_{11} \\ \mu_{11} & \mu_{02} \end{pmatrix}$$

Covariance provides a general second order measurement that is independent of the first order moment, or position of the distribution. The covariance matrix may be used to fit the shape parameters of an ellipse or 2D gaussian.

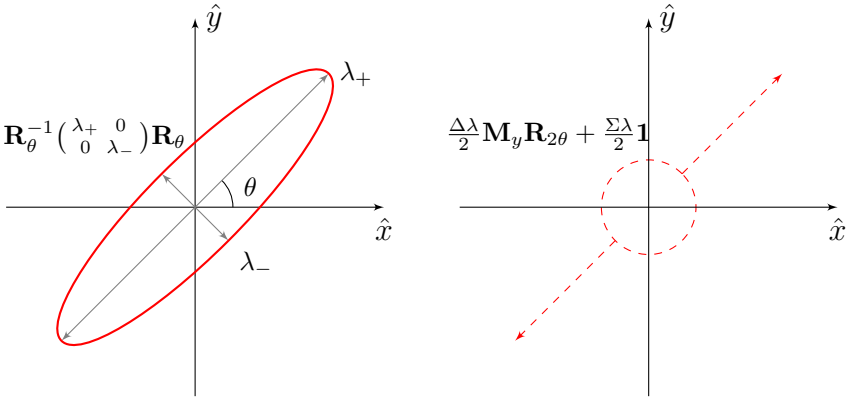

Figure 90: Covariance Eigenvectors and Components

Extracting the eigenvalues λ_+ and λ_- and diagonalizing the covariance matrix allows for

the following representation. This process is equivalent to 2D principal component analysis. The angle θ represents the orientation of the principal eigenvector.

$$cov = \begin{pmatrix} \cos\theta & -\sin\theta \\ \sin\theta & \cos\theta \end{pmatrix} \begin{pmatrix} \lambda_+ & 0 \\ 0 & \lambda_- \end{pmatrix} \begin{pmatrix} \cos\theta & \sin\theta \\ -\sin\theta & \cos\theta \end{pmatrix}$$

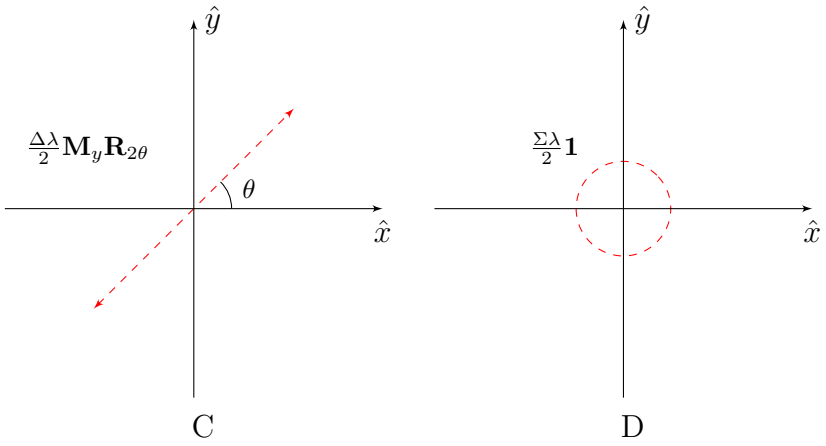

Figure 91: Covariance Components

5.4.3 Covariance Components

Carrying out the matrix multiplication and separating the result into its traceless symmetric part, C, and isotropic part, D, yields the following. [20]

$$cov = \frac{\lambda_+ - \lambda_-}{2} \begin{pmatrix} \cos 2\theta & \sin 2\theta \\ \sin 2\theta & -\cos 2\theta \end{pmatrix} + \frac{\lambda_+ + \lambda_-}{2} \begin{pmatrix} 1 & 0 \\ 0 & 1 \end{pmatrix}$$

Matrix D is the rotationally invariant component of the covariance.

$$D = \frac{Tr(cov)}{2}\mathbf{1} = \frac{\lambda_+ + \lambda_-}{2} \begin{pmatrix} 1 & 0 \\ 0 & 1 \end{pmatrix}$$

Subtracting D from the covariance yields C, the rotationally variant component of the covariance matrix.

$$C = cov - D = \frac{\lambda_+ - \lambda_-}{2} \begin{pmatrix} \cos 2\theta & \sin 2\theta \\ \sin 2\theta & -\cos 2\theta \end{pmatrix}$$

$$\begin{pmatrix} \cos 2\theta & \sin 2\theta \\ \sin 2\theta & -\cos 2\theta \end{pmatrix} = \begin{pmatrix} 1 & 0 \\ 0 & -1 \end{pmatrix} \begin{pmatrix} \cos 2\theta & \sin 2\theta \\ -\sin 2\theta & \cos 2\theta \end{pmatrix} = \mathbf{S}_0\mathbf{R}_{2\theta}$$

This rotationally variant component of the covariance consists of a rotation matrix and reflection, the symmetry components of the D_2 group.

This way we can express the covariance in terms of these two components.

$$cov = C + D = \frac{\Delta\lambda}{2}\mathbf{S}_0\mathbf{R}_{2\theta} + \frac{\Sigma\lambda}{2}\mathbf{1}$$

The orientation angle θ is calculated by the formula below.

$$\theta = \frac{1}{2}\tan^{-1}\left(\frac{2\mu_{11}}{\mu_{20} - \mu_{02}}\right)$$

The eigenvalues are calculated as follows.

$$\lambda_i = \frac{\mu_{20} + \mu_{02}}{2} \pm \frac{\sqrt{4\mu_{11}^2 + (\mu_{20} - \mu_{02})^2}}{2}$$

We may represent the covariance with an ellipse as in Figure 90. Alternately we may view the covariance matrix as the graphical additions of its two components C and D. This is shown in Figure 91. The isotropic component of the covariance, D, is rotationally invariant so it is represented by a circle. The traceless symmetric component, C, is represented by a vector of magnitude $\frac{\Delta\lambda}{2}$. Since this component varies as 2θ the vector is also drawn 180

degrees out of phase, making it a double sided arrow.

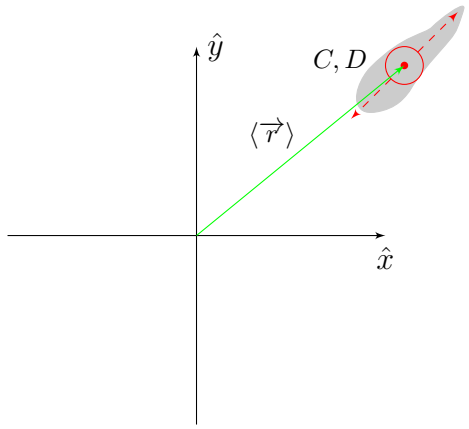

Figure 92: 2nd Order Approximation

5.4.4 Vectorization of Non-Isotopic Covariance Component

We use a vector representation of the C matrix by creating a vector $\overrightarrow{c}$ which carries the angle and magnitude of the C matrix transformation.

$$\overrightarrow{c} = \frac{\Delta\lambda}{2} \begin{pmatrix} \cos 2\theta \\ \sin 2\theta \end{pmatrix} = ce^{i2\theta}$$

The magnitude of the vector $\overrightarrow{c}$ is $Det(C)$, the difference between eigenvalues of the covariance matrix. This parameter is a monotonically increasing function of the eccentricity of the ellipse. If $c = 0$ the covariance matrix is degenerate, meaning ρ has circular symmetry up to second order.

$$c = |\overrightarrow{c}| = \sqrt{Det(C)} = \frac{\lambda_+ - \lambda_-}{2} = \frac{\Delta\lambda}{2}$$

Normalizing the vector $\overrightarrow{c}$ isolates the rotational feature.

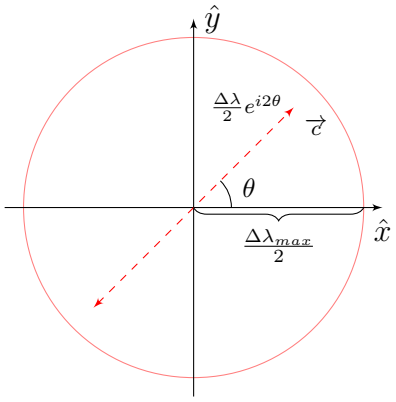

Figure 93: Vectorizing C

$$\hat{c} = \frac{\vec{c}}{c} = \begin{pmatrix} \cos 2\theta \\ \sin 2\theta \end{pmatrix} = e^{i2\theta}$$

5.4.5 Normalization

Though the rotational feature θ can be extracted from any distribution its importance as a metric feature diminishes as the magnitude of $\vec{c}$ decreases. By adding an extra dimensional component to the vector $\vec{c}$ we can generate a feature vector of unit length. Here we work to represent $\vec{c}$ as in Figure 94, the projection of a vector $\vec{\zeta}$ with fixed length ζ and an angle γ with the image plane normal.

First we identify c_{max} as the upper bound on c.

$$c_{max} = max(\frac{\Delta\lambda}{2}) = \frac{\Delta\lambda_{max}}{2}$$

Next we use c_{max} to represent c as the component of ζ projected into $x-y$ image plane.

$$\sin\gamma = \frac{c}{c_{max}}$$

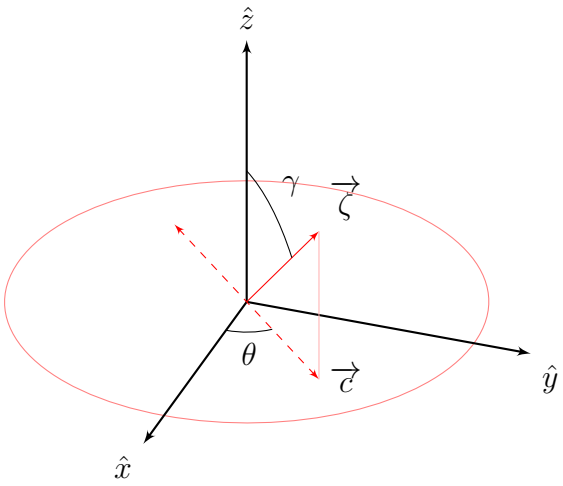

Figure 94: Projection of ζ onto the image plane

We define this 3-D vector $\overrightarrow{\zeta}$ and its components as follows.

$$\overrightarrow{\zeta} = c_{max} \begin{pmatrix} \sqrt{1-c^2} \\ \frac{c}{c_{max}}\hat{c} \end{pmatrix} = c_{max} \begin{pmatrix} \cos\gamma \\ \sin\gamma e^{i2\theta} \end{pmatrix}$$

Normalization yields the feature vector $\hat{\zeta}$. This is the basis of single particle representation.

$$\hat{\zeta} = \begin{pmatrix} \cos\gamma \\ \sin\gamma e^{i2\theta} \end{pmatrix} = \begin{pmatrix} \cos\gamma \\ \sin\gamma\hat{c} \end{pmatrix}$$

5.5 Single Particle Similarity Metric Z

We use the above representation to construct a similarity metric Z which is invariant to centroid values. Consider a second distribution $\rho_2(\overrightarrow{r})$ as shown in Figure 95.

For this second distribution we calculate the non-isotopic covariance component vector $\overrightarrow{c}_2$ and normalize it to find the feature vector $\hat{\zeta}_2$ as shown in Figure 96.

We generate a similarity metric Z between second order feature vectors $\hat{\zeta}$ using the inner product of the vectors. Note this metric is independent of the centroid values of each dis-

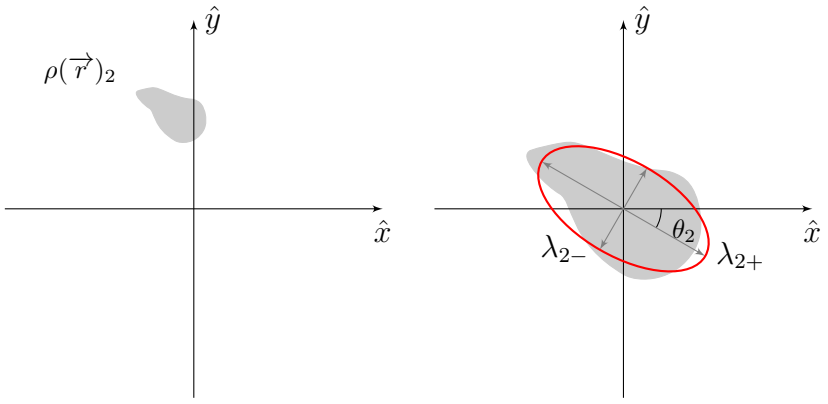

Figure 95: Distribution 2

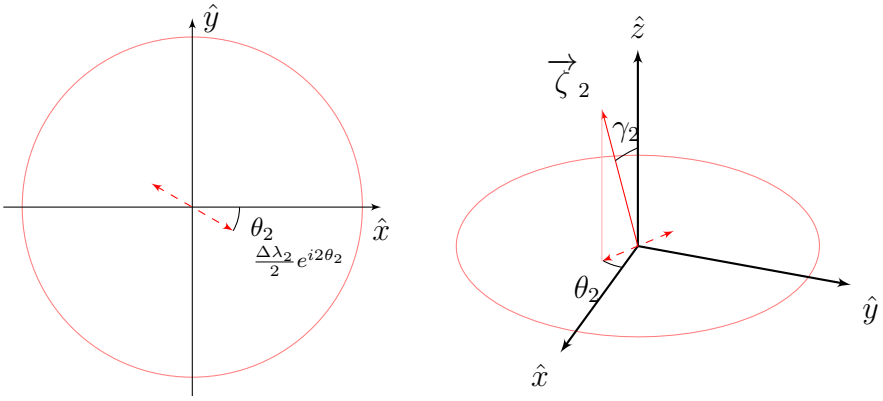

Figure 96: Vectorization and Normalization

tribution, meaning it only takes into account the ellipses' eccentricity and orientation in measuring their similarity.

$$Z_{12} = \hat{\zeta}_1 \cdot \hat{\zeta}_2$$

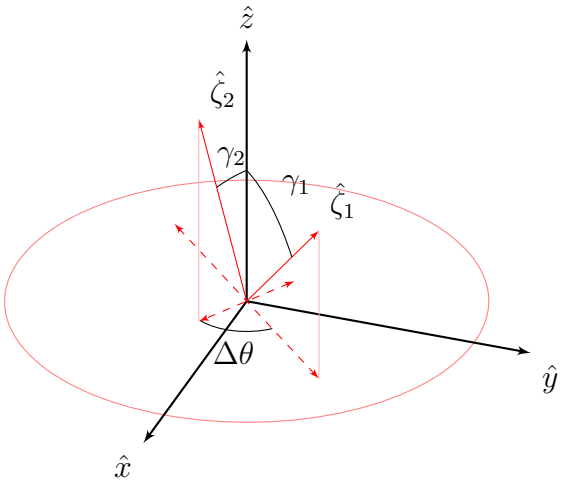

Figure 97: Two Second Order Feature Vectors

The value of the inner product of the $\hat{\zeta}$ vectors can be expressed in terms of the γ angles of each distribution and the inner product of the $\overrightarrow{c}$ vectors.

$$\hat{\zeta}_1 \cdot \hat{\zeta}_2 = \cos\gamma_1 \cos\gamma_2 + \sin\gamma_1 \sin\gamma_2 \hat{c_1} \cdot \hat{c_2}$$

In turn, the inner product of the $\overrightarrow{c}$ vectors, can be expressed as the cosine of twice the angle between them.

$$\hat{c_1} \cdot \hat{c_2} = \cos\left(2\theta_1 - 2\theta_2\right)$$

Therefore the similarity metric may be written to follow Figure 97.

$$Z_{12} = \cos\gamma_1 \cos\gamma_2 + \sin\gamma_1 \sin\gamma_2 \cos 2\Delta\theta$$

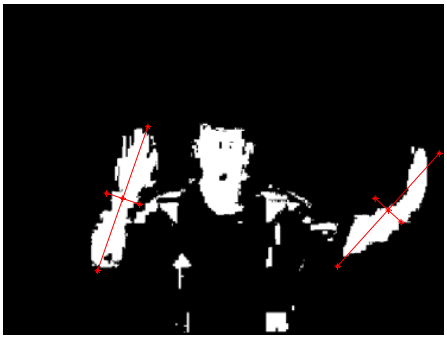

Figure 98: Arm Tracking

5.6 Two Particle Representation

Now we introduce a distribution which contains two blobs such as in Figure 98. These two regions represent the skin pixels created by exposed forearms. Moment analysis up to second order is performed on each blob. This generates both the centroid and covariance of each distribution. Figure 99 shows the first and second order moments of two distributions..

5.6.1 Two Component Centroid and Covariance

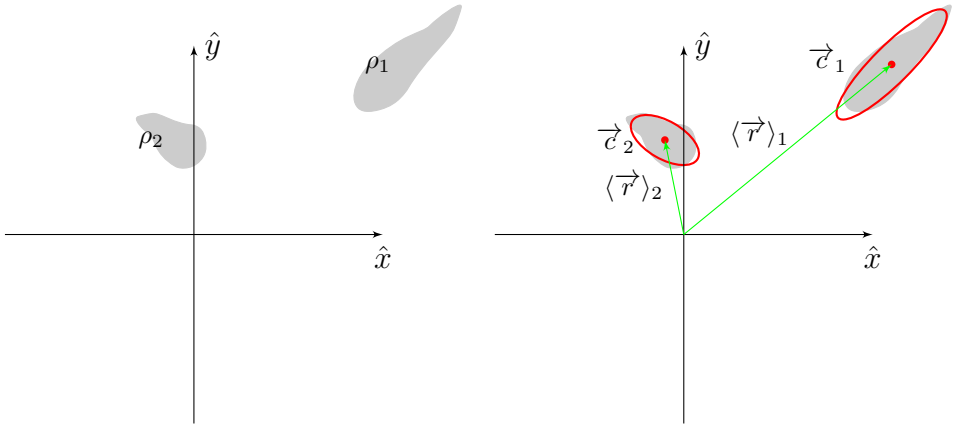

Figure 99: Two Component Distribution

We extract translationally invariant features by changing the coordinate basis to the average centroid value $\langle \overrightarrow{r} \rangle_{12}$ and their relative displacement from that center $\pm \overrightarrow{\alpha}$. These are the symmetric and antisymmetric combinations of the centroids $\overrightarrow{r}_1$ and $\overrightarrow{r}_2$. This change of

basis is shown in Figure 100.

$$\langle \overrightarrow{r} \rangle_{12} = \frac{\langle \overrightarrow{r} \rangle_1 + \langle \overrightarrow{r} \rangle_2}{2}$$

$$\overrightarrow{\alpha} = \frac{\langle \overrightarrow{r} \rangle_1 - \langle \overrightarrow{r} \rangle_2}{2}$$

This yields a set of values $(\overrightarrow{c}_1, \overrightarrow{c}_2, \overrightarrow{\alpha})$ which is invariant to translation.

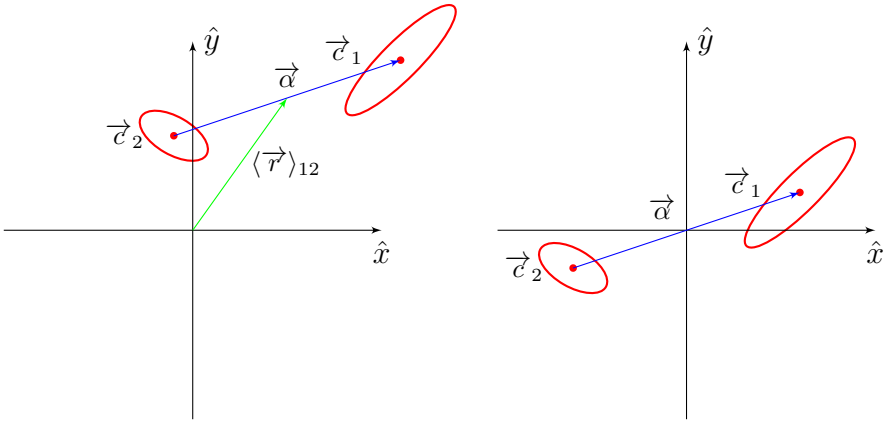

Figure 100: Feature Set of Two Distributions

The relative displacement $\overrightarrow{\alpha}$ has a magnitude α and direction $\hat{\alpha}$.

$$\overrightarrow{\alpha} = \alpha e^{i\phi} = \alpha\hat{\alpha}$$

5.6.2 Relative Displacement Normalization

Normalizing $\overrightarrow{c}_1$ and $\overrightarrow{c}_2$ yields $\overrightarrow{\zeta}_1$ and $\overrightarrow{\zeta}_2$. We apply the same technique to normalize $\overrightarrow{\alpha}$. By adding an extra dimensional component to the vector $\overrightarrow{\alpha}$ we can generate a feature vector of unit length.

Here we work to represent $\overrightarrow{\alpha}$ as in Figure 101, the projection of a vector $\overrightarrow{\nu}$ with fixed length α_{max} and an angle β with the image plane normal.

The maximum value for α is used as an upper limit.

$$\alpha_{max} = max(\alpha)$$

Next we use α_{max} to represent α as the component of ν projected into xy image plane.

$$\sin\beta = \frac{\alpha}{\alpha_{max}}$$

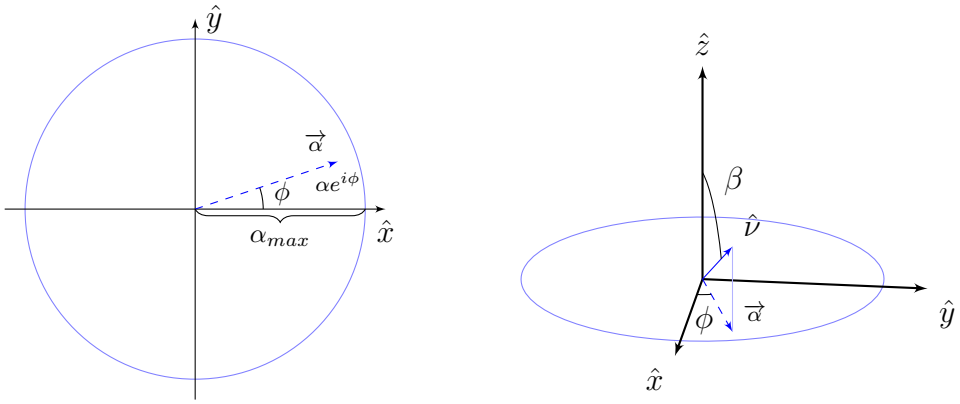

Figure 101: Relative Displacement Normalization

We define this 3-D vector $\vec{\nu}$ and its components as follows.

$$\vec{\nu} = \alpha_{max} \begin{pmatrix} \sqrt{1-\alpha^2} \\ \frac{\alpha}{\alpha_{max}}\hat{\alpha} \end{pmatrix} = \alpha_{max} \begin{pmatrix} \cos\beta \\ \sin\beta e^{i\phi} \end{pmatrix}$$

Normalization yields the feature vector $\hat{\nu}$.

$$\hat{\nu} = \begin{pmatrix} \cos\beta \\ \sin\beta e^{i\phi} \end{pmatrix} = \begin{pmatrix} \cos\beta \\ \sin\beta\hat{\alpha} \end{pmatrix}$$

This leaves us with a set of values $(\hat{\zeta}_1, \hat{\zeta}_2, \hat{\nu}, \hat{u})$ representing the state of a 3-D kinematic chain which projected onto the 2-D xy image plane yields terms $(\vec{c}_1, \vec{c}_2, \vec{\alpha}, \vec{\eta})$.

5.7 Two Particle Similarity Metric Z

Generating a similarity metric for comparing images A and B, each of which consists distributions 1 and 2, is not straightforward. While the similarity metric between two single particle distributions is well defined as $\hat{\zeta}_A \cdot \hat{\zeta}_B$, it is not clear how to apply this for two particle poses.

$$Z_{AB} \neq \Sigma(\hat{\zeta}_{1A} \cdot \hat{\zeta}_{1B}, \hat{\zeta}_{2A} \cdot \hat{\zeta}_{2B}, \hat{\nu}_A \cdot \hat{\nu}_B)$$

There is an ambiguity as to which blob is labeled 1 and which is labeled 2, making it unclear how to generate the inner product. Observe that switching the labels 1 and 2 reverses the sign of $\overrightarrow{\alpha}$.

What is needed is a representation which is invariant to labeling convention but also serves in constructing a similarity metric and reconstructing the geometric feature set ($\overrightarrow{c}_1$, $\overrightarrow{c}_2$, $\overrightarrow{\alpha}$).

5.7.1 Combined Moment Expansion

We approach this problem by considering both distributions together as a single distribution and perform a 3rd order moment analysis. This analysis should generate features which are invariant to labeling convention as we are performing the moment expansion without their application.

In order to calculate the moments of the total distribution we add the two blobs single image moments.

$$M_{ij} = {}_1M_{ij} + {}_2M_{ij}$$

The zero moments simply add as follows.

$$M_{00} = {}_1M_{00} + {}_2M_{00}$$

Now consider calculating the centroid of the total image.

$$\langle \overrightarrow{r} \rangle = \frac{1}{M_{00}} \begin{pmatrix} M_{10} \\ M_{01} \end{pmatrix} = \frac{{}_1M_{00}\langle \overrightarrow{r} \rangle_1 + {}_2M_{00}\langle \overrightarrow{r} \rangle_2}{{}_1M_{00} + {}_2M_{00}}$$

Weighting each distribution equally yields a total distribution centroid which is the center point between the two individual centroids, or their symmetric component.

$$\langle \overrightarrow{r} \rangle = \frac{\langle \overrightarrow{r} \rangle_1 + \langle \overrightarrow{r} \rangle_2}{2}$$

The higher order central moments are calculated as follows.

$$\mu_{pq}^{total} = {}_1m_{pq} + {}_2m_{pq}$$

5.7.2 Individual Moment Contributions

Shift the integration from the individual particles' center of mass to the new center of mass. The vector $\binom{a}{b}$ is the position of the blob with respect to the new center of mass.

$$m_{pq} = \sum_x \sum_y (x - \bar{x} + a)^p (y - \bar{y} + b)^q \rho(\overrightarrow{r})$$

$$m_{20} = \mu_{20} + M_{00}a^2$$

$$m_{02} = \mu_{02} + M_{00}b^2$$

$$m_{11} = \mu_{11} + M_{00}ab$$

$$m_{30} = \mu_{30} + 3a\mu_{20} + M_{00}a^3$$

$$m_{03} = \mu_{03} + 3b\mu_{02} + M_{00}b^3$$

$$m_{21} = \mu_{21} + 2a\mu_{11} + b\mu_{20} + M_{00}ba^2$$

$$m_{12} = \mu_{12} + 2b\mu_{11} + a\mu_{02} + M_{00}ab^2$$

When we add up the contributions from each distribution we use the following identities to represent expressions with (a_1, b_1, a_2, b_2) in terms of α and ϕ.

$$\begin{pmatrix} a_1 \\ b_1 \end{pmatrix} = -\begin{pmatrix} a_2 \\ b_2 \end{pmatrix}$$

$$\begin{pmatrix} a_1 \\ b_1 \end{pmatrix} = \alpha \begin{pmatrix} \cos\phi \\ \sin\phi \end{pmatrix}$$

$$\alpha = \sqrt{a_1^2 + b_1^2}$$

$\binom{a}{b}_1$ will be written $\binom{a}{b}$ while $\binom{a}{b}_2$ will be written as $-\binom{a}{b}$.

5.7.3 Combined Second Moment Expansion

Using the above formula we write the combined second moment terms for distributions 1 and 2.

$$\mu_{20}^{total} = {}_1\mu_{20} + {}_2\mu_{20} + 2a^2$$

$$\mu_{02}^{total} = {}_1\mu_{02} + {}_2\mu_{02} + 2b^2$$

$$\mu_{11}^{total} = {}_1\mu_{11} + {}_2\mu_{11} + 2ab$$

In terms of the θ and λ values of each particle and α and ϕ which relate their relative centroid positions, the combined second order moments read as follows.

$$\mu_{20}^{total} = \frac{\Sigma\lambda_1 + \Sigma\lambda_2}{2} + \alpha + \left(\frac{\Delta\lambda_1}{2}\cos 2\theta_1 + \frac{\Delta\lambda_2}{2}\cos 2\theta_2 + \alpha\cos 2\phi\right)$$

$$\mu_{20}^{total} = \frac{\Sigma\lambda_1 + \Sigma\lambda_2}{2} + \alpha - \left(\frac{\Delta\lambda_1}{2}\cos 2\theta_1 + \frac{\Delta\lambda_2}{2}\cos 2\theta_2 + \alpha\cos 2\phi\right)$$

$$\mu_{11}^{total} = \frac{\Delta\lambda_1}{2}\sin 2\theta_1 + \frac{\Delta\lambda_2}{2}\sin 2\theta_2 + \alpha\sin 2\phi$$

The terms $\alpha\cos 2\phi$ and $\alpha\sin 2\phi$ are simply the x and y components of $\alpha e^{2i\phi}$.

$$\alpha e^{2i\phi} = \frac{\overrightarrow{c}_1 + \overrightarrow{c}_2}{c_{max}} = \left(\begin{smallmatrix}1 & 0 & 0\\ 0 & 1 & 0\end{smallmatrix}\right)(\overrightarrow{\nu}e^{i\phi})$$

Similarly, the terms involving λ and θ are the x and y components of the symmetric combination of $\frac{\overrightarrow{c}}{\zeta}$ values for each particle.

$$\frac{\overrightarrow{c}_1 + \overrightarrow{c}_2}{c_{max}} = \left(\begin{smallmatrix}1 & 0 & 0\\ 0 & 1 & 0\end{smallmatrix}\right)(\hat{\zeta}_1 + \hat{\zeta}_2)$$

5.7.4 Combined Third Moment Expansion

Below we write the combined third moment terms.

$$\mu_{30}^{total} = {}_1\mu_{30} + {}_2\mu_{30} + 3a\left({}_1\mu_{20} - {}_2\mu_{20}\right)$$

$$\mu_{03}^{total} = {}_1\mu_{03} + {}_2\mu_{03} + 3b\left({}_1\mu_{02} - {}_2\mu_{02}\right)$$

$$\mu_{21}^{total} = {}_1\mu_{21} + {}_2\mu_{21} + 2a\left({}_1\mu_{11} - {}_2\mu_{11}\right) + b\left({}_1\mu_{20} - {}_2\mu_{20}\right)$$

$$\mu_{12}^{total} = {}_1\mu_{12} + {}_2\mu_{12} + 2b\left({}_1\mu_{11} - {}_2\mu_{11}\right) + a\left({}_1\mu_{02} - {}_2\mu_{02}\right)$$

In terms of the θ and λ values of each particle and α and ϕ which relate their relative centroid positions, the combined third order moments read as follows.

$$\mu_{30}^{total} = 3\alpha\cos\phi\left(\frac{\Delta\lambda_1}{2}\cos 2\theta_1 - \frac{\Delta\lambda_2}{2}\cos 2\theta_2\right)$$

$$\mu_{03}^{total} = -3\alpha\sin\phi\left(\frac{\Delta\lambda_1}{2}\cos 2\theta_1 - \frac{\Delta\lambda_2}{2}\cos 2\theta_2\right)$$

$$\mu_{21}^{total} = 2\alpha\cos\phi\left(\frac{\Delta\lambda_1}{2}\sin 2\theta_1 - \frac{\Delta\lambda_2}{2}\sin 2\theta_2\right) + \alpha\sin\phi\left(\frac{\Delta\lambda_1}{2}\cos 2\theta_1 - \frac{\Delta\lambda_2}{2}\cos 2\theta_2\right)$$

$$\mu_{12}^{total} = 2\alpha\sin\phi\left(\frac{\Delta\lambda_1}{2}\sin 2\theta_1 - \frac{\Delta\lambda_2}{2}\sin 2\theta_2\right) - \alpha\cos\phi\left(\frac{\Delta\lambda_1}{2}\cos 2\theta_1 - \frac{\Delta\lambda_2}{2}\cos 2\theta_2\right)$$

The terms $\alpha\cos\phi$ and $\alpha\sin\phi$ are simply the x and y components of $\alpha e^{i\phi}$ or $\overrightarrow{\nu}$. Similarly, the terms involving λ and θ are the x and y components of the antisymmetric combination of $\hat{c}$ values for each particle. These are the x and y components of $\hat{c}_1 - \hat{c}_2$ or $\hat{\zeta}_1 - \hat{\zeta}_2$. The terms are always found as a product so that we may describe them as the terms of the outer product of $\hat{\nu}$ and $\hat{\zeta}_1 - \hat{\zeta}_2$. The third order moments correspond to the linear combination of terms from $(\hat{\zeta}_1 - \hat{\zeta}_2) \otimes \hat{\nu}$.

By inspection we can see that both $\hat{\zeta}_1 - \hat{\zeta}_2$ and $\hat{\nu}$ switch sign on reversing the index of the blobs 1 and 2. Therefore the outer product $(\hat{\zeta}_1 - \hat{\zeta}_2) \otimes \hat{\nu}$ is invariant to reversing index of the two blobs since the reversal of sign in each term of the product cancels out. This follows the required criteria for a well behaved representation from which we can construct a similarity function Z.

5.7.5 Index Invariant Similarity Function Z

We define a state set Ψ as follows.

$$\Psi = [\alpha e^{i2\phi}, \hat{\zeta}_1 + \hat{\zeta}_2, (\hat{\zeta}_1 - \hat{\zeta}_2) \otimes \hat{\nu}]$$

Using this state set Ψ we may define the similarity function Z_{AB} between state Ψ_A and Ψ_B as the inner product.

$$Z_{AB} = \Psi_A \cdot \Psi_B$$

5.8 Multi-Particle Pose Representation

Finally we have the mathematical tools to effectively represent the image signals which come from face recognition and skin recognition for two arm frontal gestures.

First we consider the use of face recognition on an image. This will locate the part of an image which is recognized as a face. The following images show two arms and a face.

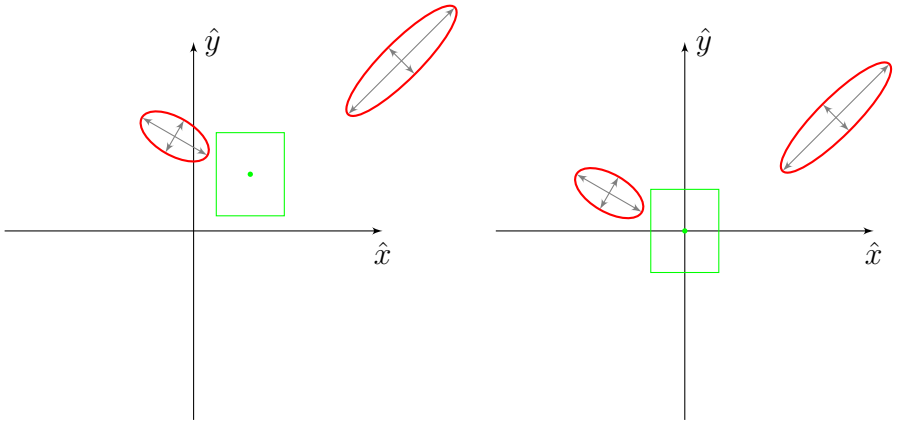

Figure 102: Two Arms Relative to Face

Our first feature vector will be the vector which goes from the center of the face $\langle \overrightarrow{r} \rangle_{face}$ to the center of arms $\langle \overrightarrow{r} \rangle_{12}$. We call this vector $\overrightarrow{\eta}$.

$$\overrightarrow{\eta} = \langle \overrightarrow{r} \rangle_{12} - \langle \overrightarrow{r} \rangle_{face}$$

In the images below we show on the left a synthetic model of a subject. The face to arms vector $\overrightarrow{\eta}$ is shown in green.

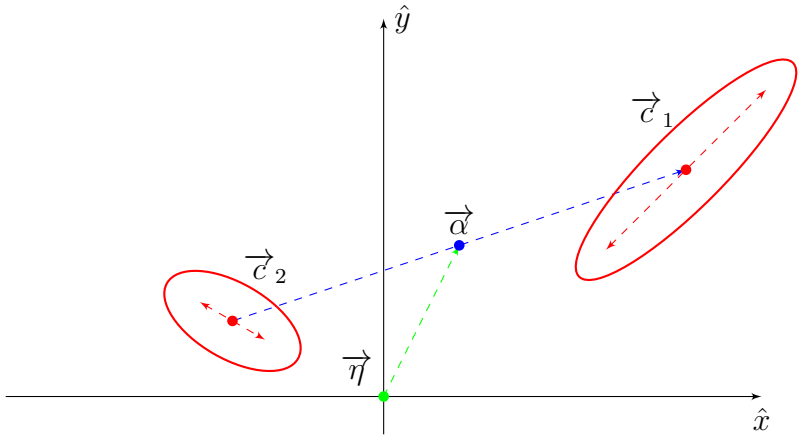

Figure 103: Two Arms Pose Relative to Face

5.8.1 Normalization

We apply the same technique to normalize $\overrightarrow{\eta}$. By adding an extra dimensional component to the vector $\overrightarrow{\eta}$ we can generate a feature vector of unit length.

Here we work to represent $\overrightarrow{\eta}$ as in Figure 104, the projection of a vector $\overrightarrow{u}$ with fixed length η_{max} and an angle φ with the image plane normal.

The maximum value for η may be measured from a calibration image.

$$\eta_{max} = max(\eta)$$

Next we use η_{max} to represent η as the component of u projected into xy image plane.

$$\sin\varphi = \frac{\eta}{\eta_{max}}$$

We define this 3-D vector $\overrightarrow{u}$ and its components as follows.

$$\overrightarrow{u} = \eta_{max} \begin{pmatrix} \sqrt{1 - \frac{\eta}{\eta_{max}}^2} \\ \frac{\eta}{\eta_{max}}\hat{\eta} \end{pmatrix} = \alpha_{max} \begin{pmatrix} \cos\varphi \\ \sin\varphi e^{i\vartheta} \end{pmatrix}$$

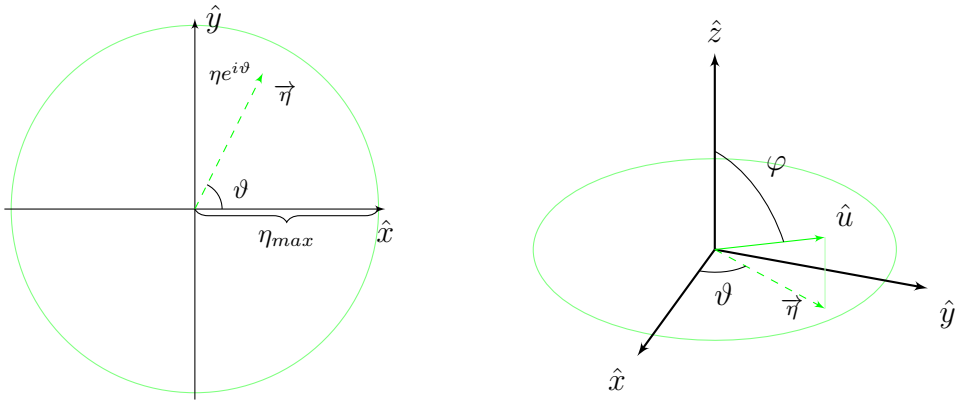

Figure 104: Arms Centroid Relative to Face

Normalization yields the feature vector $\hat{u}$.

$$\hat{u} = \begin{pmatrix} \cos\varphi \\ \sin\varphi e^{i\vartheta} \end{pmatrix} = \begin{pmatrix} \cos\varphi \\ \sin\varphi\hat{\eta} \end{pmatrix}$$

This leaves us with a set of values $(\hat{\zeta}_1, \hat{\zeta}_2, \hat{\nu}, \hat{u})$ representing the state of a 3-D kinematic chain which projected onto the 2-D xy image plane yields terms $(\overrightarrow{c}_1, \overrightarrow{c}_2, \overrightarrow{\alpha}, \overrightarrow{\eta})$. This is depicted explicitly in Figure 105.

5.9 Multi Particle Similarity Function Z

We define a state set Ψ as follows.

$$\Psi = [\hat{u}, \alpha e^{i2\phi}, \hat{\zeta}_1 + \hat{\zeta}_2, (\hat{\zeta}_1 - \hat{\zeta}_2) \otimes \hat{\nu}] = [\hat{u}, \hat{\nu}e^{i\phi}, \hat{\zeta}_+, \hat{\zeta}_- \otimes \hat{\nu}]$$

Using this state set Ψ we may define the similarity function Z_{AB} between state Ψ_A and Ψ_B as the inner product.

$$Z_{AB} = \Psi_A \cdot \Psi_B = \Sigma[\hat{u}_A \cdot \hat{u}_B, (\hat{\nu}e^{i\phi})_A \cdot (\hat{\nu}e^{i\phi})_B, \hat{\zeta}_{+A} \cdot \hat{\zeta}_{+B}, (\hat{\zeta}_- \otimes \hat{\nu})_A \cdot (\hat{\zeta}_- \otimes \hat{\nu})_B]$$

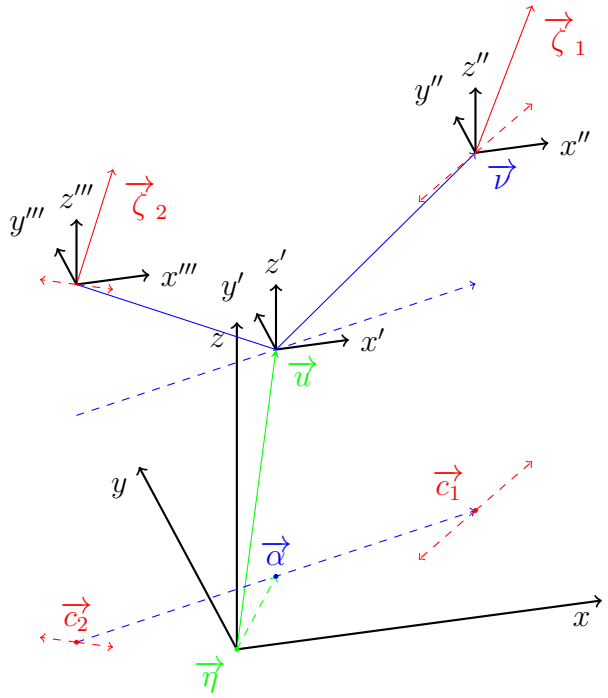

Figure 105: Multi-Particle Projection

5.10 Future Work

We build a simple model of the face, shoulders and arms with a kinematic chain based on the proportions of Vitruvian Man. The forearms are modeled as prolate ellipsoids. Image features ($\overrightarrow{c}_1, \overrightarrow{c}_2, \overrightarrow{\alpha}, \overrightarrow{\eta}$) are captured to build the geometric model.

The semaphore poses for the Vitruvian and the image extracted geometric model are shown in Figure 106. Each semaphore poses corresponds to a letter of the alphabet.

The image models and similarity metrics developed in this chapter deserve further research. They could be used as in Chapter 3 and 4 to generate Z/Z^* plots and extract the motion graphs for time series.

This $[\hat{u}, \hat{\nu}e^{i\phi}, \hat{\zeta}_+, \hat{\zeta}_- \otimes \hat{\nu}]$ representation could also be used in human interface as a feature set suited for recognition of physical poses or gestures. Expanding the model to include more color channels through the use of clothing would also interesting to explore.

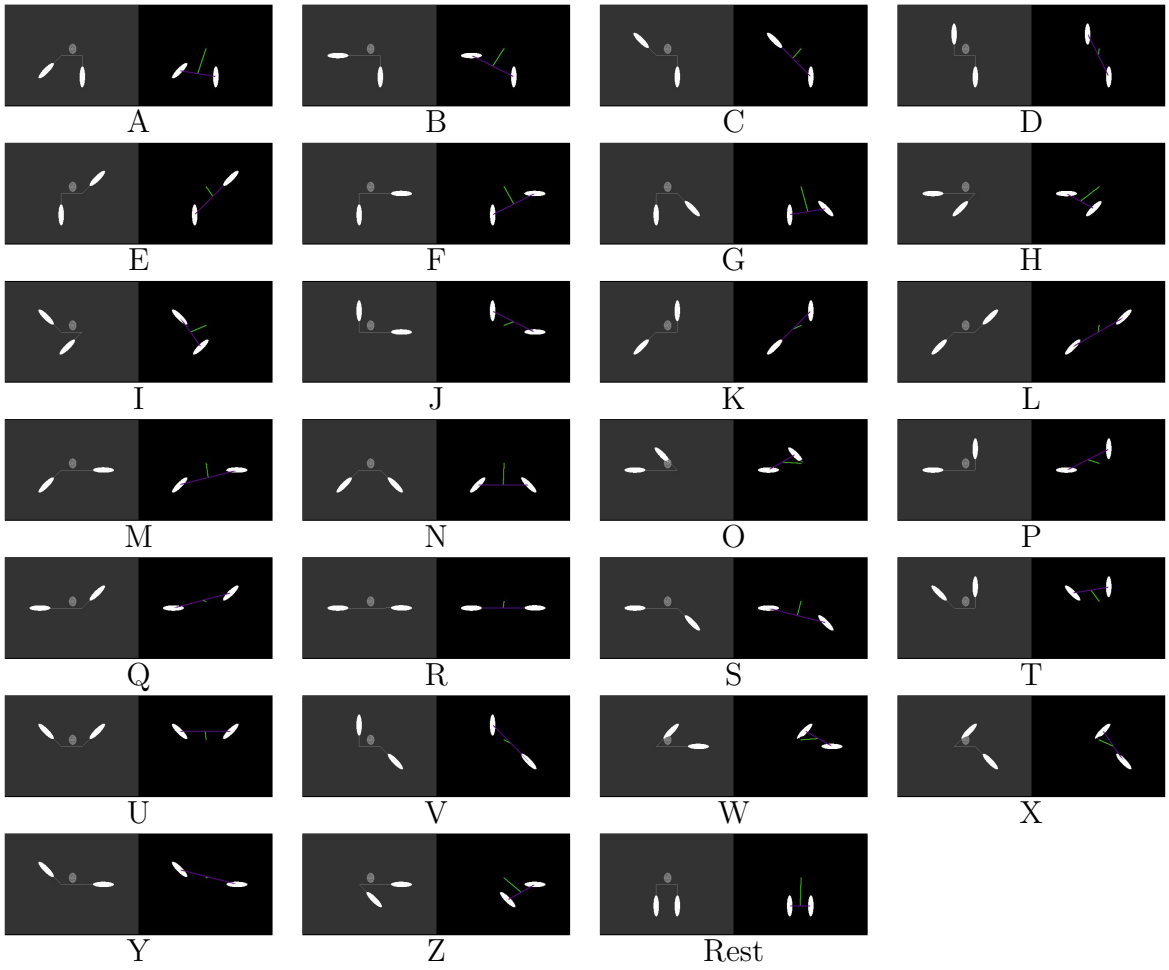

Figure 106: Semaphore Poses

It would also be fruitful to use a range finding video system such as that in the Kinect camera which delivers color video with an alpha channel representing depth of the image. Combined with color segmentation the depth of field measurements would enhance the model greatly and lift certain degeneracies in the above model.

6 Conclusion

In this thesis we developed a kinematic chain model of the human body using a quaternionic symmetry basis. A distance metric and pseudo metric were developed to measure symmetry and similarity between model configurations. The metric space generated by each was used over a movement time series to form a colored similarity plot representing the information of both. The movement features and motion graph topologies corresponding to similarity plot motifs were presented. Similarity plots and motion graphs were constructed for longer motion series of subjects performing traditional movement choreographies from yoga and karate. All the work using kinematic chains and motion capture data was developed in Chapters 2 and 3.

An equivalent method of analysis was applied to video sequences of dancers in Chapter 4. We presented a segmentation algorithm to extract the body image and distance metric based on the overlap integral of the body image functions. We showed similarity plots and the derived motion graphs for two subjects. We reconstructed the virtual subjects in a 3D space. The application of a dynamic Markov network on the motion graph was shown to be successful in directing a virtual subject toward a target location.

A more sophisticated model for human subjects on video was described in Chapter 5. The use of OpenCV's face recognition algorithm, color based segmentation methods and cartesian moment analysis in generating feature sets was shown. We detailed the use of third order moment analysis to derive a proper distance metric. This representation is shown to span the space of semaphore language.

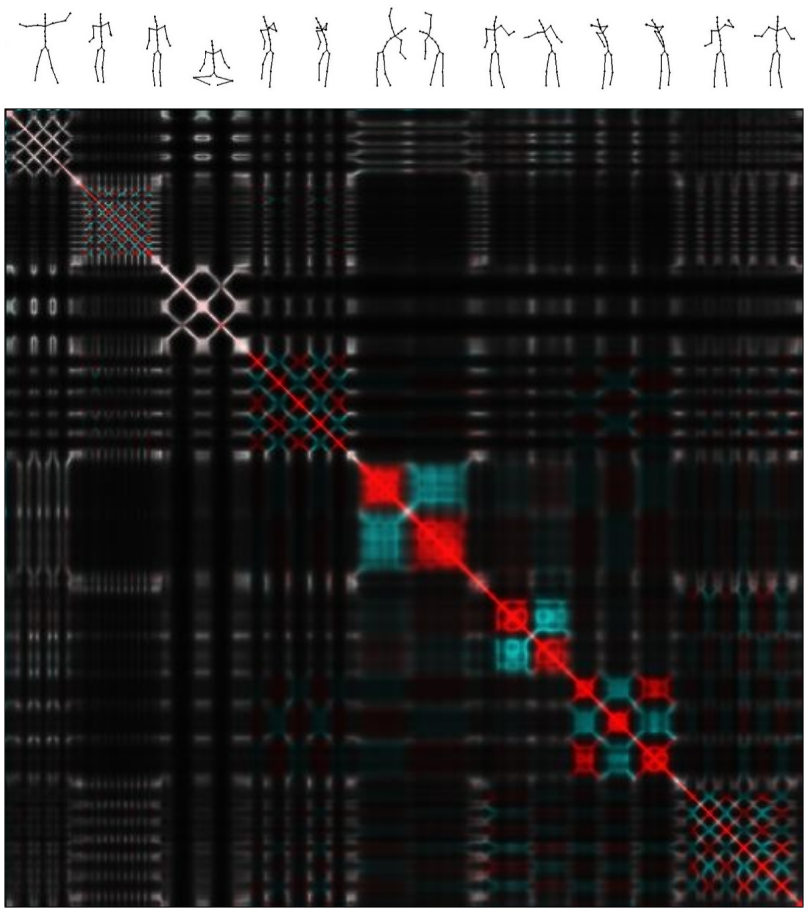

(Z_{ij}, Z^*_{ij})

Figure 107: Color Similarity Plot

References

[1] Openkinect, March 2012. URL `http://openkinect.org/`.

[2] Masayuki Akamatsu. aka.objects, March 2010. URL `http://www.iamas.ac.jp/~aka/max/`.

[3] Gazihan Alankus. Animating character navigation using motion graphs. Master's thesis, Middle East Technical University, 2005.

[4] Paul Allard. *Three-Dimensional Analysis of Human Movement*. Human Kinetics, 1995.

[5] John G. Allen, Richard Y. D. Xu, and Jesse S. Jin. Object tracking using camshift algorithm and multiple quantized feature spaces. In *Proceedings of the Pan-Sydney Area Workshop on Visual Information Processing*, VIP '05, pages 3–7. School of Information Technologies at the University of Sydney, Australian Computer Society, Inc., 2004.

[6] *Small, Low Power, 3-Axis ±3 gi MEMS® Accelerometer ADXL330*. Analog Devices Inc., One Technology Way, P.O. Box 9106, Norwood, MA 02062-9106, U.S.A., 2007.

[7] O. Arikan and D. A. Forsyth. Interactive motion generation from examples. In *Proceedings of the 29th Annual Conference on Computer Graphics and Interactive Techniques*, SIGGRAPH '02, pages 483–490. ACM, 2002.

[8] Werner Bailer, Peter Schallauer, Harald Bergur Haraldsson, and Herwig Rehatschek. Optimized mean shift algorithm for color segmentation in image sequences. In *Proceedings of the Conference on Image and Video Communications and Processing*, 2005.

[9] R. Begg and M. Palaniswami. *Computational intelligence for movement sciences: neural networks and other emerging techniques*. Computational intelligence and its applications series. Idea Group Pub., 2006.

[10] Thomas J. Binga and Edward F. Redish. Symbolic manipulators affect mathematical mindsets. *American Journal of Physics*, 76(45):418–424, April/May 2008.

[11] Richard A. Bolt. Put-that-there: Voice and gesture at the graphics interface. In *Proceedings of the 7th Annual Conference on Computer Graphics and Interactive Techniques*, SIGGRAPH '80, pages 262–270, Cambridge, Massachusetts 02139, 1980. Architecture Machine Group at Massachusetts Institute of Technology, ACM.

[12] Gary R. Bradski. Computer vision face tracking for use in a perceptual user interface. *Intel Technology Journal Q2 '98*, pages 1–15, 1998.

[13] Matthew Brand and Aaron Hertmann. Style machines. In *MERL TR2000-14 Conference Proceedings, SIGGRAPH*, 2000.

[14] Gabriele Brandstetter and Hortensia Volkers, editors. *ReMembering the Body*. Hatje Cantz Publishers, 2000.

[15] C. Bregler. Tracking people with twists and exponential maps, 1998. URL `citeseer.ist.psu.edu/bregler98tracking.html`.

[16] Claudia Carello and M.T. Turvey. Physics and psychology of the muscle sense. *Current Directions in Psychological Science*, 13:25–28, 2004.

[17] James Davis and Gary Bradski. Real-time motion template gradients using intel cvlib. In *IEEE ICCV Workshop on Framerate Vision*. MIT Media Lab and Intel Corporation, 1999.

[18] Don Rutledge Day and Rabindranath Dutta. Using video image analysis to automatically transmit gestures over a network in a chat or instant messaging, patent number 7039676, May 2006.

[19] Richard O. Duda, Peter E. Hart, and David G. Stork. *Pattern Classification*. John Wiley, second edition, 2001.

[20] Thomas C. Farrar and John E. Harriman. *Density Matrix Theory and its Applications in NMR Spectroscopy*, chapter 5, pages 170–180. Farragut Press, January 1995.

[21] Jan Flusser. Moment invariants in image analysis. *Transactions on Engineering, Computing and Technology*, 11:196–201, 2006.

[22] Jan Flusser, Jiri Boldys, and Barbara Zitova. Moment forms invariant to rotation and blur in arbitrary number of dimensions. *IEEE Transactions on Pattern Analysis and Machine Intelligence*, 25:234–246, 2003.

[23] David A. Forsyth and Jean Ponce. *Computer Vision*. Prentice Hall, 2003.

[24] Herbert Goldstein. *Classical Mechanics*. Addison Wesley, second edition, 1980.

[25] Morton Hammermesh. *Group Theory and its Application to Physical Problems*. Dover, 1962.

[26] Kris E. Hatlelid, William D. Harrison, and Ken G. Kavanagh. Remote communication through visual representations, patent number 6522333, Feb 2003.

[27] Ming-Kuei Hu. Visual pattern recognition by moment invariants. In *IRE Transactions on Information Theory*, pages 179–187, 1962.

[28] Du Huynh. Metrics for 3d rotations: Comparison and analysis. *Journal of Mathematical Imaging and Vision*, 35:155–164, 2009.

[29] Tsuyoshi Ide. Pairwise symmetry decomposition method for generalized covariance analysis. In *Fifth IEEE International Conference on Data Mining*, pages 27–30. IBM Research, Tokyo Research Laboratory, 2005.

[30] *Open Source Computer Vision Library*. Intel Corporation, 1 edition, December 2000.

[31] Gerald Jacobs. The distribution and nature of colour vision among the mammals. *Biological Reviews*, 68(3):413–471, 1993.

[32] Weseley M. Johnson, J. R. Paul Hanna, and Richard J. Millar. Advances in dataflow programming languages. *ACM Computing Suveys*, 36(1):1–34, March 2004.

[33] L. Kovar, M. Gleicher, and F. Pighin. Motion graphs. In *Proceedings of the 29th Annual Conference on Computer Graphics and Interactive Techniques*, SIGGRAPH '02, pages 473–482. ACM, ACM, 2002.

[34] Astrid Twenebowa Larssen. *Computer Human Interaction*, volume 3101/2004, chapter Physical Computing – Representations of Human Movement in Human-Computer Interaction, pages 661–665. Springer Berlin / Heidelberg, 2004.

[35] Nianjun Liu and Brian C. Lovell. Mmx-accelerated real-time hand tracking system. In *IVCNZ 2001*, pages 381–385, Brisbane, Australia, 2001. Intelligent Real-Time Imaging and Sensing (IRIS) Group of the School of Computer Science and Electrical Engineering at The University of Queensland.

[36] M. Marcuso and R.M. Weber. Mathematical measurements using digital image capture. *American Journal of Physics*, 64(8):1080–1083, August 1996.

[37] Paulo Menezes, José Carlos Barreto, and Jorge Dias. Face tracking based on haar-like features and eigenfaces. In *IAV2004*, pages 5–7, 2004.

[38] R. Mukundan, S. H. Ong, and P. A. Lee. Image analysis by tchebichef moments. *IEEE Transactions on Image Processing*, 10:1357–1364, 2001.

[39] M.P. Murray, Z. Li, and S. S. Sastry. *A Mathematical Introduction to Robotic Manipulation*. CRC Press, 1994.

[40] Kenji Nagao and B. K. P. Horn. Direct object recognition using no higher than third order statistics of the image. A.I. Memo 1526, MIT Artificial Intellegence Laboratory, 1995.

[41] Marcin Novotni and Reinhard Klein. Shape retrieval using 3d zernike descriptors. *Computer-Aided Design*, 36:1047–1062, January 2004.

[42] Jean-Mark Pelletier. jit.freenect.grab. URL `http://jmpelletier.com`.

[43] Eric Pirard. *Image Analysis of Sediments Paleoenvironmental Reconstructions*, chapter Image Measurements. Francus, 2003.

[44] Katherine Ann Pullen. *Motion Capture Assisted Animation: Texturing and Synthesis*. PhD thesis, Stanford, 2002.

[45] Timothy J. Roberts, Stephen J. McKenna, and Ian W. Ricketts. Human tracking using 3d surface colour distributions. *Image and Computer Vision*, 24(12):1332–1342, Decemeber 2006.

[46] Ryan S. Russell and John B. Zipperer. Method and system for controlling an avatar using computer vision, patent number 6697072, Feb 2004.

[47] Edcel John Salumbides, Joyce Maristela, Alfredson Uy, and Kees Karremans. A vision-based motion sensor for undergraduate laboratories. *American Journal of Physics*, 70 (8):868–875, August 2002.

[48] Thomas Schlomer, Benjamin Poppinga, Niels Henze, and Susanne Boll. Gesture recognition with a wii controller. In *Proceedings of the 2nd International Conference on Tangible and Embedded Interaction*, pages 11–14. ACM, 2008.

[49] C.E. Shannon and W. Weaver. *The mathematical theory of communication*. University of Illinois Press, 1949.

[50] Claude Shannon, Noshirwan Petigara, and Satwiksai Seshasai. A mathematical theory of communication. *Bell System Technical Journal*, 27:379–423, 1948.

[51] Linda G. Shapiro and George C. Stockman. *Computer Vision*. Prentice Hall, 2001.

[52] P. K. Sinha, F. Y. Chen, and R. E. N. Horne. Fast recognition on general processor using moment invariants. *IEE Colloquium on Hough Transforms*, pages 1–4, 1993.

[53] Anthony Vernon Walker Smith, Alistair Ian Sutherland, Arnaud Lemoine, and Sean Mcgrath. Hand gesture recognition system and method, patent number 6128003, Oct 2000.

[54] Chris Stauffer and W.E.L. Grimson. Adaptive background mixture models for real-time tracking. In *Computer Vision and Patern Recognition*, volume 2, pages 246–252, Cambridge, MA 02139, 1999. The Artificial Intelligence Laboratory at the Massachusetts Institute of Technology, IEEE Computer Society.

[55] Dag Svanæs. *Understanding Interactivity: Steps to a Phenomenology of Human-Computer Interaction*. PhD thesis, Computer Science Department, NTNU, Trondheim, 2000.

[56] Maurizio Vannoni and Samuele Straulino. Low-cost accelerometers for physics experiments. *European Journal of Physics*, 28:781–787, July 2007.

[57] M. Whittle. *Gait analysis: an introduction*, volume 1 of *Gait Analysis*. Butterworth-Heinemann, 2002.

[58] Norbert Wiener. *Cybernetics: or Control and Communication in the Animal and Machine*. The MIT Press, second edition, 1965.

[59] Bo Wu, Haizhou Ai, Chang Huang, and Shihong Lao. Fast rotation invariant multi-view face detection based on real adaboost. In *Sixth IEEE International Conference on Automatic Face and Gesture Recognition, 2004. Proceedings.*, pages 79–84. IEEE, 2004.

[60] Frances A. Yates. *The Art of Memory*. The University of Chicago Press, 1966.

[61] Vladimir Zatsiorsky. *Kinematics of Human Motion*. Human Kinetics, 1998.